University of Crete
Department of Physics
Microelectronics Research Group

EPITAXIAL GROWTH AND CHARACTERIZATION OF III-NITRIDE THIN FILMS AND HETEROSTRUCTURES FOR PHOTOVOLTAIC APPLICATIONS

Ph.D. Dissertation

Elena Papadomanolaki

Supervising Professor:
Eleftherios Iliopoulos

Crete, 2017

TABLE OF CONTENTS

Acknowledgments

I would like to thank my supervising professor, Eleftherios Iliopoulos for his guidance. I would also like to give thanks to anyone who worked with me to make this possible: Stelios Kazazis, the other member of our group and valuable partner for his collaboration and support; Prof. George Dimitrakopoulos, and Dr. Calliope Bazioti from the Aristotle University of Thessaloniki, for their contribution with TEM characterization; members of the Microelectronics Research Group, Katerina Tsagaraki, for her indispensable advice with XRD and for psychological support, Maria Androulidaki for working with us on PL characterization, Dr. Adam Adikimenakis for all his help with MBE. I would like to thank Nikos Papadakis and Michalis Sfendourakis for the all important technical support.

Most importantly, I would like to thank my friend and colleague, Savvas Eftychis, for many years of sharing all kinds of problems, academic, emotional, philosophical. I thank my friends, who love me and think of me even when we are far apart, for taking care of me when I need it. I owe my gratitude to my parents to whom I hope not to be too much of a problem: my father, who showed me responsibility, and my mother, who showed me compassion. I would like to thank my dear sister, for her support, and for being an awesome person, and my dog, Roza, for reminding me not to be too hard on myself. Lastly, for getting me through this, I would like to give my thanks to cpt. Rogers, and Picard.

This research has been co-financed by the European Union (European Social Fund – ESF) and Greek national funds through the Operational Program "Education and Lifelong Learning" of the National Strategic Reference Framework (NSRF) - Research Funding Program: THALES.

Με τη συγχρηματοδότηση της Ελλάδας και της Ευρωπαϊκής Ένωσης

Abstract

Indium Gallium Nitride (InGaN) alloys are a family of semiconductors with a direct band gap that can span the entire solar spectrum. This property gives them great promise for optoelectronic applications, especially solar cells. Combining the band gap tunability of the system with multi-juction solar cell architectures has the potential for devices with high efficiencies, that push past the Schockly-Queisser limit. For device development, however, several challenges have to be overcome: increased structural defects due to the large lattice mismatch between the alloy endpoints as well as phase separation phenomena caused by the immiscibility of the alloy components, especially at high temperatures. Plasma-assisted Molecular Beam Epitaxy has proven a very valuable tool when it comes to addressing these problems, mainly because of the far-from-equilibrium nature of the epitaxy. However, challenges in epitaxy remain due to the very different temperatures typically employed for MBE growth of GaN and InN Additionally, the kinetic mechanisms that take part in InGaN growth, such as InGaN decomposition, and Indium desorption, are yet to be fully understood. In the present work, the MBE growth of InGaN is thoroughly studied, with the goal to shed light to the kinetic processes that govern it, to eliminate inhomogeneities and phase separation, to achieve better control over the alloy composition, and to optimize the conditions for films of desirable structural and optoelectronic properties.

The role of substrate temperature on InGaN growth is investigated. For that reason, a large number of InGaN films were grown on (0001)GaN substrates by MBE under a range of different growth conditions. Films were characterized by HR-XRD, HR-TEM, SEM, AFM, PL, and Hall effect measurements. Temperature effects on the kinetic processes, growth conditions, and indium incorporation mechanisms are discussed. For low growth temperatures, InGaN decomposition seems to be the dominant mechanism dictating the growth conditions. For higher temperatures, when In desorption becomes more prominent, both processes are found to affect the growth conditions. The temperature's influence on structural and optoelectronic properties of InGaN alloys is examined. Temperature is found to play an important part in the occurrence of phase separation, as well as on the different strain relaxation mechanisms of the InGaN epilayer (sequestration, introduction of threading dislocations and stacking faults and V-pits formation). Low temperatures seem to favor the growth of uniform, homogenous films with no phase separation. A correlation is found between alloy inhomogeneities and different structural defects with the films' optoelectronic properties.

Next, the process of InGaN thermal decomposition is examined. Decomposition is known to significantly affect the growth conditions by decreasing the effective rate of active nitrogen during MBE growth. The dependence of InGaN decomposition rate on the growth temperature, however is not well-understood. A thorough study is performed to accurately determine the InGaN decomposition rate. To that purpose, a large number of samples were grown with different element

arrival rates and growth temperatures by MBE, and were characterized with XR-XRD, spectroscopic ellipsometry, SEM, and AFM. Decomposition during growth is found to be influenced by surface phenomena and to be a function of growth temperature, and adatom arrival rate, rather than alloy composition. A quantitative model for the decomposition rate is extracted. Furthermore, the films' morphological characteristics are found to be greatly influenced by the extent of InGaN decomposition; very high decomposition rates are found to be detrimental to the alloys' structural properties. A window for the optimum growth conditions for InGaN alloys of different composition is determined.

Indium adsorption and desorption processes are also studied in this work. Desorption is the main mechanism that limits metal rates, and, in particular, the arrival rate of indium, during InGaN growth. Furthermore, the presence of a metal adlayer on the growth surface has a significant affect on the growth mode. To investigate indium adsorption and desorption during InGaN MBE growth, GaN(0001) substrates were exposed to different indium fluxes, while the evolution of the RHEED specular intensity was monitored. Experiments were performed for a wide range of substrate temperatures. It was revealed that indium adsorbes into the GaN surface in a bilayer structure. Any excess indium impinging on the surface forms droplets on top of this bilayer. Desorption rates were measured, and activation energies were extrated for both individual layers. It was also found that the desorption rate's dependence on the indium coverage is not according to the Langmuir isotherm.

Finally, the previous results are combined to determine the precise effect of the kinetic processes on InGaN growth conditions. It is found that indium incorporation is defined by the presence of the indium bilayer, and its level of indium coverage. A quantitative was to correlate the coverage with kinetic processes is suggested.

The last part of this dissertation includes presentation on some initial work on InGaN heterostructures and photovoltaic devices. This is the starting point for the next step of the ongoing effort toward device application. The structures included in this part are InGaN/GaN multiple quantum well (MQW) structures, InGaN/*p*-Si(111) heterostructures, as well as two preliminary photovoltaic devices.

LIST OF FIGURES

LIST OF TABLES

Introduction

Significance of III-nitrides

Over the last few decades III-nitrides have proven themselves a family of highly promising materials for optoelectronic and electronic applications. They are widely used in such devices as light emitting diodes (LEDs), high electron mobility transistors (HEMTs), ultra-violet detectors, solar cells, and the list goes on. Nitride ternary alloys (InGaN, AlGaN, InAlN), constitute a system of semiconductors with direct band gaps spanning from 0.65eV for InN[1] to 3.4eV for GaN, and up to 6.2 for AlN[2]. (fig. 1). Additionally, III-nitrides possess such appealing properties as high carrier mobilities, low effective carrier masses, high breakdown fields, high thermal conductivity. Their chemical inertness and excellent mechanical properties render them suitable for applications in harsh environments, such as industrial locations and the outer space; their ability to operate at high frequencies make the suitable for communication applications.

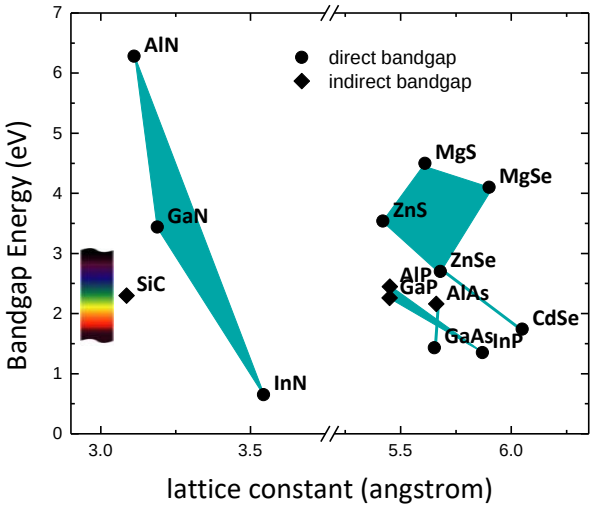

Figure i: Bandgaps of some of the most important elemental and binary cubic semiconductors versus their lattice constant at room temperature.

Single crystal gallium nitride was first synthesized by hybrid vapour phase epitaxy in 1969[3] and it wasn't long before the first GaN-based light emitting diode was fabricated by Pankove and Miller in 1971[4] using Zn doping. However, in these early days, poor material quality, with high densities of dislocations and impurities, made GaN unsatisfactory for efficient device fabrication. It wasn't until the 1980s, with the development and improvement of such methods of crystal synthesis as metal organic chemical vapor deposition (MOCVD) and molecular beam epitaxy (MBE) that the crystal quality was finally improved. In 1986, Amano[5] suggested the introduction of a low temperature AlN nucleation layer pior to GaN growth. This breakthrough led to dramatic

improvements both for the crystal quality and the electronic and optical properties of GaN. Even with greatly improved quality, however, p-type doping in GaN still presented an obstade that needed to be overcome on the way to efficient device development. In 1989[6] Amano succeeded in achieving p-type conductivity while maintaining high crystal quality utilizing magnesium as an acceptor. Soon after, the first GaN p-n blue LED junction was realized. These breakthroughs renewed interest in nitride research which hasn't diminished since. The performance of LED devices was further improved when, in 1995[7], Nakamura reported on the use of a InGaN/GaN quatum well as an active layer. Similar structures are used in commercial LEDs and LDs up to this day.

In 2014, the Nobel Prize in Physics was awarded to Isamu Akasaki, Hiroshi Amano, and Shuji Nakamura 'for the invention of efficient blue light emitting diodes which has enabled bright and energy saving white light sources[8].

InGaN for photovoltaic applications

With regards to photovoltaic applications, indium gallium nitride ($In_xGa_{1-x}N$) in particular is an ideal material candidate with its band gap tunable across the entirety of the solar spectrum depending on the relative indium content, x (fig. iia). The great advantage of InGaN over other systems of materials becomes apparent when we consider the case of multi-junction or tandem solar cells[9]. Even though Si-based photovoltaics have become competitive in some markets over the past years, the efficiency of first and second generation solar cells is limited by the Shockley-Queisser limit[10] (fig iib). There are two main energy loss mechanisms in the energy conversion

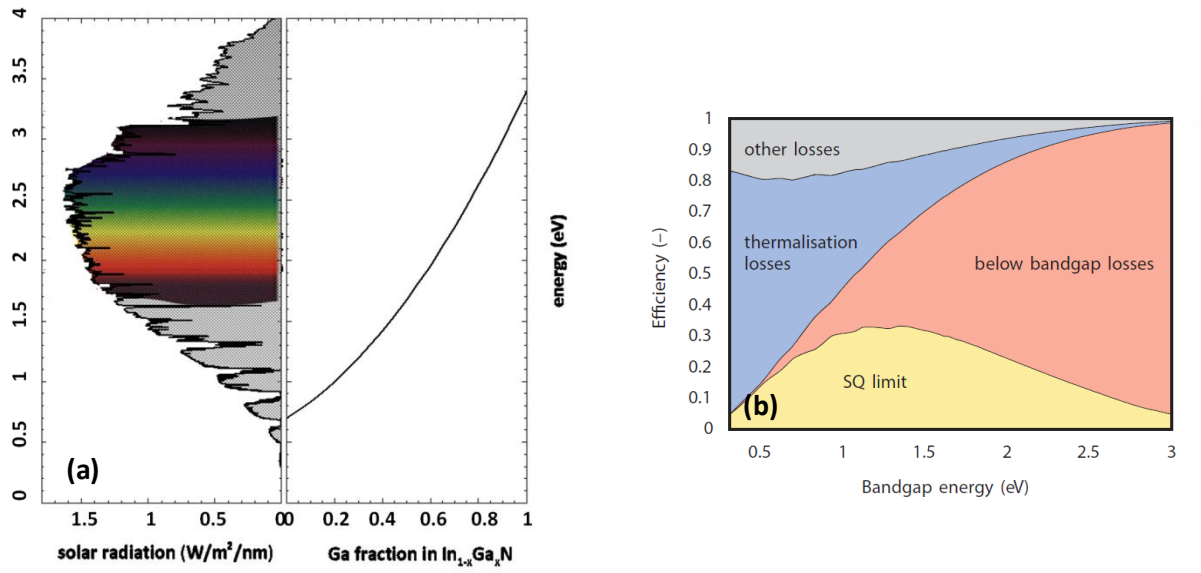

Fig ii: (a) Bandgap energies of the InGaN alloy system cover the entire air-mass-1.5 solar spectrum. [11] (b) The Shockley-Quessier limit and causes of energy loss. With yellow, energy that can be extracted as useful electrical power (the Shockley-Queisser efficiency limit); with red, energy of below-bandgap photons; with blue, energy lost when hot photogenerated electrons and holes relax to the band edges; with grey, energy lost in the tradeoff between low radiative recombination versus high operating voltage.

process of a single-junction solar cell. Only photons with energy higher than the band gap energy of the absorber can generate electron-hole pairs. Since the electrons and holes tend to occupy energy

levels at the bottom of the conduction band and the top of the valence band, respectively, the extra energy is released as heat into the semiconductor lattice in the thermalisation process. Photons with energy lower than the band gap energy of the active layer cannot be absorbed at all and are, therefore, not involved in the energy conversion process. The most promising approach to push over the SQ limit is the use of multi-junction cells to absorb a wider energy range of incident photons. In this architecture, the solar spectrum is divided into different ranges, typically three of them, and each of these fractions of the spectrum is absorbed and converted by a junction that uses a material with a carefully matching band-gap. The different cells are stacked on top of each other with the largest band-gap closer to the sun. For an infinite number of stacks, the theoretical upper limit of tandem solar cells reaches 86.6%[12], as opposed to the 33% for a single-junction cell. Using this approach, record efficiencies have been achieved, such as 40.7% on a triple-junction metamorphic GaInP/GaInAs/Ge cell (figure iii) under high concentration[13], and reaching as high as 46% under concentrated sunlight for a four-junction GaInP/GaAs/GaInAsP/GaInAs solar cell[14]

For a long time it was believed that the band-gap of InN was 1.9 eV, but ever since several studies revealed it to be 0.65eV[1], it became obvious that Indium gallium nitride ($In_xGa_{1-x}N$) is an ideal material candidate for such applications as its range of band gaps covers the solar spectrum depending on the relative indium content, x. Tandem devices can greatly benefit from employing a single alloy system to cover the solar spectrum in simplifying the manufacturing process, thus reducing the overall cost. Moreover, this would allow for more versatility in engineering, opening up new possibilities for improving device efficiency, without further increasing their complexity.

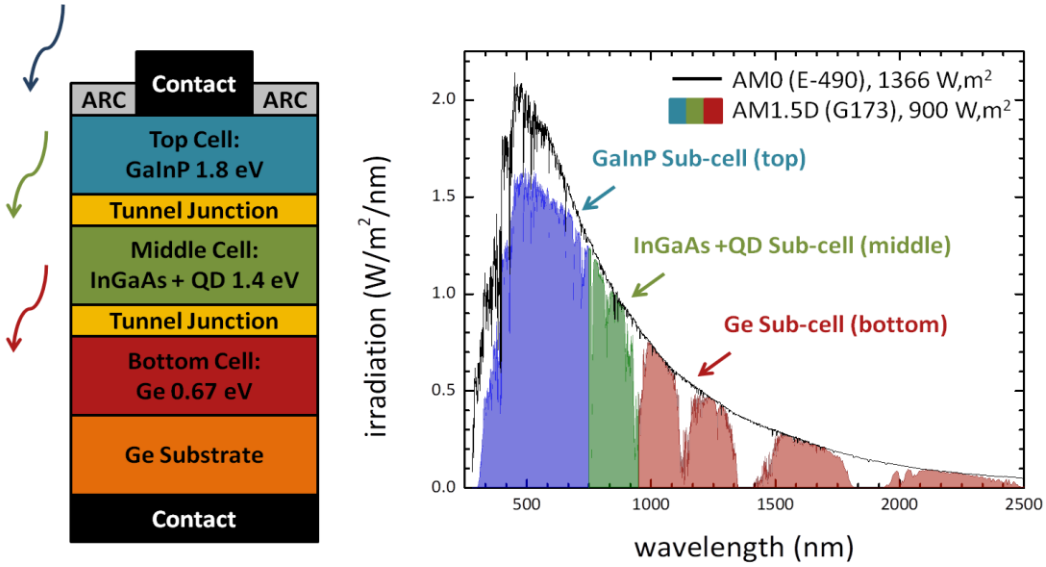

Fig iii: The structure of an MJ solar cell with a graph of solar radiation together with the maximum electricity conversion efficiency for every junction.

What is more, as a member of the III-nitride alloy semiconductor group, InGaN possesses many optoelectronic properties that give it additional advantages. It is a direct band-gap semiconductor, with a very high absorption coefficient on the order of 105 cm^{-1} near the band edge,[15] a low effective mass of charge carriers (electrons and holes), high peak and saturation velocities. Like all nitride semiconductors, they possess spontaneous and piezoelectric properties that can, with the proper engineering, be exploited to assist in the operation of the solar cell by enhancing the fields in the active layer. High radiation tolerances have been observed indicating InGaN-based devices will have long-term reliability in harsh environments[11]. Moreover, unlike similar devices, InGaN solar cells eliminate the use of toxic elements like arsenic, cadmium, or phosphorous.

Since 2002, and the reevaluation of InN bandgap energy, there have been various efforts to fabricate InGaN solar cells based on different approaches, with some success [9, 16]. However, on the way to efficient InGaN photovoltaics, there are limitations, most of which have to do with the quality of the material[17, 18]. We will discuss such difficulties presently.

Challenges of the InGaN alloy system

In spite of the advantages of $In_xGa_{1-x}N$ that promise the great potential it has for photovoltaic and other applications, there are several challenges that hinder the progress to that goal. These challenges mostly focus on the growth and development of adequate quality material that spans the entire compositional range from x=0 to 1.

Lattice mismatch and crystal quality.

Due to the lack of native substrates, InGaN and other nitride alloys are challenging to grow in large thicknesses. There's a 16% lattice mismatch between GaN and sapphire and 29% between sapphire and InN[19]. Furthermore, the lattice mismatch between InN and GaN is about 10%. As a result, even for growth of InGaN on a GaN substrate, the critical thickness of the heteroepitaxy has been found to be very low. Theoretical studies have shown the critical thickness to be less than 10nm for InGaN with a composition of 20% InN or lower[20-22], and to further decrease for higher Indium contents. Above the critical thickness, defects are introduced into the film; these include threading dislocations, stacking faults, cracks, pits, and more. InGaN films therefore suffer from high threading dislocation densities[22, 23], and this can deteriorate device performance, especially when solar cells are considered.

Growth conditions and In incorporation

In addition to the lattice mismatch, another factor that contributes to the increased difficulty of successfully developing InGaN films of adequate quality, is the great difference between optimum growth conditions for the alloy endpoints, InN, and GaN. GaN is typically grown at temperatures as high as 900^{o}C for MOCVE and >700^{o}C for MBE[2]. Bonds between indium and nitrogen are much weaker than bonds between gallium and nitrogen, and, at such temperatures this causes InN to decompose at very high rates[24].

This causes a reduced In incorporation in the film, and makes it very difficult to grow In-rich InGaN, especially in the case of MOCVD[25]. In addition, the difference in formation enthalpies for InN and GaN causes phenomena of strong indium segregation on the growth front[26-29], which also limits the incorporation of indium. Such problems can be addressed by optimizing growth parameters. It has been shown that lowering the growth temperature can improve In incorporation[30], but it does so at the cost of material quality, as less energy is supplied to reactant atoms to find an optimal location in the crystalline lattice. Higher growth rates have also been reported to improve In incorporation[31, 32].

Phase separation and inhomogeneities

One of the main challenges with InGaN alloys is that they tend to suffer from compositional inhomogeneities and phase separation phenomena. One of the reasons for this is the indium segregation along the growth front that was mentioned before. Even though, it has been shown that indium can be useful as a surfactant for growth of GaN or AlN[33, 34], in the case of InGaN, the alloy is very sensitive to accumulated In on the growth surface, and it is very difficult to control without risking fluctuations of the composition of the film. Nitrogen-rich conditions can be used to eliminate this effect, but they also compromise material quality. On top of this, it has been shown[35] that, for

compositions of InGaN close to the 50% mark, there is a miscibility gap between the alloy constituents. This can cause both minor indium compositional fluctuations, as well as two completely separate phases[36]. Although some small amount of phase separation can in actuality be advantageous for some applications such as LEDs[36, 37], in the case of solar cells it can prove highly detrimental, since they lead to increased electron-hole recombination rates and limit the device efficiency[38].

Doping

InGaN is intrinsically a n-type semiconductor due to its high density donor-type of defects and strong electron surface accumulation[17]. For higher indium compositions especially, the intrinsic carrier concentration becomes particularly high. As a result, the p-type doping of InGaN alloys has proven very difficult. P-type doped InN has been demonstrated[39], but for InGaN, the results have been very limited[40, 41], with focus on low-content indium films[17].

Motivation and overview

At present, MOCVD is the most popular technique for growing most III-Nitride materials and devices. However, with regards to InGaN growth, radio-frequency Molecular Beam epitaxy (RF-MBE) demonstrates a number of advantages over MOCVD. Namely, growth by MBE is carried out under conditions that are far from thermodynamic equilibrium. Under such conditions, epitaxy is governed mainly by the kinetics on the growth surface. This non-equilibrium character of the growth, along with lower growth temperatures used in MBE, can be exploited to avoid one of the most prominent problems of InGaN alloys as was mentioned above: phase separation. Indium incorporation has also been found to benefit from MBE conditions, producing indium-richer alloys. It has been shown[42] that homogenous InGaN films across the compositional range can be grown by MBE. Additionally, since MBE growth is operated in high vacuum, it provides high in-situ monitoring capability, and precise control of the growth parameters. This makes it an ideal tool for studying and developing InGaN alloys with adequate crystal quality, and satisfactory properties.

The focus of the present thesis is to make use of the advantages presented by MBE for the growth and investigation of InGaN films and heterostructures with an outlook to photovoltaic applications. In particular, some of the points we will be turning our attention to include:

- In depth study of the kinetic mechanisms that govern non-equilibrium MBE growth and how they affect indium incorporation, to achieve indium-rich InGaN alloys
- Investigation of structural properties of InGaN films and correlation with growth conditions. Phase separation phenomena and relaxation of films are considered with aim to realize quality homogenous material.
- Correlation of structural quality and growth conditions with the films' optoelectronic properties
- Optimizing MBE growth conditions according to desired composition and properties
- A first look at InGaN heterostructures for photovoltaic applications

REFERENCES

1. Wu, J., et al., *Unusual properties of the fundamental band gap of InN.* Applied Physics Letters, 2002. **80**(21): p. 3967-3969.
2. Ambacher, O., *Growth and applications of Group III-nitrides.* Journal of Physics D: Applied Physics, 1998. **31**(20): p. 2653.
3. Maruska, H.P. and J.J. Tietjen, *THE PREPARATION AND PROPERTIES OF VAPOR-DEPOSITED SINGLE-CRYSTAL-LINE GaN.* Applied Physics Letters, 1969. **15**(10): p. 327-329.
4. Pankove, J.I., E.A. Miller, and J.E. Berkeyheiser, *GaN blue light-emitting diodes.* Journal of Luminescence, 1972. **5**(1): p. 84-86.
5. Amano, H., et al., *Metalorganic vapor phase epitaxial growth of a high quality GaN film using an AlN buffer layer.* Applied Physics Letters, 1986. **48**(5): p. 353-355.
6. Hiroshi, A., et al., *P-Type Conduction in Mg-Doped GaN Treated with Low-Energy Electron Beam Irradiation (LEEBI).* Japanese Journal of Applied Physics, 1989. **28**(12A): p. L2112.
7. Shuji, N., et al., *Superbright Green InGaN Single-Quantum-Well-Structure Light-Emitting Diodes.* Japanese Journal of Applied Physics, 1995. **34**(10B): p. L1332.
8. *The Nobel Prize in Physics 2014*. 2014 Web. 9 May 2017]; Available from: http://www.nobelprize.org/nobel_prizes/physics/laureates/2014/.
9. Neufeld, C.J., et al., *High quantum efficiency InGaN/GaN solar cells with 2.95 eV band gap.* Applied Physics Letters, 2008. **93**(14): p. 143502.
10. Shockley, W. and H.J. Queisser, *Detailed Balance Limit of Efficiency of p-n Junction Solar Cells.* Journal of Applied Physics, 1961. **32**(3): p. 510-519.
11. Wu, J., et al., *Superior radiation resistance of In1−xGaxN alloys: Full-solar-spectrum photovoltaic material system.* Journal of Applied Physics, 2003. **94**(10): p. 6477-6482.
12. Vos, A.D., *Detailed balance limit of the efficiency of tandem solar cells.* Journal of Physics D: Applied Physics, 1980. **13**(5): p. 839.
13. King, R.R., et al., *40% efficient metamorphic GaInP/GaInAs/Ge multijunction solar cells.* Applied Physics Letters, 2007. **90**(18): p. 183516.
14. Dimroth, F., et al., *Four-Junction Wafer-Bonded Concentrator Solar Cells.* IEEE Journal of Photovoltaics, 2016. **6**(1): p. 343-349.
15. Davydov, V.Y., et al., *Band Gap of Hexagonal InN and InGaN Alloys.* physica status solidi (b), 2002. **234**(3): p. 787-795.
16. Liou, B.W., *Design and fabrication of InxGa1−xN/GaN solar cells with a multiple-quantum-well structure on SiCN/Si(111) substrates.* Thin Solid Films, 2011. **520**(3): p. 1084-1090.
17. Chen, X., et al., *Growth, fabrication, and characterization of InGaN solar cells.* physica status solidi (a), 2008. **205**(5): p. 1103-1105.
18. Jani, O., et al., *Design and characterization of GaN/InGaN solar cells.* Applied Physics Letters, 2007. **91**(13): p. 132117.
19. Wang, X. and A. Yoshikawa, *Molecular beam epitaxy growth of GaN, AlN and InN.* Progress in Crystal Growth and Characterization of Materials, 2004. **48-49**: p. 42-103.
20. Holec, D., et al., *Critical thickness calculations for InGaN/GaN.* Journal of Crystal Growth, 2007. **303**(1): p. 314-317.
21. Zhao, W., et al., *Theoretical study on critical thicknesses of InGaN grown on (0001) GaN.* Journal of Crystal Growth, 2011. **327**(1): p. 202-204.
22. Parker, C.A., et al., *Determination of the critical layer thickness in the InGaN/GaN heterostructures.* Applied Physics Letters, 1999. **75**(18): p. 2776-2778.
23. Faleev, N., et al., *Correlation of crystalline defects with photoluminescence of InGaN layers.* Applied Physics Letters, 2009. **95**(5): p. 051915.
24. Thaler, G.T., et al., *Thermal stability of thin InGaN films on GaN.* Journal of Crystal Growth, 2010. **312**(11): p. 1817-1822.

25. Yam, F.K. and Z. Hassan, *InGaN: An overview of the growth kinetics, physical properties and emission mechanisms.* Superlattices and Microstructures, 2008. **43**(1): p. 1-23.
26. Adelmann, C., et al., *Indium incorporation during the growth of InGaN by molecular-beam epitaxy studied by reflection high-energy electron diffraction intensity oscillations.* Applied Physics Letters, 1999. **75**(22): p. 3518-3520.
27. Karpov, S.Y. and Y.N. Makarov, *A Quantitative Model of Surface Segregation in III-V Ternary Compounds.* MRS Proceedings, 2011. **618**.
28. Yoshimoto, N., et al., *Photoluminescence of InGaN films grown at high temperature by metalorganic vapor phase epitaxy.* Applied Physics Letters, 1991. **59**(18): p. 2251-2253.
29. Duff, A.I., L. Lymperakis, and J. Neugebauer, *Understanding and controlling indium incorporation and surface segregation on InxGa1−xN surfaces: Anab initioapproach.* Physical Review B, 2014. **89**(8).
30. Averbeck, R. and H. Riechert, *Quantitative Model for the MBE-Growth of Ternary Nitrides.* physica status solidi (a), 1999. **176**(1): p. 301-305.
31. Wu, Z.H., et al., *Spontaneous formation of highly regular superlattice structure in InGaN epilayers grown by molecular beam epitaxy.* Applied Physics Letters, 2011. **98**(14): p. 141905.
32. Moseley, M., et al., *Control of surface adatom kinetics for the growth of high-indium content InGaN throughout the miscibility gap.* Applied Physics Letters, 2010. **97**(19): p. 191902.
33. Neugebauer, J., et al., *Adatom kinetics on and below the surface: the existence of a new diffusion channel.* Phys Rev Lett, 2003. **90**(5): p. 056101.
34. Yamaguchi, T., et al., *Novel InN growth method under In-rich condition on GaN/Al2O3 (0001) templates.* physica status solidi (c), 2009. **6**(S2): p. S360-S363.
35. Ho, I.h. and G.B. Stringfellow, *Solid phase immiscibility in GaInN.* Applied Physics Letters, 1996. **69**(18): p. 2701-2703.
36. Stringfellow, G.B., *Microstructures produced during the epitaxial growth of InGaN alloys.* Journal of Crystal Growth, 2010. **312**(6): p. 735-749.
37. Grandjean, N. and M. Ilegems, *Visible InGaN/GaN Quantum-Dot Materials and Devices.* Proceedings of the IEEE, 2007. **95**(9): p. 1853-1865.
38. Lai, K.Y., et al., *Effect of indium fluctuation on the photovoltaic characteristics of InGaN/GaN multiple quantum well solar cells.* Applied Physics Letters, 2010. **96**(8): p. 081103.
39. Jones, R.E., et al., *Evidence for p-type doping of InN.* Phys Rev Lett, 2006. **96**(12): p. 125505.
40. Horie, M., et al., *MOVPE growth and Mg doping of InxGa1−xN (x ~0.4) for solar cell.* Solar Energy Materials and Solar Cells, 2009. **93**(6-7): p. 1013-1015.
41. Chang, C.-A., et al., *Magnesium Doping of In-rich InGaN.* Japanese Journal of Applied Physics, 2007. **46**(5A): p. 2840-2843.
42. Iliopoulos, E., et al., *InGaN(0001) alloys grown in the entire composition range by plasma assisted molecular beam epitaxy.* physica status solidi (a), 2006. **203**(1): p. 102-105.

CHAPTER 1: An overview of III-Nitrides

1.1 General Properties of III-Nitrides

Nitride semiconductors are defined as III-V compound semiconductors in which nitrogen is the group V element. Group III-Nitrides include GaN, AlN, InN and their alloys. Their significance for research and application, as well as some of their most prominent advantages were extensively discussed in the introduction. In this chapter, we will briefly review some of their most important properties. Gallium Nitride (GaN), as the most studied and well-understood member of the group, will often be used as an example in the following discussion.

1.1.1 Crystal Structure

The thermondynamically stable phase of nitrides is the hexagonal wurtzite structure. It consists of alternating biatomic closed-packed planes of group III atoms and nitrogen pairs stacked in an ABABAB sequence (figure 1.1a), with the first and third layer perfectly aligned. Apart from that, it is also possible to stabilie a zincblende structure for nitride films. In this case, the closed packed plans of the crystal follow an ABCABC sequence figure 1.1b.

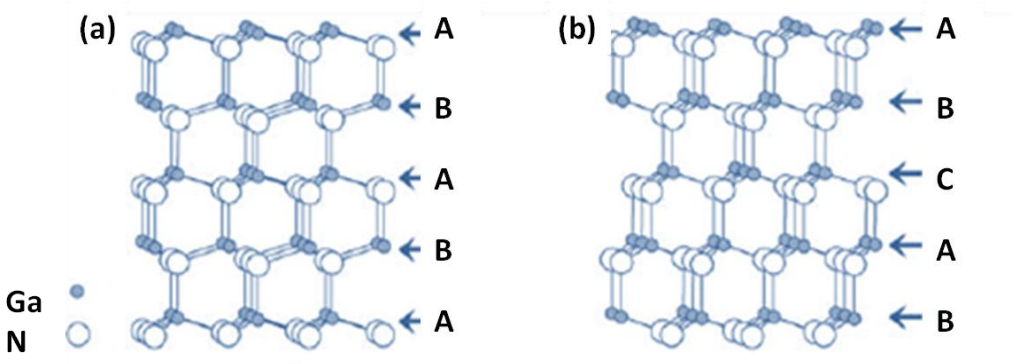

Figure 1.1: (a)Wurtzite, and (b) Zincblende structrure of GaN.

The hexagonal crystal structure is presented in figure 1.2. It can be described by the lattice parameters a_0, which is the length of the basal hexagon, c_0, which corresponds to the height of the hexagonal prism, and u, which is used to characterize the III-N bond length along the (0001) axis. Table I summarizes the values of a_0, c_0, and u, for GaN, AlN, and InN. Each lattice atom is tetrahedrally bonded to the nearest neighbor, and each group of atoms, metal or nitrogen, forms a

separate hexagonal system; the two systems are shifted by a ratio *u* of the c_0 lattice parameter in relation to each other along the (0001) axis.[1]

	GaN	AlN	InN
c_0	5.185[a]	4.982[b]	5.79374[a]
a_0	3.1884[a]	3.112[b]	3.53774[a]
u	0.376[b]	0.38[b]	0.377[b]

Table I: Values for the c0, and a0 lattice parameters, as well as for the bond length for GaN, AlN, and InN. Values noted with [a] are from reference [2], and values noted [b] from reference [3].

The Miller-Bravais notation {hkil} is used to index the atmic planes of the crystal. In figure 1.2b planes of interest for III-nitrides are noted. These include basal *c*-planes, which are the ones perpendicular to the c-axis, *a*-planes and *m*-planes (indexed {1120} and {1010} respectively in Miller notation), which are parallel to the c-axis, and r-planes.

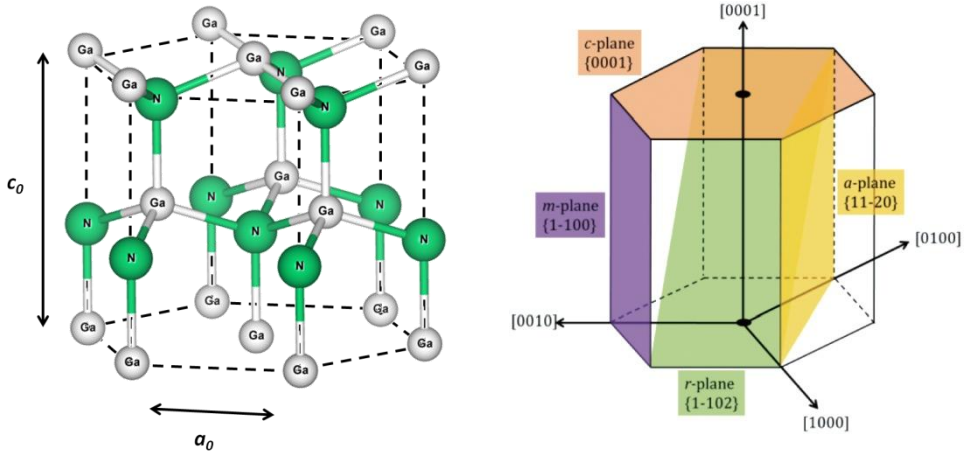

Figure 1.2: (a) Hexagonal wurtzite crystal structure of GaN; the lattice parameters c0, and a0 are defined. (b) Planes of interest for the hexagonal crystal structure, and the respective Miller indices are shown.

Polarity

All group III-nitrides lack an inversion plane perpendicular to the *c*-axis. This property is referred to as the *polarity* of the nitride layer, and is defined by the direction of the metal-nitrogen bond parallel to the (0001) direction, which is the most common for crystal growth. Thus, if we assume GaN as an example, a plane perpendicular to the *c*-axis can be either Ga-faced (also called Ga-polar, or +c), meaning there's a Ga atom on the top position in the Ga-N bond, or N-faced (or N-polar, or –c), meaning the nitrogen atom is on top (figure 1.3).

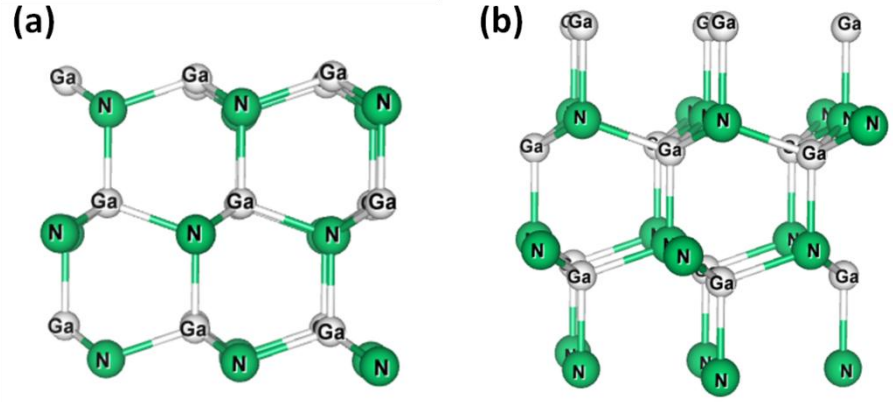

Figure 1.3: Illustration of GaN wurtzite crystal structure exhibiting the polarity along the c-axis. GaN with (a) shows Ga-face (+c) polarity, and (b) N-face (-c) polarity[4].

{0001} c-planes are naturally the ones most affected y the asymmetry of the III-N bond and, for that reason, they are usually referred to as *polar*. Planes parallel to the *c*-axis are non-polar. These include *a*- and *m*-planes. All other planes, with angles to the *c*-axis that are different than 0^{o} or 90^{o} are referred to as *semi-polar*.

The polarity of a crystal film is found to affect both the crystal growth and the material properties. For example, Ga-polar GaN usually shows smoother surfaces and better crystal quality. Polarity affects the growth rate, as well as impurity incorporation and doping efficiency; Mg doping is found to be much more effective for Ga-polar GaN. Chemical and optical properties are also affected by polarity[4-6]. Lastly, polarity plays an important role in the electrical properties of nitride materials and devices, since it is closely related with *polarization* effects, which will be discussed more extensively in the following section.

1.1.2 Polarization

A significant feature of nitrides that sets them apart from other semiconductor materials is the strong *polarization* phenomena. Polarization in nitrides plays an important role in affecting electric fields, carrier distributions, and, as a consequence, the material's optical and electrical properties. Polarization fields in group III-nitrides consists of two components, spontaneous, and piezoelectric polarization.

Spontaneous Polarization

Due to the lack of center of inversion symmetry in the wurtzite structure, and the ionicity of the metal-nitrogen bond, a strong macroscopic polarization manifests along the (0001) direction in nitride semiconductors. This is known as *spontaneous* polarization and is inherent in nitride materials. The direction of the spontaneous polarization depends on the polarity of the crystal.

Piezoelecric Polarization

Piezoelectric polarization manifests when the crystal is subjected to external stress. This causes the crystal lattice to distort, and this naturally affects the polarization field. There are two factors

that can contribute to piezoelectric phenomena: the first is strain induced on the crystal by *lattice mismatch*. In heteroepitaxy, a crystal grown on a substrate with different lattice constants will be distorted due to *elastic strain*. Additionally, a difference in thermal expansion coefficients between the epilayer and the substrate can cause thermal strain and affect the piezoelectric polarization of the material. The direction of the piezoelectric field depends on the polarity, as well as on whether the material is under tensile or compressive stress. [7, 8]

1.1.3 Optical properties

Band structure of InN

InN, like all nitrides, is a direct bandgap semiconductor. Early InN samples had poor crystal quality: in most cases, polycrystalline InN was synthesized by radio-frequency sputtering, and exhibited high free electron concentration densities due to unintentional doping. Such samples showed an absorption edge at about 1.9eV, and for a long time, this was believed to be the band gap value for InN[9]. More recently, however, on account of progress with Molecular Beam Epitaxy (MBE), the quality of InN films has improved dramatically, and the band gap of InN has since been established to a value of 0.64eV[10].

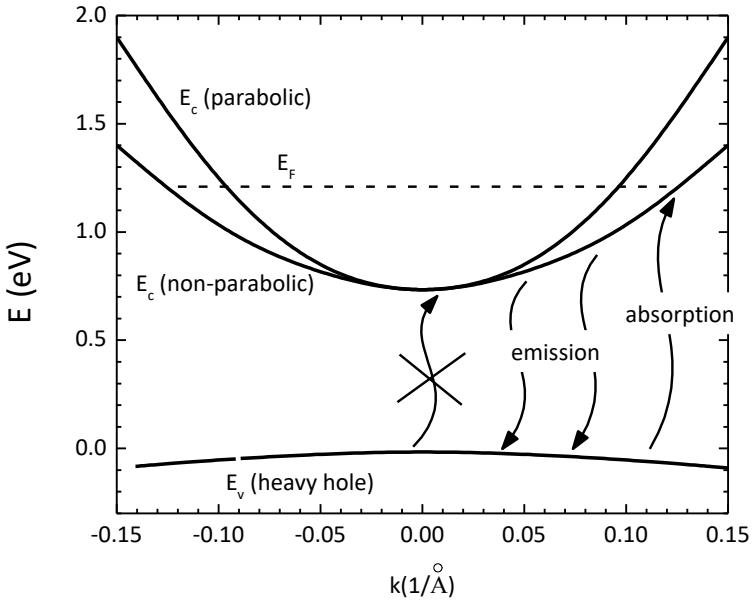

Figure 1.4: Calculated conduction and valence band dispersion of InN using the ***k·p*** model. The Fermi level is for electron concentration 10^{20} cm^{-3}.

Figure 1.4 shows the conduction and valence band dispersion calculated with the **k·p** model, using a parabolic, and non-parabolic approximation[11]. For crystals with degenerate doping, optical absorption is forbidden for transitions below the Fermi level, leading to an overestimation of the intrinsic bang gap (Burnstein-Moss effect[12]). This explains the discrepancy between the 1.9eV value for InN band gap, and the recently established 0.64eV: earlier samples were heavily doped; but

for high quality InN grown by MBE, the electron concentrations can be precisely controlled by several order of magnitude, and it has been shown that the absorption edge varies continuously from 0.64eV (intrinsic value) to ~2eV for electron concentrations of ~10^{21} cm^{-3}.

Band gap of III-Nitride ternary alloys

Apart from InN, which, as we have seen, possesses a narrow band gap of 0.64eV, the values for the direct band gaps for GaN, and AlN are about 3.4eV and 6.2eV respectively[5]. For alloys, it is well-known that the band gap value can be approximated according to the following:

$$E_g^{A_xB_{1-x}N} = xE_g^{AN} + (1-x)E_g^{BN} - bx(1-x) \quad (1.1)$$

where $E_g^{A_xB_{1-x}N}$ the band gap value for the ternary alloy $A_xB_{1-x}N$, E_g^{AN}, and E_g^{BN} the band gap values for the alloy components AN, and BN respectively, and *b* the bowing parameter.

Figure 1.5 presents the band gap values for GaN, AlN, InN, and their ternary alloys AlGaN, InGaN, and InAlN as a function of the in-plane lattice constant *a*, with the respective bowing for each alloy[13]. Particularly for InGaN, the bowing parameter has been reported to range from values as low as 1.4eV[14] to 2.5eV[15]. More recently, it has been suggested that for InGaN[16], as well as InAlN the bowing parameter itself is not independent of the alloy composition[17].

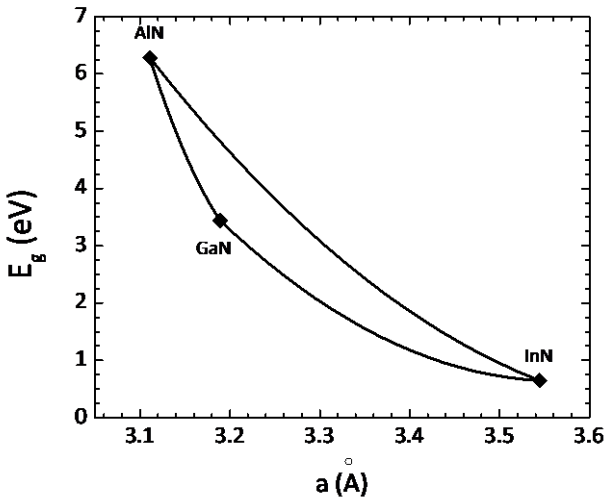

Figure 1.5: Bandgaps of group III-nitride alloys as a function of in-plane lattice constant. Each curve between two end-points is by Eq. (1.1)

1.2 Nitride Epitaxy

The term *epitaxy* is used to describe the process of synthesizing a thin film of material, often referred to as the *epilayer*, on top of a crystalline substrate. When the thin film has the same chemical composition as the substrate, the process is described as *homoepitaxy*. The deposition of a film on a substrate of different material is called *heteroepitaxy*. In order to minimize strain, and therefore, to ensure a high quality crystal for the deposited film, a suitable substrate that matches its crystal structure as closely as possible should be chosen.

There are two main methods for growing thin films of nitride semiconductors. For the first, Chemical Vapor Deposition (CVD), epitaxial films are grown from gases containing the required

chemical elements that react close to the substrate surface. The product of this reaction is deposited on the substrate as a thin film. In the case of III-V compound semiconductors, the use of metal-organic compounds like trimethyl gallium [$Ga(CH_3)_3$] is often employed. In this case, the process is described as Metal-Organic Chemical Vapor Deposition (MOCVD).

In contrast to MOCVD, where the reactions take place under relatively high pressures, the second method, Molecular Beam Epitaxy (MBE) employs the use of Ultra High Vacuum (UHV) conditions (pressures below 10^{-7} torr). In this case, a reactant is heated in a source until it vaporizes. Because of the UHV environment, its molecules are allowed to travel all the way to the substrate nearly without any collisions in a well-collimated beam called a *molecular beam*, or *atomic beam*. The film then grows on the substrate, which is heated to an appropriate temperature, epitaxially. As MBE is the main focus of this work, the particulars of the method will be discussed in greater detail in the following chapters. [18]

Other methods of nitride growth include HVPE (hydride vapor phase epitaxy) and ALD (atomic layer deposition.

Growth of a thin film can occur in one of three modes, schematically presented in figure 1.6:

- *Frank-Van der Merwe*, or layer-by-layer mode, in which deposition takes place in a two-dimensional manner, and which is desired for epitaxial growth
- *Volmer-Weber*, or three-dimensional mode, which results in growth of three-dimensional islands from the initial stages of deposition; in this case, 3D structures may eventually join to form a uniform film.
- *Stranksi-Krastanow[19] mode*, in which 2D growth will initially take place, resulting in a thin layer consisting of one or a few monolayers of crystal. This is often referred to as the wetting layer. After the wetting layer has formed, however, the growth continues in a 3D manner to form islands.

Depending on the mode, the growth can promote or inhibit the strain relaxation of the epilayer thus affecting the density of dislocations in the crystal and the overall material quality. Naturally, growth mode has also a big effect on surface smoothness Experimentally, the growth mode is a result of the materials of both the epilayer and the substrate, as well as the growth conditions. These include substrate temperature, and partial pressures of various sources.[1, 18]

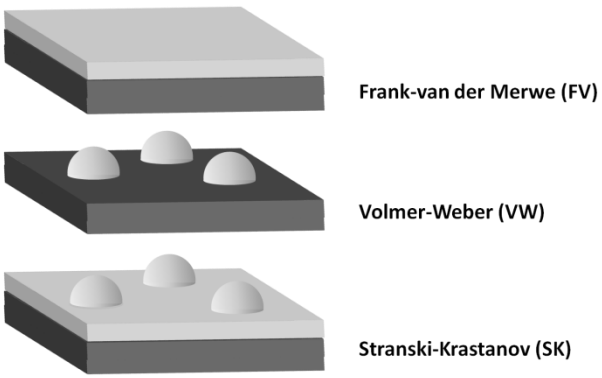

Figure 1.6: The three primary modes of thin-film growth including Frank–Van der Merwe (FM: layer-by-layer), Volmer–Weber (VW: island formation), and Stranski–Krastanov (SK: layer-plus-island).

1.2.1 Surface processes during MBE

In figure 1.7, the reader can find a schematic representation of the physical processes that take place during MBE growth. Impinging atoms adsorb on the film surface. Subsequently, the atoms may diffuse across the surface, to eventually be either incorporated in the crystal lattice by binding with lattice atoms, or desorb fromm the surface. Incorporation can happen either at sites available at steps, or as nucleation of new clusters. If the growth temperature is high enough, one must also consider the rate at which the epilayer decomposes. Atoms that result from the decomposition can then either evaporate from the surface or be re-incorporated in the lattice through the processes described above[20, 21].

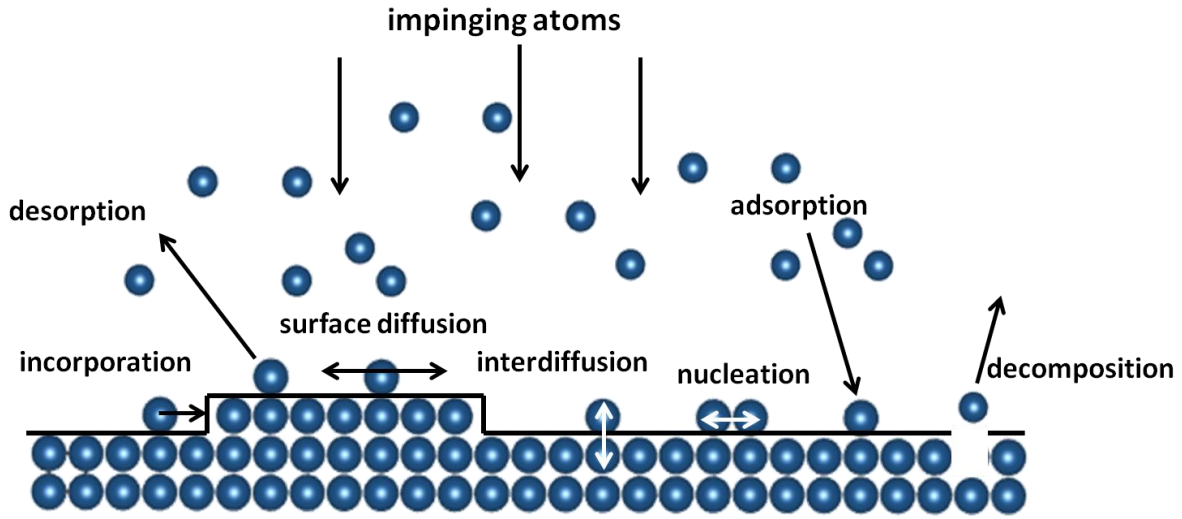

Figure 1.7: Surface processes during the MBE growth: adsorption, desorption, surface diffusion, lattice incorporation, and decomposition.

As far as nitride growth by MBE is concerned, GaN is the one most extensively studied and best understood. In the following section, a few important points regarding GaN MBE growth will be discussed.

1.2.2 GaN growth regime

When one considers the case of GaN MBE growth, the parameters that should be examined include the substrate temperature during growth, the metal and nitrogen atom fluxes, and the III/V flux ratio. Typically, we can distinguish three growth regimes:

- The N-stable, or N-rich regime. In this case the growth is limited by the amount of the available Ga atoms.
- The transition growth regime, where stoiciometric conditions are assumed, and the III/V ratio is close to unity.

- The Ga-stable regime. The growth here is limited by the available nitrogen, and the excess Ga accumulates on the growth surface. For this regime, we can additionally distinguish two separate cases. For specific conditions, here referred to as slightly Ga-rich, or meta-stable regime, Ga atoms form a bilayer on the GaN surface. Additional increase in the Ga flux will result in excess accumulation of Ga which manifests in the form of Ga droplets. This case is referred to as the droplet regime.

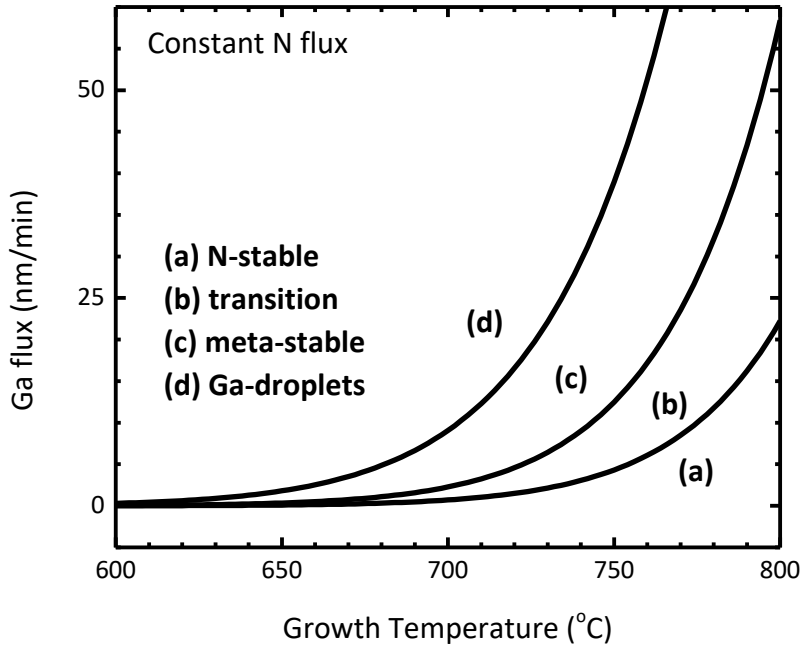

Figure 1.8: Growth diagram defining the Ga flux values for the N-stable, transition, meta-stable, and Ga-droplet regime, for a given N flux.

The diagram of figure 1.8 shows the four cases as a function of substrate temperature, as well as the III/V flux ratio. The boundary line between the Ga-droplet and intermediate regime has an Arrhenius dependence on temperature corresponding to the activation energy for Ga desorption from liquid Ga. [21]

It has been established that the presence of the Ga bilayer in the meta-stable regime encourages layer-by-layer growth by increasing the N adatom mobility on the growth surface. As a result, samples grown in this regime will exhibit smooth surfaces, as well as low dislocation densities and high optical and electrical quality. For N-rich growth conditions, the Ga diffusion length is reduced and samples grown in this regime are characterized by rough surfaces and increased defect, including threading dislocation and stacking faults[22]. On the other hand, moving too far from stoichiometry and well into the droplet region has proven to have a negative effect on the film's electrical properties, with electron mobilities drastically degrading[21]. The optimum window is therefore achieved when the Ga-bilayer coverage is maximized without the formation of Ga droplets.

REFERENCES

1. Albrecht, M., J. Neugebauer, and P. Ruterana. *Nitride semiconductors : handbook on materials and devices*. 2006; Available from: http://dx.doi.org/10.1002/3527607641.
2. Morales, F.M., et al., *Determination of the composition of InxGa1–xN from strain measurements.* Acta Materialia, 2009. **57**(19): p. 5681-5692.
3. Ambacher, O., *Growth and applications of Group III-nitrides.* Journal of Physics D: Applied Physics, 1998. **31**(20): p. 2653.
4. Sumiya, M. and S. Fuke, *Review of polarity determination and control of GaN.* MRS Internet Journal of Nitride Semiconductor Research, 2014. **9**.
5. Wang, X. and A. Yoshikawa, *Molecular beam epitaxy growth of GaN, AlN and InN.* Progress in Crystal Growth and Characterization of Materials, 2004. **48-49**: p. 42-103.
6. Hellman, E.S., *The Polarity of GaN: a Critical Review.* MRS Internet Journal of Nitride Semiconductor Research, 2014. **3**.
7. Ambacher, O., et al., *Two-dimensional electron gases induced by spontaneous and piezoelectric polarization charges in N- and Ga-face AlGaN/GaN heterostructures.* Journal of Applied Physics, 1999. **85**(6): p. 3222-3233.
8. Bernardini, F. and V. Fiorentini, *Spontaneous versus Piezoelectric Polarization in III–V Nitrides: Conceptual Aspects and Practical Consequences.* physica status solidi (b), 1999. **216**(1): p. 391-398.
9. Morkoç, H., *Nitride Semiconductors and Devices.* 1999.
10. Wu, J., et al., *Unusual properties of the fundamental band gap of InN.* Applied Physics Letters, 2002. **80**(21): p. 3967-3969.
11. Wu, J., *When group-III nitrides go infrared: New properties and perspectives.* Journal of Applied Physics, 2009. **106**(1): p. 011101.
12. Wu, J., et al., *Effects of electron concentration on the optical absorption edge of InN.* Applied Physics Letters, 2004. **84**(15): p. 2805-2807.
13. Wu, J., et al., *Universal bandgap bowing in group-III nitride alloys.* Solid State Communications, 2003. **127**(6): p. 411-414.
14. Wu, J., et al., *Small band gap bowing in In1–xGaxN alloys.* Applied Physics Letters, 2002. **80**(25): p. 4741-4743.
15. Davydov, V.Y., et al., *Band Gap of Hexagonal InN and InGaN Alloys.* physica status solidi (b), 2002. **234**(3): p. 787-795.
16. Moses, P.G. and C.G. Van de Walle, *Band bowing and band alignment in InGaN alloys.* Applied Physics Letters, 2010. **96**(2): p. 021908.
17. Iliopoulos, E., et al., *Energy bandgap bowing of InAlN alloys studied by spectroscopic ellipsometry.* Applied Physics Letters, 2008. **92**(19): p. 191907.
18. Yu, P.Y., Cardona, M. *Fundamentals of Semiconductors*. 2010; Available from: http://dx.doi.org/10.1007/978-3-642-00710-1.
19. Stranski, I.N., Krastanow. L., *Zur Theorie der orientierten Ausscheidung von Ionenkristallen aufeinander.* Monatshefte fur Chemie, 1937. **71**(1): p. 351-364.
20. Henini, M., *Molecular beam epitaxy : from research to mass production*. 2013.
21. Morkoç, H., *III-Nitride semiconductor growth by MBE: Recent issues.* Journal of Materials Sciene: Materials in Electronics, 2001. **12**(12): p. 667-695.
22. Morkoç, H. and I. Wiley. *Handbook of nitride semiconductors and devices*. 2008; Available from: http://onlinelibrary.wiley.com/book/10.1002/9783527628438.

CHAPTER 2: Experimental Methods

2.1 Molecular Beam Epitaxy

As it has been briefly mentioned in the previous chapter, molecular beam epitaxy (MBE) is an epitaxial process which is characterized by growth in an Ultra High Vacuum (UHV) environment. The constituent elements are supplied in the form of molecular, or atomic beams onto a heated crystalline substrate to form thin epitaxial layers. The term molecular beam epitaxy was first used in 1970 by Alfred Y. Cho and his colleagues at Bell Laboratories [1, 2] after years of studies of molecular beams interacting with solid surfaces[3, 4]. Today, MBE is not only a valuable research tool but also, especially in the case of arsenide compound semiconductors, a method for material development for commercial applications[5]

2.1.1 Ultra High Vacuum

The UHV environment plays an important part in the function of MBE. The system, at pressure *p* is characterized by the mean free path between collisions of particles, which, according to kinetic theory is given by the following formula:

$$\lambda = \frac{k_B T}{\sqrt{2}\pi d^2 p} \qquad (2.1)$$

where *d* is the diameter of the atoms or molecules, k_B the Boltzmann constant, and *T* the absolute temperature of the system.

Under conditions of UHV, the mean free path becomes larger or comparable to critical lengths of the system, such as the size of the chamber or the distance between the sources and the substrate, which, in the case of a research MBE chamber are in the order of 0.2-0.5m. This means that the growth system is under *free molecular flow* conditions: there is no interaction between particles along their paths, and the creation of atomic beams is thus allowed. Such conditions further allow for mechanical control of the atomic beams by switching on and off shutters that prevent or allow the reactants to reach the sample surface.

2.1.2 MBE Growth Chamber

In figure Figure 2.1, a standard MBE growth chamber is schematically presented along with all the basic elements that are included in it. The chamber itself consists of a stainless steel vessel with a diameter typically in the range of 0.5m. To maintain the low pressures necessary for UHV (which means typically in the order of ~10^{-11} torr), a combination of pumps are typically used, which may

include ion pumps, titanium sublimation, diffusion, and turbomolecular pumps. Additionally, extensive use of cryopanels is made to remove condensable contaminants (such as C0, $C0_2$, and H_2O), as well as to provide thermal insulation among the different heating parts. A quadrupole mass spectrometer is often used to monitor background species. The system also includes effusion cells for the production of the molecular beams, along with the respective shutters to switch them on and off. There is a substrate holder capable of withstanding heating temperatures up to several hundred degrees, and a loadlock system through where the samples are introduced into the chamber without compromising the UHV environment. Additionally, MBE typically gives the option of in-situ monitoring techniques, the most common of which is Reflection High Electron Diffraction (RHEED), as it will be discussed in greater detail in an upcoming section. For this, an electron gun is included, along with a fluorescent screen.[6]

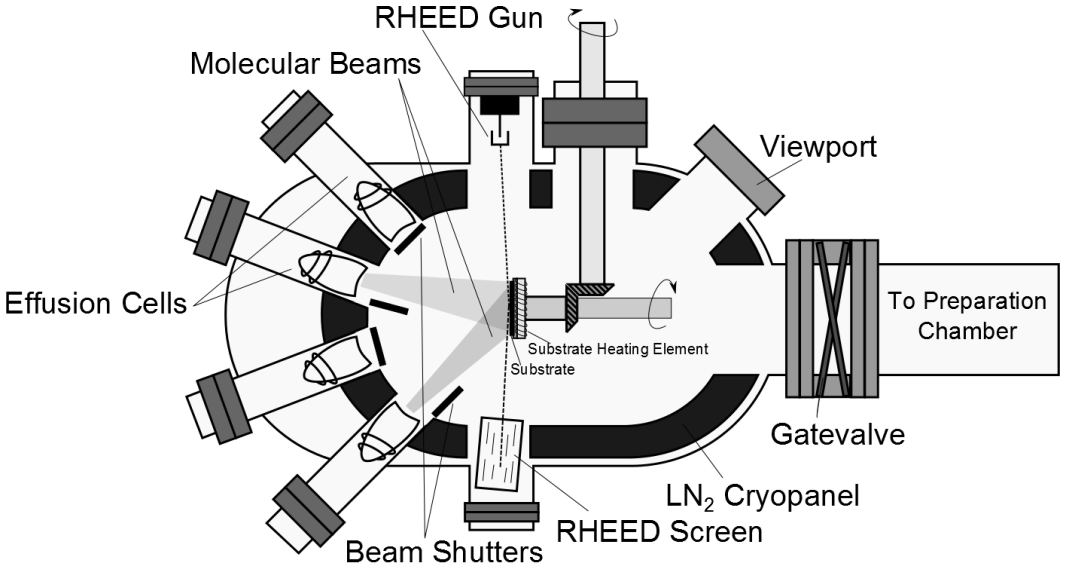

Figure 2.1: Schematic representation of an MBE growth chamber with standard elements.[7]

2.1.3 Thermal evaporation cells

The molecular beams are a very important part of MBE, and their purity and uniformity assures the effective operation and the product quality of the system. For their generations, a few types of sources have been developed, with the most widely used being the Knudsen cells, also referred to as thermal efussion cells, or thermal evaporation cells. In this case, the source materials are kept in crucibles, most commonly made of high-purity pyrolitic boron nitride (PBN), and the molecular beams are generated by thermal evaporation when they are heated at very high temperatures. The temperature of the cell is precisely controlled by closed-loop controllers in order to achieve high stability (in the order of tenths of a degree) and fast temperature changes[6].

According to Knudsen's[8] and Langmuir's[9] theories of evaporation, the flux of a species effusing from an orifice with area A_e depends on the equilibrium pressure of the evaporate at temperature *T*, *p(T)*, according to the following:

$$\Phi_e = A_e p(T) \left(\frac{N_A}{2\pi M k_B T}\right)^{1/2} \qquad (2.2)$$

where N_A, k_B, are the Avogadro's and Boltzmann constants respectively, and *M* the molecular weight. However, the flux that will eventually reach the substrate, additinonally depends on the

geometrical elements of the system, such as the distance between the cell and the substrate, as well as the angle between the cell and the substrate axes. As a result of the angular dependence, the incident flux can decrease rapidly as we move further away from the cell axis. To compensate for this, it is advisable to keep the substrate at continuous azimuthial rotation

Further geometrical factors, such as the shape of the crucible (conical or cylindrical), or its dimensions, can cause the final flux to diverge from what is predicted theoretically. For such reasons, actual fluxes are usually experimentally extracted from measurements of beam equivalent pressures by using gauges, or growth rates.

2.1.4 Plasma-Assisted MBE (PA-MBE)

For nitride growth, a source of nitrogen is necessary. N_2, however, is a chemically inert molecule which cannot be easily cracked thermally. Therefore, MBE growth of group-III nitrides requires the use of energetic nitrogen species. In order to accomplish that, compact remote plasma sources are employed; such include the electron cyclotrone resonance (ECR) microwave source, and the radio-frequency (RF) source, which is what was used for the present work. When an MBE system employs a plasma source, it is often referred to as *plasma-assisted MBE* (PA-MBE). Nitrogen plasma includes a variety of excited species, such as excited neutral molecules, ionized molecules, atoms, and ionized atoms. The exact composition of the nitrogen plasma can have a notable impact on RF MBE growth.[10]

For the RF generation of plasma, nitrogen is fed into the source by a mass flow controller. Subsequently, plasma is produced at 13.56MHz, with RF energy inductively coupled through a water-cooled copper coil. Nitrogen plasma is contained in a cylindrical PBN discharge tube, until it is supplied in the chamber to interact with the atomic beams on the sample surface, so that epitaxial growth can take place.

2.1.5 Reflection High Energy Electron Diffraction (RHEED)

In-situ monitoring for MBE is crucial, as it provides insight on the growth process, which translates into better control of the conditions, and, consequently better results. Reflection High Energy Electron Diffraction (RHEED) is the preferred method for MBE monitoring.[6]

The RHEED technique requires an electron gun, which produces a collimated electron beam that is accelerated by energies of 10-50keV. The beam is then diffracted from the sample surface where it hits at a very small angle (0.5-2^{o}). The diffraction patterns are then picked up on a fluorescent screen.

Constructive interference takes place where the Ewald sphere intersects with the reciprocal lattice. The Ewald[11, 12] sphere is centered at the point where the electron beam hits the sample surface and has a radius equal to the wavenumber of the beam. In the case of a smooth surface, the reciplrocal lattice consists of parallel rods, as it is drawn in figure 2.2, due to the fact that, under grazing incidence, electrons are diffracted by only a few monolayers of crystal, which is equivalent to a 2D lattice. For a rough surface, the electrons are diffracted from the 3D lattice of the crystal, and the reciprocal space consists then of spots. A necessary condition for the technique is that the radius must be much larger than the distance between the lattice rods/points. Then, the RHEED diffraction

pattern that appears on the fluorescent screen consists of streaks, for the smooth growth surface, or spots, for rough surfaces.

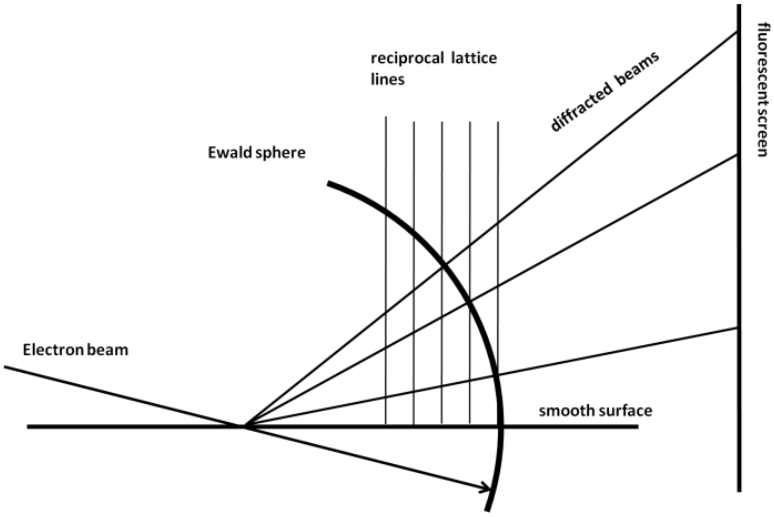

Figure 2.2: Schematic representation of the origin of RHEED diffraction patterns from a smooth surface characterised by a reciprocal lattice of rods; the intersections of the Ewald sphere with the rods of the reciprocal lattice define diffracted patterns visualised on a fluorescent screen

RHEED's significance lies in monitoring of the growth process in real time, and accommodating the instant adjustment of the growth conditions. RHEED monitoring can also provide a number of additional information: extraction of growth rates from RHEED intensity oscillations, observation of surface reconstruction, removal of oxides for surface study and preparation, temperature calibration, and so on.[13]

2.2 X-ray Diffraction

X-ray diffraction is an essential tool for the structural characterization of crystal films and devices. It is an ex-situ, non-destructive technique that can be applied to provide such versatile information, as determination of the crystal lattice parameters, which in turn can be used to extract alloy composition and/or strain relaxation, misorientation, crystallite size and microstrain, superlattice thicknesses, as well an assessment of the crystal quality, including information on defect types and densities, film uniformity and phase separation, and alloy ordering.[14]

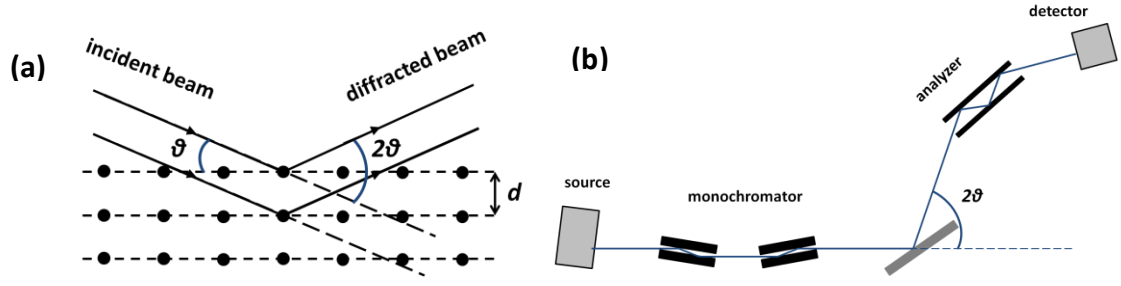

Figure 2.3: (a) Illustration of the conditions required for Bragg diffraction. (b) Standard high-resolution diffraction configuration

When incoming monochromatic x-rays of λ wavelength are directed at a crystal lattice, they are scattered by the crystal planes. Constructive interference of the scattered x-rays occurs according to Bragg's law:

$$n\lambda = 2dsin\theta \quad (2.3)$$

where *d* is the spacing between the planes of the crystal lattice, from which diffraction is occurring, ϑ is the angle between the incident rays and the scattering planes, and *n* is an integer determined by the order (figure 2.3a). Each set of crystal planes is characterized by a spacing $d_{h\,k\,l}$, which, in the case of a hexagonal lattice, with parameters, *c*, and *a*, is given by

$$\frac{1}{d_{h\,k\,l}^2} = \frac{4}{3}\frac{h^2+k^2+hk}{a^2} + \frac{l^2}{c^2} \quad (2.4)$$

where (hkil) the Miller notation that describes the group of planes. For each group of planes, a diffraction spot is created in the reciprocal space with position inversely related to the spacing d [15].

For the most part, nitride single crystal or heterostructure characterization by XRD requires a high resolution (HR) diffractometer (figure 2.3b). This means that the x-rays employed in the experimental setup need to be constricted both spatially, and in terms of wavelength. In such a case, x-rays are generated by bombarding a metal, typically copper, with electrons in an evacuated tube. Subsequently, a monochromator is used to reduce the incident beam divergence to as low as 0.3°, and eliminate unwanted wavelengths[14]. Most commonly, the value of the x-ray wavelength used is the Cu Kα1 *λ=1.5405975*Å. The incident beam next hits the sample at an angle ω, as shown in the figure. A detector is used to measure the intensity of the diffracted beam, as well as and the angle 2ϑ to determine the plane spacing. When the detector remains open, the setup is called 'double axis'. There is, however, the option of inserting an additional analyzer crystal before the detector to increase the resolution of the 2ϑ measurement, in which case the experimental setup becomes 'triple-axis'.

An HR diffractometer can perform a large number of different scan types. Some of the most common include *ω-2ϑ* scans, in which the sample is rotated by ω, while the detector is rotated by 2θ, and which are typically used to measure the lattice parameters, as well as to evaluate composition and uniformity, *ω*-scans, in which the same is rotated while the detector remains at a fixed position, and whose broadening, with open detectors, is generally used to assess crystal quality, *φ*-scans, which include rotation of the samle in the plane, and can be used to measure misorientation, and so on. The setup can also be used to map the reciprocal space, which provides with much information on interplanar spacings, strain relaxation, and defect-related broadening.

2.2.1 Lattice parameter determination

X-ray diffraction is a very precise method for the measurements of lattice parameters, with precisions in the order of 10^{-4} Å, or lower. If the diffractometer is properly calibrated for $\vartheta=0$, then Bragg's law can be used to extract the interplanar spacing *d* from the angle 2ϑ, for a specific reflection (*hkl*), and subsequently eq. (2.4) can be used to relate this information to the lattice parameter values, for a hexagonal system. Since there are two unknown variables, *a*, and *c*,

measurements at at least two different reflections are needed to determine them. For nitride semiconductors with (0001) surfaces, this usually means a symmetric reflection (meaning $2\omega \approx 2\vartheta$), from which the *c* lattice constant can be directly determined, and one asymmetric ($2\omega \neq 2\vartheta$) reflection, typically (105), or (104).

High precision Bond method

To eliminate misalignment errors in the lattice constant measurement, the Bond method[16] is often employed. In this approach, the same reflection is measured at both positive and negative 2θ values (also referred to as grazing incidence, and grazing exit measurements). The interplanar spacing can then be calculated from the difference between the crystal setting, $\Delta\omega$. Because this method has low sensitivity to alignment errors, a 'double-axis' setup with an open detector can be used, which allows for higher intensities and faster measurements. For hexagonal crystals[17, 18], for a (*hkl*) reflection, it can be written that

$$\frac{c}{a} = \sqrt{\frac{3}{4}\left(\frac{1}{cos^2\Delta\omega - 1} - 1\right)\left(\frac{l^2}{h^2+k^2+hk}\right)} \qquad (2.5)$$

so that, if the c lattice constant is known, possibly from a symmetric HR scan, then the a lattice can be found by performing Bond measurements for an asymmetric reflection, most commonly 105.

2.2.2 Alloy composition and strain relaxation

With the lattice parameters *a*, and *c* precisely measured, the composition of a ternary alloy can be extracted. However, the calculation is not straightforward, as the lattice parameters of alloys are affected by strain, as well as composition

For a fully relaxed alloy, the crystal parameters depend on the composition according to Vegard's law[19], which states that they will vary linearly between the alloy endpoints. In the case of InGaN, this means:

$$c_0^{In_xGa_{1-x}N} = c_0^{GaN}(1-x) - c_0^{InN}(x) \quad (2.6)$$

$$a_0^{In_xGa_{1-x}N} = a_0^{GaN}(1-x) - a_0^{InN}(x) \quad (2.7)$$

For an unstrained crystal, therefore, it is possible to calculate the composition by measuring a single lattice constant. On the other hand, for cases of strained material, the measured lattice constants can deviate significantly from those dictated by Vegard's law. It is possible, however, to obtain the relaxed values of the lattice constants, from the measured ones, assuming elastic strain in the crystal. Then, the out-of-plane strain will be related to the in-plain strain according to the following[20]

$$\frac{c_{meas} - c_0}{c_0} = -\frac{2C_{13}}{C_{33}}\left(\frac{a_{meas} - a_0}{a_0}\right) \qquad (2.8)$$

where c_{meas} and a_{meas} are the measured lattice constants, c_0, and a_0 are the relaxed constants, which can be assumed to follow Vegard's law, and C_{13}, C_{33} are the elastic constants for InGaN alloy with composition *x*[14]. The elastic constants can in turn be assumed to follow Vegards law:

$$C_{13} = C_{13}^{GaN}(1-x) - C_{13}^{InN}(x) \qquad (2.9)$$

$$C_{33} = C_{33}^{GaN}(1-x) - C_{33}^{InN}(x) \qquad (2.10)$$

Values for the elastic constants for GaN, and InN can be found in Table II[21]

Solving the above equations will yield the film's composition, as well as the relaxed values for the lattice parameters. The strain relaxation of the crystal with relation to the substrate lattice parameter a_0, can also be calculated, according to:

$$R = \frac{a_{meas} - a_s}{a_0 - a_s} \times 100\% \quad (2.11)$$

	GaN	InN
C_{13}	101±4	85±3
C_{33}	395±5	236±6

Table II: Values for the elastic constants for GaN, and InN, reference [21]

2.3 Atomic Force Microscopy

Atomic force microscopy (AFM)[22], or scanning force microscopy, is a high resolution tool for imaging, measuring and manipulating matters at micro- or nano-scale. It is widely used for the characterization of surface morphologies, and measuring surface roughness.

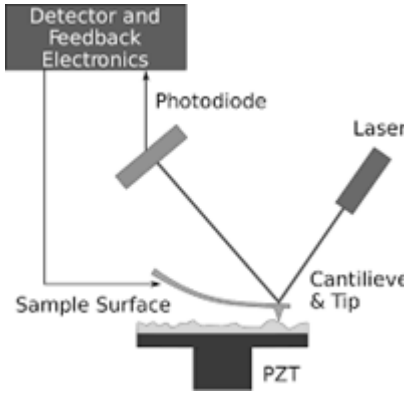

Figure 2.4: Block diagram of atomic-force microscope using beam deflection detection. [23]

Figure 2.4 presents the standard configuration of AFM. A cantilever with size of a few millimetres, with a sharp tip (radius of curvature in the order of a few tens of nanometer) at its apex, is used to scan the sample surface line by line. The tip is excited at a resonant frequency with oscillation amplitude in the order a few nanometers. The deflection of the cantilever resulting from atomic force interaction is measured by a pair of laser and photo-detector. Measuring the tip-to-sample distance at each point allows the scanning software to construct a topographic image of the sample surface. An AFM system can operate in three modes defined by whether or not the tip is in contact with the sample surface during the measurement: non-contact mode, which means the tip does not touch the surface, at any point, taping mode, in which the tip touches the surface once every oscillation, and contact mode, which means the tip is in contact with the sample surface for the duration of the measurement.

2.4 Scanning electron microscopy (SEM)

Scanning electron microscopy (SEM)[24] is an electron technique for the imaging of materials in the ranges of micrometers or smaller.. SEM is similar to light microscopy except that electrons are used instead of photons. This means that much larger magnification is possible, since the electron wavelength is much smaller than the photon wavelength and the depth of field is higher.

An electron gun typically generates the electron beam by thermionic emission in vacuum. The electron beam, accelerated by energies of up to 40keV is subsequently focused by a series of lenses and scans the sample surface. As a result of the interaction of the electrons with the sample, there is generation of secondary electrons, backscattered electrons, auger electrons, as well as x-ray radiation. The image in a SEM is produced by detecting secondary electrons. The secondary electrons are collected and their density is amplified and displayed on a cathode-ray tube (CRT). These can be focused, deflected and accelerated using appropriate potentials, to adjust focus and magnification.

2.5 Transmission electron microscopy

Transmission electron microscopy (TEM) operates on the same basic principles as the light microscope but uses electrons instead of light. Since the wavelength of electrons is much smaller than that of light, the optimal resolution for TEM images is many orders of magnitude better than that from a light microscope. Thus, TEM images can reveal the finest details of internal structure - in some cases as small as individual atoms, which makes it an important tool for structural characterization of semiconductor crystals, as it can provide information on lattice parameter, strain relaxation and alloy composition, defect types and dislocation densities, and so on.

For the TEM technique, a beam of electrons hits an ultrathin (less than 100nm) section of a sample. Subsequently, the portion that is transmitted through the sample is focused into an image on phosphor screen or charge coupled device (CCD) camera. If the sample is illuminated by parallel electron beam then this geometry is termed as selective area electron diffraction (SAED). If a convergent beam is incident on the sample, it generates diffraction patterns over several incident angles. This geometry is called as convergent beam electron diffraction (CBED). Preparation of samples for TEM typically includes processes such as ultrasonic disk cutting, dimpling, and ion-milling, to make them adequately thin for the technique.

2.6 Spetrospopic Ellipsometry

Ellipsometry is a non-destructive technique that determines a material's optical and dielectric properties by using polarized light and measuring the change in the polarization. It can be used to calculate dielectric and optical constants, thin film thickness, alloy composition, and so on.

The principle of ellipsometry is shown in figure 2.5. A light source emits light that is linearly polarized by a polarizer. The light beam is then reflected from the sample surface and the change in its polarization is measured. The polarization state of the light incident upon the sample may be decomposed into an *s* and a *p* component (the *s* component is oscillating perpendicular to the plane of incidence and parallel to the sample surface, and the *p* component is oscillating parallel to the

plane of incidence). The Fresnel reflection coefficients R_p, and R_s, are given by the ratio of the amplitudes of the polarization components after and before reflection. Ellipsometry determines the complex reflectance ratio ρ is determined, which related to the Fresnel coefficients according to the following:

$$\rho = \frac{R_p}{R_s} = \tan\psi\, e^{i\Delta} \qquad (2.12)$$

which can be expressed with an amplitude and a phase component, ψ, and Δ respectively.

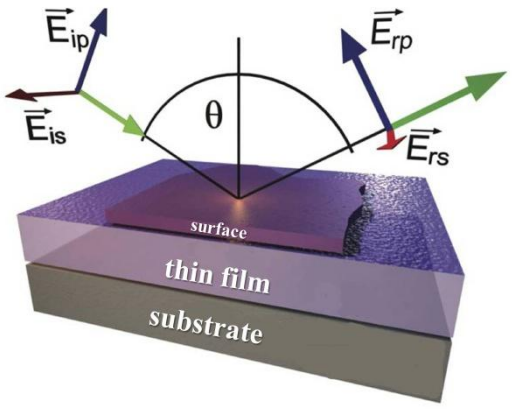

Figure 2.5: Typical ellipsometry configuration, where linearly polarized light is reflected from the sample surface and the polarization change is measured to determine the sample response.

2.7 Photoluminescence spectroscopy

Photoluminescence spectroscopy is a contactless, non-destructive method of probing the electronic structure of materials. It is used for band gap determination, to study impurity levels and defects in semiconductors, recombination mechanisms, and so on.

A laser is directed onto a sample, where light is absorbed and photo-excites electrons in the semiconductor. When these electrons return to their equilibrium states, the excess energy can be released by a radiative and/or nonradiative process. The radiative process is called *photoluminescence*. Photouminescence is analyzed by a spectrometer and the peaks in the spectra represent a direct measure of the energy levels in the semiconductor.[25]

2.8 Hall effect measurements

The Hall effect[26] is a well-established, reliable method to characterize the electrical properties of semiconductors, such as the carrier type, carrier density and mobility, and the material resistivity. Some additional advantages of the method include simplicity, low cost, and fast results

The principle of the Hall effect, lies in the Lorentz force and is shown in figure 2.6: When a carrier moves along an electric field (here, this means a current, *I*), and a magnetic field is applied perpendicular to its direction, then it experiences a magnetic force that is normal to both the direction of the current, and the direction of the magnetic field. Carriers subjected to the Lorentz's force will drift away from the current direction, which will result in a potential drop across the width

of the sample. This is called the Hall voltage, V_H. The Hall voltage is related to the carrier density n according to:

$$V_H = \frac{IB}{qnd} \qquad (2.13)$$

where B is the magnitude of the magnitude of the magnetic field, q=1.602 10-19C the elementary charge, and d the thickness of the sample.[25]

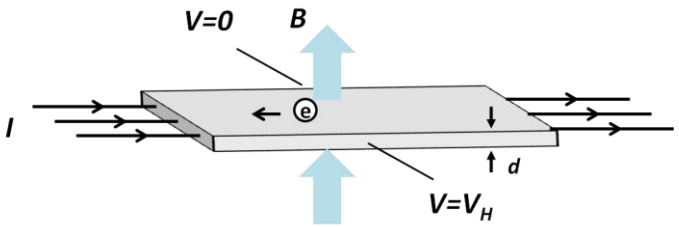

Figure 2.6: Schematic representation of the Hall Effect measurement principles.

The carrier mobility μ can then also be determined according to

$$\mu = \frac{1}{qn_sR_s} \qquad (2.14)$$

where n_s=nd is the sheet carrier density, and R_s the sheet resistance.

Van der Paue Method

To determine both the carrier density and the resistivity of a semiconductor, the Van der Paue[27] configuration is often employed, which uses an arbitrary shape, thin-plate sample containing four small ohmic contacts places peripherically. A series of measurements are performed, where current is applied in two of the four contacts and the voltage that arises at the other two contacts is then measures. For the resistivity part of the measurement, no magnetic field is applied, whereas the Hall measurements take place under magnetic field. The specifics of the measurements and the combinations of contact pairs can be found in the literature.[28]

2.9 Specifications

For the present work, all the samples discussed in the following chapters were grown in a 32P RiBER system equipped with Knudsen cells for the evaporation of group III elements. Active nitrogen species were supplied by an Oxford HD25 plasma source operating at 13.56MHz[29]. For gallium and indium, beam equivalent pressures at the position of the substrate were measured by an ion gauge; subsequently, those values were calibrated to respective group III element arrival rates by measuring deposition rates of films grown under nitrogen excess. Similarly, RF source operating conditions were calibrated to nitrogen arrival rates by determining deposition rates for films grown under metal excess. RHEED was used for in-situ monitoring of the growth, operating at 15kV. To record the transient variation of the RHEED intensity, an experimental setup was developed. A photodiode was used to monitor the intensity in real time, and subsequently the signal was aplified

and recorded by a computer[30]. A low pass filter was also used for the elimination of high frequencies. Substrate temperature was monitored at all times by a thermocouple located on the backside of the substrate. Since the thermocouple reading in MBE systems can diverge dramatically from the actual temperature value, temperature points were calibrated by use of a pyrometer. Black body emission of the substrate was collected[31] through the chamber window; emissivity was determined by comparing the pyrometer reading against well-defined temperature values ex-situ.

Prior to growth, the backsides of the wafers were coated with molybdenum to ensure efficient radiation heating. All samples were cleaned using standard degreasing procedures, and dried with nitrogen. Subsequently, they were mounted onto Si holders using indium bonding. Before transferring them to the growth chamber, samples were baked at 600° C for 30min. Upon introduction in the growth chamber, the sample surface was cleaned by Ga deposition and subsequent annealing to remove oxidation[32]. Following removal from the growth chambers, all samples were cleaned from excess indium with HCL.

High resolution x-ray diffraction (HR-XRD) measurements were performed using a Bede D1 triple-axis x-ray diffractometer to determine the films' lattice parameters. Typically, the *c* lattice parameter was determined from a symmetrical (0002) HR ω-2ϑ scan, and the *a* lattice parameter from measurement of the $(10\bar{1}5)$ Bragg reflection, using the Bond method. For the determination of InGaN alloy composition, Vegard's law and biaxial strain dependence were assumed, after the lattice parameters were determined.

A Digital IIIa Nanoscope AFM was used to study ex situ the films' surface. Transmission electron microscopy (TEM) characterization was performed at the Aristotle University of Thessaloniki. Observations of the heterostructures were performed in cross sectional geometry using a 200 kV JEOL JEM 2011 microscope. SEM images were acquired with a 7000 Joel microscope. Optical dielectric functions of InGaN thin films were obtained from the analysis of the spectroscopic ellipsometry data acquired using a rotating analyzer J.A. Woolam VASE. Measurements were performed at room temperature in the photon energy range of 0.92–4eV at 65°, 70° and 75° angles of incidence. Films' thickness was estimated through the Cauchy dispersion model applied in the transparent region. The electronic properties of the films were studied by resistivity and Hall effect measurements at room temperature, using van der Pauw (vdP) method and a magnetic field of 0.30 T. The photoluminescence of the InGaN films was excited with a Kimmon 25 mW continuous wave He–Cd laser (λ=325 nm). Samples were mounted in an APD helium closed-circuit cryostat and PL measurements were carried out at 15K and room temperature. The signal was recorded with an Acton 0.5 m focal length imaging spectrograph, equipped with a 150 gr/mm holographic grating and a charge-coupled device camera. Lastly, for solar cell characterization, a LOT-Quantum Design full spectrum solar simulator LS0608 equipped with a 1000W ozone free Xe arc lamp, and a class AAA Air Mass 1.5 global filter, and a Keithley Series 2600B System Source Meter were used

REFERENCES

1. Cho, A.Y., *Epitaxial Growth of Gallium Phosphide on Cleaved and Polished (111) Calcium Fluoride.* Journal of Applied Physics, 1970. **41**(2): p. 782-786.
2. Cho, A.Y., *Morphology of Epitaxial Growth of GaAs by a Molecular Beam Method: The Observation of Surface Structures.* Journal of Applied Physics, 1970. **41**(7): p. 2780-2786.
3. Shelton, H. and A.Y.H. Cho, *Evaporative Lifetimes of Copper, Chromium, Beryllium, Nickel, Iron, and Titanium on Tungsten and Oxygenated Tungsten.* Journal of Applied Physics, 1966. **37**(9): p. 3544-3548.
4. Cho, A.Y. and J.R. Arthur, *Molecular beam epitaxy.* Progress in Solid State Chemistry, 1975. **10**: p. 157-191.
5. Cho, A.Y., *How molecular beam epitaxy (MBE) began and its projection into the future.* Journal of Crystal Growth, 1999. **201–202**: p. 1-7.
6. Henini, M., *Molecular beam epitaxy : from research to mass production*. 2013.
7. Wikipedia. 2013 [cited 2017; Available from: https://commons.wikimedia.org/wiki/File:Molecular_Beam_Epitaxy.png.
8. Knudsen, M., *Die maximale Verdampfungsgeschwindigkeit des Quecksilbers.* Annalen der Physik, 1915. **352**(13): p. 697-708.
9. Langmuir, I., *The Vapor Pressure of Metallic Tungsten.* Physical Review, 1913. **2**(5): p. 329-342.
10. Morkoç, H. and I. Wiley. *Handbook of nitride semiconductors and devices*. 2008; Available from: http://onlinelibrary.wiley.com/book/10.1002/9783527628438.
11. Ewald, P.P., *Zur Begründung der Kristalloptik.* Annalen der Physik, 1917. **359**(23): p. 519-556.
12. Ewald, P., *Introduction to the dynamical theory of X-ray diffraction.* Acta Crystallographica Section A, 1969. **25**(1): p. 103-108.
13. Wang, X. and A. Yoshikawa, *Molecular beam epitaxy growth of GaN, AlN and InN.* Progress in Crystal Growth and Characterization of Materials, 2004. **48-49**: p. 42-103.
14. Moram, M.A. and M.E. Vickers, *X-ray diffraction of III-nitrides.* Reports on Progress in Physics, 2009. **72**(3): p. 036502.
15. Fewster, P.F., *X-Ray Scattering From Semiconductors (2nd Edition).* 2003.
16. Bond, W., *Precision lattice constant determination: erratum.* Acta Crystallographica Section A, 1975. **31**(5): p. 698.
17. Herres, N., et al., *X-ray determination of the composition of partially strained group-III nitride layers using the Extended Bond Method.* Materials Science and Engineering: B, 2002. **91–92**: p. 425-432.
18. Fatemi, M., *Absolute measurement of lattice parameter in single crystals and epitaxic layers on a double-crystal X-ray diffractometer.* Acta Crystallogr A, 2005. **61**(Pt 3): p. 301-13.
19. Vegard, L., *Die Konstitution der Mischkristalle und die Raumfüllung der Atome.* Zeitschrift für Physik, 1921. **5**(1): p. 17-26.
20. Schuster, M., et al., *Determination of the chemical composition of distorted InGaN/GaN heterostructures from x-ray diffraction data.* Journal of Physics D: Applied Physics, 1999. **32**(10A): p. A56.
21. Morales, F.M., et al., *Determination of the composition of InxGa1–xN from strain measurements.* Acta Materialia, 2009. **57**(19): p. 5681-5692.
22. Binnig, G., C.F. Quate, and C. Gerber, *Atomic Force Microscope.* Physical Review Letters, 1986. **56**(9): p. 930-933.
23. Askewmind at English Wikipedia. 2006 2017]; Available from: https://commons.wikimedia.org/wiki/File:Atomic_force_microscope_block_diagram.png.
24. von Ardenne, M., *Das Elektronen-Rastermikroskop.* Zeitschrift für Physik, 1938. **109**(9): p. 553-572.

25. Sze, S.M. and K.K. Ng, *Physics of semiconductor devices*. 2007, New Jersey: John Wiley & Sons.
26. Hall, E.H., *On the new action of magnetism on a permanent electric current.* American Journal of Science, 1880(117): p. 161-186.
27. van der PAUYV, L., *A method of measuring specific resistivity and Hall effect of discs of arbitrary shape.* Philips Res. Rep, 1958. **13**: p. 1-9.
28. Schroder, D.K., *Semiconductor material and device characterization*. 2006, [Piscataway, NJ]; Hoboken, N.J.: IEEE Press ; Wiley.
29. Iliopoulos, E., et al., *Active nitrogen species dependence on radiofrequency plasma source operating parameters and their role in GaN growth.* Journal of Crystal Growth, 2005. **278**(1-4): p. 426-430.
30. Χέβας, Λ., *Ανάπτυξη πειραματικής διάταξης μέτρησης έντασης δέσμης RHEED σε σύστημα MBE και μελέτη της εκρόφησης Γαλλίου από υποστρώματα GaN*, in *Department of Physics*. 2017, University of Crete: Heraklion.
31. Bertness, K.A., et al., *In situ temperature measurements for selective epitaxy of GaN nanowires.* physica status solidi (c), 2014. **11**(3-4): p. 590-593.
32. Bermudez, V.M., D.D. Koleske, and A.E. Wickenden, *The dependence of the structure and electronic properties of wurtzite GaN surfaces on the method of preparation.* Applied Surface Science, 1998. **126**(1): p. 69-82.

CHAPTER 3: Temperature effects on InGaN alloys grown by MBE

3.1 Introduction

As it was mentioned in previous chapters, MBE growth is the complicated result of the combination of a large number of physical processes[1]. Some of these include, element adsorption, surface diffusion[2-4], metal desorption from the sample surface[5, 6], and thermal decomposition[7, 8], all of which depend greatly upon temperature. As a matter of fact, the temperature dependence of such mechanisms is a lot of the times much more complex than a straightforward Arrhenius[9] formula. In the case of alloy epitaxy, the complexity increases with the number of constituents, as for each of them there is a separate set of parameters to describe such processes, and how they are affected by temperature. For the focus of the present study, InGaN ternary alloys, one must also take into consideration mechanisms that affect the alloy quality, such as indium segregation[10, 11], and phase separation[12, 13], as those have already been mentioned, and which also depend heavily on temperature. The homogeneity problems of the InGaN material have been previously discussed. According to Ho and Stringfellow's[14] calculation of the binodal and spinodal curves for the InGaN system, the miscibility gap between the alloy constituents decreases dramatically as the temperature increases. The difficulty to grow uniform alloys especially increases for compositions larger than 20% InN[15, 16], as the miscibility gap shrinks to zero for the 50% point. Even though the theoretical prediction is discouraging, experiments show that, with MBE, it is not impossible to develop uniform InGaN films across the compositional range, by employing techniques such as Metal-Modulated epitaxy[12] or droplet-elimination by radical-beam irradiation[17], or by decreasing the growth temperature[18].

In this chapter, we will attempt to investigate the effect of substrate temperature on the MBE growth of InGaN films. This includes a qualitative study of how kinetic processes affect growth conditions, and In incorporation, the role temperature plays in film structural quality, phase separation, and strain relaxation mechanisms, as well as its relationship with optical and electronic qualities of the material.

To investigate the effects of substrate temperature on the properties of InGaN alloys two separate series of samples were grown by MBE, and are studied in this chapter. For each of the two series, the substrate temperature (T_{gr}) was varied over a wide range, from 400^{o} C to 600^{o} C, while the rest of the growth parameters were kept constant. These include the active nitrogen, and metal arrival rates, and the deposition time. For the first series, here on denoted S1, the total arrival rate for metal atoms (meaning the sum of the indium and gallium arrival rate) is greater than the arrival rate for active nitrogen (N*). The second series, denoted S2, includes samples with the same metal arrival rates as S1, but the nitrogen rate is raised, so that it is higher than the total metal rate. This means, that growth for S1 samples took place under nominally slightly metal-rich conditions, and nominally under N-rich conditions for S2 samples. All of the parameters for the two series are

presented in Table III. Arrival rates are all given in GaN equivalent thickness nm/h. All films were grown on high resistivity Fe-doped GaN(0001)/c-Al2O3 commercial templates.

	Series S1	**Series S2**
Ga rate (nm/h)	135	135
In rate(nm/h)	115	115
N* rate (nm/h)	235	280
Deposition time	2 hrs	2 hrs

Table III:Arrival rates for Ga, In, N, for series S1, and S2

It should be noted at this point, that there is a difference between the nominal growth rates, as these are shown above, and the actual growth conditions as these are manifested on the sample surface during epitaxy. This is due to the fact that growth processes, namely indium desorption, and InGaN thermal decomposition, have a restrictive effect on indium arrival rates and nitrogen rates respectively. Since these processes are highly dependent on temperature as we have discussed above, the effective growth conditions will also vary with temperature. This is made evident by the results of the study, as we will discuss below. However, before we continue, it is very useful to consider the mechanics of this restriction, as well as the effects on indium incorporation.

3.2 Preliminary discussion: definitions and basic concepts

Since the nominal arrival rates can often give a misleading impression as to what the actual growth conditions are, it is worthwhile to distinguish between the nominal arrival rates, and what we will refer to as the *effective* rates, which are representative of the growth regime. The effective rates depend on the nominal rates, as well as the kinetic processes that take place, as it is discussed in the following.

As far as metal rates are concerned, impinging atoms will eventually either be incorporated into the lattice, or desorb from the sample surface. Therefore, the main mechanism that limits the effective rates of metal is desorption, so that effective rates for Ga and In respectively are given by:

$$F'_{Ga} = F_{Ga} - F_{Ga}^{des} \qquad (3.1)$$

$$F'_{In} = F_{In} - F_{In}^{des} \qquad (3.2)$$

where F_{Ga}, F_{In} the nominal rates of Ga, and In, and F_{In}^{des}, F_{Ga}^{des} the desorption rates. Desorption rates obviously depend heavily on substrate temperature T_{gr}, however, the exact function dependence will not be discussed here, as it is investigated in greater detail in the following chapters. It is worth mentioning however, that for the temperatures discussed in this work, the desorption of Ga is found to be very low[19], and can be neglected for the rest of the discussion, so that $F'_{Ga} = F_{Ga}$.

As for the active nitrogen atoms, they are incorporated into the lattice as long as there is enough metal on the growth surface, so that desorption does not play an important role. However, once they have been incorporated, it is not unlikely that these bonds will break again, due to thermal decomposition. Decomposition can be ignored for GaN, or AlN growth, since it is very limited for the temperatures used. For InN, and InGaN epitaxy though, the decomposition rates can be quite significant for the temperature range used in the experiments. It has been demonstrated by

Kobmuller et al.[20] that, one can consider the decomposition rate as N atoms leaving the sample surface, so that the effective nitrogen rate becomes:

$F_N' = F_N - F_{InGaN}^{Dec}$ (3.3)

where, F_N, the nominal N arrival rate, and F_{InGaN}^{N} the decomposition rate. The determination of the InGaN decomposition rate becomes even more convoluted, since it is a function of not only temperature, but also the composition of the alloy. It is expected that decomposition rates will be higher for higher indium contents, since the In-N bond is much weaker than the bond between Ga and N, and, therefore, decomposition rate of InN is much larger than GaN. Again, extensive discussion of how we can estimate the decomposition rates will follow in upcoming chapters.

It now becomes obvious how effective growth conditions can deviate from those dictated by nominal arrival rates. Especially as we go to higher growth temperatures, desorption and decomposition rates can become very high and alter effective rates dramatically. It is effective conditions that determine the result of the experiment, including crystal quality, film properties, surface morphology, and, of course, InGaN composition. Let us first consider effective N-rich conditions. This means that the total effective metal rate $F_{In}' + F_{Ga}'$ is lower than the amount of nitrogen, thus resulting in an excess of nitrogen atoms on the growth surface. In this case, the In content *x* of the resulting $In_xGa_{1-x}N$ alloy should be straightforward[21]:

$x = \frac{F_{In}'}{F_{In}' + F_{Ga}'}$ (3.4)

The growth rate, additionally, should amount to $F_{In}' + F_{Ga}'$.

However, for effective nitrogen-limited conditions, the total metal effective rate $F_{In}' + F_{Ga}'$ becomes larger than the effective nitrogen rate. In this case, it has been found[22, 23] that gallium is preferentially incorporated into the film. Gallium incorporation in this case depends only on the available metal sites (defined here by the available nitrogen F_N' on the surface), and consequently the incorporation of indium depends on the available vacant sites remaining. Whatever excess indium is not incorporated then accumulates on the sample surface in the form of indium droplets. The effective nitrogen rate corresponds to the growth rate The In content can then be found according to the following:

$x = 1 - \frac{F_{Ga}'}{F_N'}$ (3.5)

To illustrate the points made above, two additional series of samples will be discussed in this section. For series S3, parameters that were kept constant include the nominal nitrogen arrival rate at 235 nm/h GaN eq, substrate temperature at 520° C, gallium nominal arrival rate at 115 nm/h GaN eq, and deposition time at 2hrs. Indium arrival rates were varied from approximately 50 nm/h GaN eq to approximately 170 nm/h GaN eq, which means conditions for these samples change from the nominally N-rich to the nominally metal-rich regime. For series S4, nominal N rate, temperature, and deposition time were also kept constat at 280nm/h GaN eq, 520° C, and 2hrs respectively. This time, the total nominal metal rate $F_{Ga}+F_{In}$ was unchanged at approximately 210nm/h GaN eq for each of the samples within the series, so that all of them are grown at nominally N-rich conditions. The nominal III/V ratio is then fixed at ~0.75. The In rate to total metal rate $F_{In}/(F_{In} + F_{Ga})$ was then changed from approximately 15% to approximately 75%. Again, high resistivity GaN(0001)/*c*-Al_2O_3 wafers were used as substrates. In contents for the samples were measured by HR-XRD, as per the specifications of chapter 2.

Figure 3.1 shows the results for the series S3 (fig. 3.1a) and S4 (fig 3.1b). For S3 samples, as the indium rate increases, the growth regime changes from N-rich (or metal-limited) to metal-rich (or N-

limited. In the N-rich regime, the InN mole fraction increases linearly with the indium flux, as is predicted by equation (3.4). Once we switch to the metal-rich growth conditions, the InN mole fraction of the films reaches a saturation. This, again, is in agreement with equation (3.5) which suggests that, under metal excess, increasing the indium rate does not affect composition, which depends solely on Ga and N effective rates. It is worth noting, however, that the switch between regimes according to nominal rates should happen at the boundary marked by the dashed red line, not by the solid red line. The saturation value of the InN mole fraction, approximately 0.4, is also not successfully predicted by nominal values. This confirms that the regime depends on effective rates, rather than on nominal ones. Taking the previous discussion into account, and assuming that within the series, the decomposition and desorption rates are constant, we can extract that $F_{InGaN}^{Dec} \approx 45$nm/h GaN eq, and $F_{In}^{des} \approx 15$nm/h GaN eq.

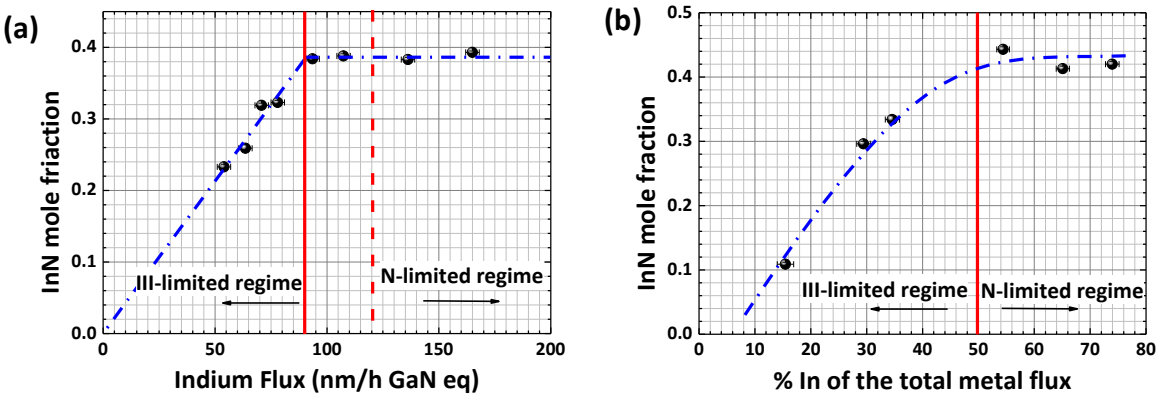

Figure 3.1: (a) InN mole fraction as a function of the indium arrival rate for series S3. The red dashed and solid lines mark the change from metal-rich to nitrogen-rich conditions according to nominal and effective conditions respectively (b) InN mole fraction as a function of the In over total metal ratio for series S4. The red line marks the change from metal-rich to nitrogen-rich conditions. The blue dashed lines in both figures are guides for the eye.

The distinction between effective and nominal conditions is even more obvious for series S4. Nominal rates for S4 suggest that all samples should have been grown under N-rich conditions, and the dependence of InN mole fraction on In rate should be linear. However, for high enough indium fluxes, InN mole fraction reaches the limit associated with metal-rich conditions. In this case, the decomposition rates increases as the ratio of In to metal rate becomes higher. After it reaches a critical value (the boundary of the red line in figure 3.1b) it causes the conditions to switch to metal-limited. Again, the dependence of both desorption and decomposition on conditions is a complicated subject, not very well understood, and will be investigated in detail in following chapters.

For both series, samples in the N-limited regime, as shown in figure 3.1, exhibited indium droplets on the surface after they were removed from the growth chamber, adding to our interpretation concerning effective growth conditions.

3.3 In incorporation and effective conditions

Returning to the study of the substrate temperature and its effects, figure 3.2a presents the InN mole fraction of the samples included in series S1 and S2, as it was measured by HR-XRD (see chapter 2 for specifications). The red squares and blue circles represent samples of S1, and S2 respectively. The reader is reminded that S1 conditions are nominally metal-rich, while S2 conditions are nominally nitrogen-rich.

There is a clear trend of the InN mole fraction decreasing as the temperature rises. This obviously means there is a restriction of indium incorporation into the alloy that becomes stronger the higher the substrate temperature. To discuss temperature effects, we have divided figure 3.2a into three sections. Representative RHEED images for each of these sections are shown in figure 3.2b.

Section (I) concerns samples that belong only to S2, for very low growth temperatures. In fact, the temperature here is low enough, so that both indium desorption and thermal decomposition can be considered negligible. This means that the effective rates are not significantly affected by either of them, and their values are practically equal to the nominal ones. The effective conditions here remain metal-limited as predicted by the nominal rates. Since the nominal rates for Ga and In are kept constant throughout the series, the InN mole fraction remains almost unchanged for this region, at ~0.54 as eq. (3.4) predicts for the given arrival rates.

The argument that samples in this region are grown under N-rich conditions is further supported by RHEED observations. The top image of figure 3.2b shows an indicative RHEED pattern for section I. It is characterized by high brightness, which suggests no metal accumulation on the growth surface, and is comprised of spots, which point to growth of 3D structures. This is in agreement with existing observations that nitrogen excess conditions encourage 3D growth as well as the relaxation of the epilayer by the introduction of dislocations [24].

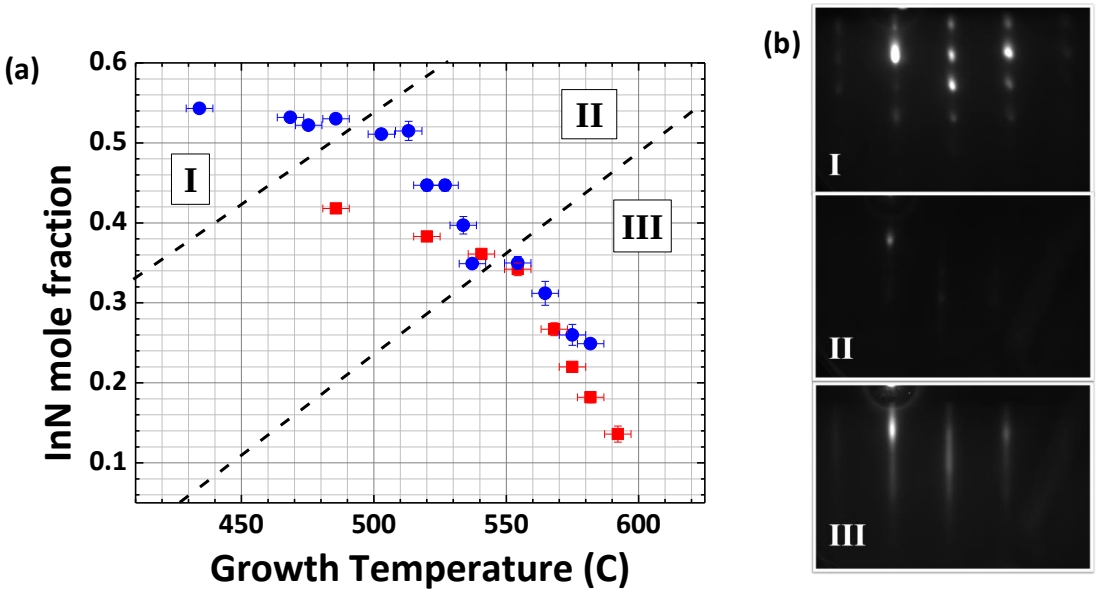

Figure 3.2: (a) InN mole fraction as a function of substrate temperature. Red squares and blue circles are used to plot S1 and S2 samples respectively. Dashed lines are used to divide the plot into sections. (b) characteristic RHEED images for samples grown in sections I (top), II (middle), and III (bottom).

For samples growh inside **section (II)** the effective conditions can be argued to be metal-rich for both of the series. Within this temperature range, indium desortpion is still quite low, and the effective indium rate is not significantly altered. However, it seems that decomposition here starts to have a considerable effect. The effective nitrogen rate is reduced to a low enough point, so that conditions switch to metal-rich even for samples of S2 series, which have a nominal nitrogen excess of 30 nm. Furthermore, decomposition rate appears to increase rapidly with substrate temperature, thus quickly decreasing the InN mole fraction (eq. (3.5)). The fact that InN mole fraction decreases at a faster rate for S2 point to the argument that the decomposition rate is higher for S2 than for S1. As it will be discusse in later chapters, this could be due to the higher indium content of S2 samples, or the difference in nominal rates. Indium that is not incorporated accumulates on the sample surface. This results in RHEED patterns being very dark for this section, as it is apparent from figure 3.2b, middle image. All the samples in this region exhibited indium droplets upon removal from the growth chamber. No indium droplets were observed for samples outside of section (II).

In **section (III)**, the substrate temperatures have increased considerably. InN mole fraction continues to decrease, but a a different rate than that of section (II). The two series seem to almost converge in this region, as far as the In content is concerned. For such high temperatures, not only is decomposition's role very important, but also indium desorption can no longer be overlooked. Effective indium rates are reduced considerably as a result, and the reduction becomes more prominent the higher the temperature. It becomes, therefore, more complicated to make assumptions about the growth conditions. However, the fact that InN mole fraction for S1, and S2 is very similar is an indication that it is no longer strongly affected by the effective nitrogen rate. Furthermore, as shown in the last image of figure 3.2b, RHEED patterns here are bright, which means no accumulated metal on the sample surface. No indium droplets are present on the surface in this region either. Additionally, the RHEED patterns for these samples remain streaky for the duration of the experiment. This suggests a smooth sample surface, and layer-by-layer growth, an argument that is further supported by AFM results, as we will review in the following chapters. All of the above point to effective stoichiometric conditions for this region.

The exact way in which the kinetic processes affect the growth conditions is a complicated subject, which we will try to elucidate with the present work. Further results supporting the above arguments will be presented as this chapter progresses, and we will return to this discussion in following chapters, as the growth mechanisms are investigated in greater detail.

3.4 Structural properties

3.4.1 Phase separation and strain relaxation

Figures 3.3a and 3.3b present a selection of HR-XRD symmetric ω-2θ scans for the (0002) reflections of InGaN films with increasing growth temperatures for series S1 and S2 respectively. Let us look at series S1, which, according to discussion in section 3.3, does not include effectively N-rich samples. For low substrate temperatures, the InGaN diffraction peaks are single, sharp and narrow, which suggests a homogenous composition in the alloy. As we move to higher temperatures, the peaks become shorter, broader and more a-symmetrical. The InGaN peaks begin to show shoulders to their left which gradually increase in intensity as the temperature rises. For yet higher substrate

temperatures (T_{gr} >560° C) double peaks begin to appear in the XRD spectra, possibly suggestive of phase separation. Series S2 exhibits a very similar behavior, only we have to call attention to the fact that the lower temperature samples were grown under different growth conditions.

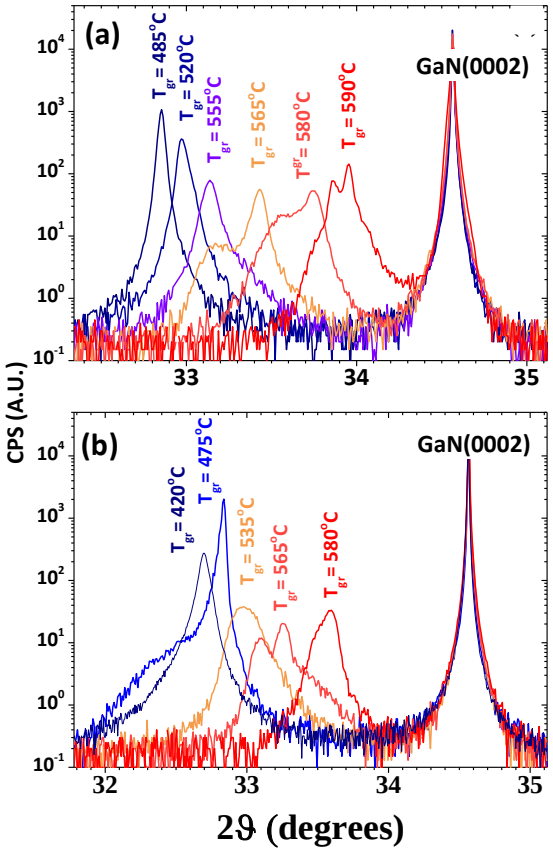

Figure 3.3: Representative examples of HR-XRD *ω-2ϑ* scans around the (0002) Bragg point for InGaN films grown at different substrate temperatures for series S1(a), and S2(b).

The fact that there are secondary peaks some of them in the XRD spectra could be interpreted as the manifestation of a secondary InGaN phase with indium content slightly higher than the main phase, which would be represented by the main peak. However, this conclusion is not definite. Another possible explanation for the shoulders could be variations in film strain, instead of film composition[25]. Previous studies[26-28] have sometimes linked the double peaks to a self-formed pseudomorphic InGaN interlayer between the substrate and the epilayer, called the *sequestration layer*. The composition of the sequestrated layer is usually very close to that of the main film, it has very low density in structural defects, and its thickness ranges a few nanometers. Its presence accommodates the plastic relaxation of strain, therefore, it becomes crucial that we look into the strain relaxation mechanisms of the films.

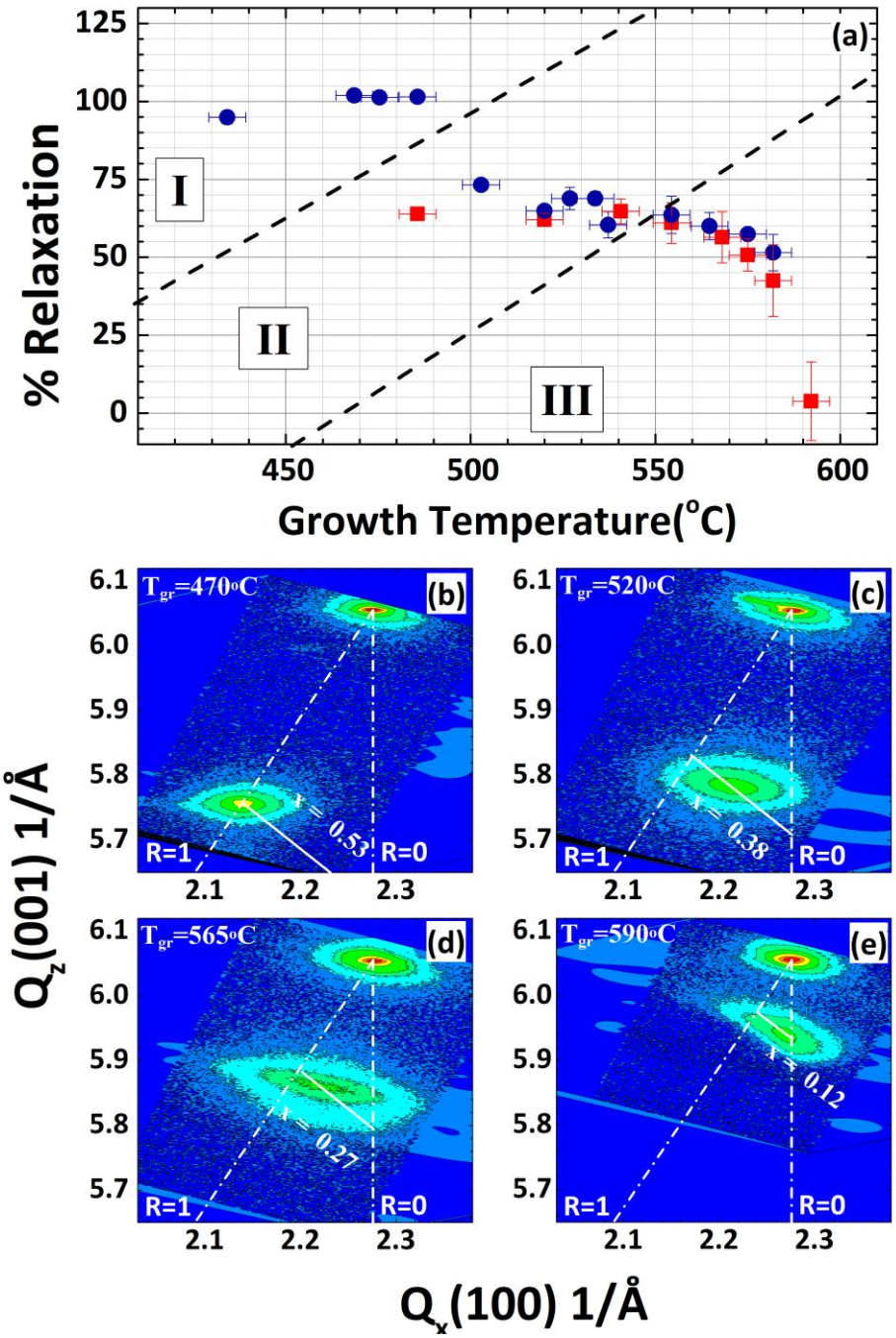

Figure 3.4: (a) Percent of plastic relaxation R of InGaN epilayes as a function of substrate temperature. Red squares and blue circles correspond to S1 and S2 samples. (b), (c), (d), and (e) show characteristic examples of RSMs around the $(10\bar{1}5)$ reflection for samples grown at substrate temperatures of 470C, 520°C, 565°C, and 590°C respectively. In each figure, the dashed lines labelled R=0 and R=1 mark expected peak positions of fully strained and fully relaxed epilayers respectively. The lines connecting the fully strained to the fully relaxed dashed lines indicate the calculated relaxation directions in the reciprocal space for the specific InN mole fraction of the InGaN film in each case.[29]

In figure 3.4a the relaxation of the samples, measured by XRD, is presented as a function of substrate temperature, for series S1 (marked by red squares), and S2 (marked by blue circles). It is

considered helpful to divide the diagram into sections (I), (II), and (III), according to the discussion in section 3.3. For section (I), we observe relaxation close to 100% for samples of S2 series. This is in agreement with growth under effective N-rich conditions, which, as we have mentioned, encourages 3D growth mode, and plastic relaxation of the epilayer. For section (II), the relaxation drops from 100% to approximately 60%. For this section, the conditions have switched to metal-rich, and the growth no longer happens in 3D mode. The metal adlayer present helps to accommodate a 2D growth mode, which could act obstructively to plastic relaxation. For samples in section (III), a further decrease in relaxation is observed, which could be related to the fact that the InN mole fraction is also considerably lower in this region. The lattice parameters of the epilayer are, therefore, closer in values to those of the substrate.

It has been mentioned that the critical thickness of InGaN on GaN substrates is theoretically predicted to be very low, in the order of a few nanometers[30, 31]. This appears to not be supported by these results. The films discussed here have thicknesses that, in most cases, exceed 300nm, although exact thickness depends on temperature. Even for films as thick as that, the relaxation of the epilayer is only partial, when the effective conditions are not metal-limited. This agrees with experimental results from other studies[32, 33] that also report partial relaxation for films thicker than only a few nanometers.

To review the possible correlation between the secondary peaks in the XRD spectra and the films' fluctuations in composition and strain relaxation, an extensive study was performed, with reciprocal space maps around the (105) Bragg reflection, some representative examples of which are presented in figures 3.4b,c,d, and e for different growth temperatures. The dashed lines indicate the fully strained (R=0) and the fully relaxed (R=100) states for the epilayers. The solid lines between the fully strained and fully relaxed states represent the relaxation directions for the respective InN mole fractions, noted in each RSM figure. It is clear that, as the temperature rises, the InGaN (105) diffraction peaks move closer to the R=0 line, meaning an increase in strain, and also closer to the GaN(105) peak, indicating a decrease in indium content. For low temperatures, and fully relaxed samples, the broadening of the InGaN peak does not appear to be happening along the relaxation direction. However, as the relaxation decreases, the broadening seems to be changing direction to match the one of the relaxation for the specific InN mole fraction. This could be interpreted as a gradual strain relaxation process. However, there are many components that could give rise to broadening of the reciprocal space peaks[34, 35], and it is often very difficult to distinguish between them. Furhermore, the XRD intensity for the asymmetric diffraction is not adequate to discern secondary peaks that could be associated with a separate InGaN phase. For these reasons, a TEM study was performed to help clarify these results.

Weak beam dark field (WBDF) images obtained near the $[11\bar{2}0]$ zon axis of a few characteristic samples from series S2 are shown in figure 3.5. The images were recorded using the *g0002* (images on the left) and $g[1\bar{1}00]$ (images on the right) reflections. A sample from section (II) is presented in figures 3.5a, and b. The sample exhibits typical relaxation behaviour, even though they posess high *a*-type threading dislocation densities (see fig. 3.5b), possibly due to a twist type mosaicity introduced at the initial stages of growth. As the growth temperature increases, a change is observed in the relaxation mode. A sequestration layer appears at the GaN/InGaN interface. The sequestrated InGaN (s-layer) is indeed more strained than the main InGaN epilayer, although the strain relaxation seems to happen gradually. The s-InGaN composition is, furthermore, very close to that of the main film. The thickness of the sequestration layer is approximately 30-40nm, and it is accompanied by the introduction of basal stacking faults (BSF) in the main epilayer. Fig. 3.5c, and

3.5d present a sample from series S1, grown at 565° C, that demonstrates the details discussed above. For yet higher substrate temperature, an increase in the thickness of the sequestrated layer is observed, along with an overall decrease in defect content of the InGaN epilayer (see fig. 3.5e, and 3.5f for a sample from series S1 grown at temperature 580° C). This is in agreement with observations from the XRD results: if we attribute the shoulders in the spectra to the sequestration layer, it follows that shoulder intensity becomes greater for higher temperature samples as the sequestration thickness also increases. Some final observations include the fact that for low temperature S2 samples grown under effective N-rich conditions, TEM studies confirm the full relaxation of the samples by a 3D growth mode. Furthermore, for samples with double peaks in the XRD spectra, TEM revealed In-rich regions, often associated with formation of V-pit defects, that support the claim for phase separation. A detailed report of the TEM study has been published in [36].

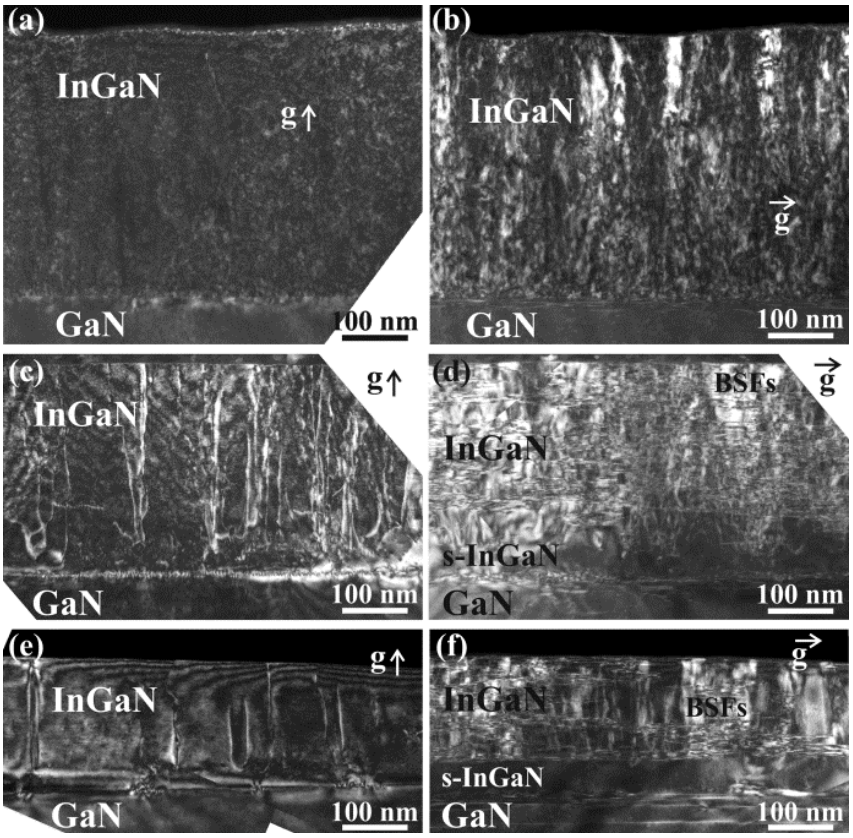

Figure 3.5: Cross sectional WBDF TEM images near the $[11\bar{2}0]$ zone axis of InGaN thin films using $g0002$ [(a), (c), (e)] and $g1\bar{1}00$ [(b), (d), (f)]. (a) and (b) illustrate a sample grown at T_{gr} = 485 °C, (c) and (d) a sample grown at T_{gr} = 565 °C, and (e) and (f) a sample grown at T_{gr} = 580 °C [note that the whole film thickness is not visible in (e) and (f) due to the ion thinning of the TEM foil].

3.4.2 Other structural characteristics

The full width at half maximum (FWHM) of the XRD rocking curves around the (0002) reflection as a function of substrate temperature is shown in figure 3.6. Taking the FWHM as a measure for the structural quality of the film, it is obvious that low temperatures seem to favour crystal quality, as

samples at low T_{gr} have the lowest FHWM values. This is true for both S1 and S2 samples, which potentially means, effective conditions do not play as an important role as for other features. Best results are obtained, around approximately 475° C. After that point, and up to temperatures ~ 520° C, the FWHM shows an increasing trend. For yet higher temperatures, the FWHM seems to be again reducing in value. However, the reader is reminded, that for this temperature range, XRD spectra often demonstrate double peaks.

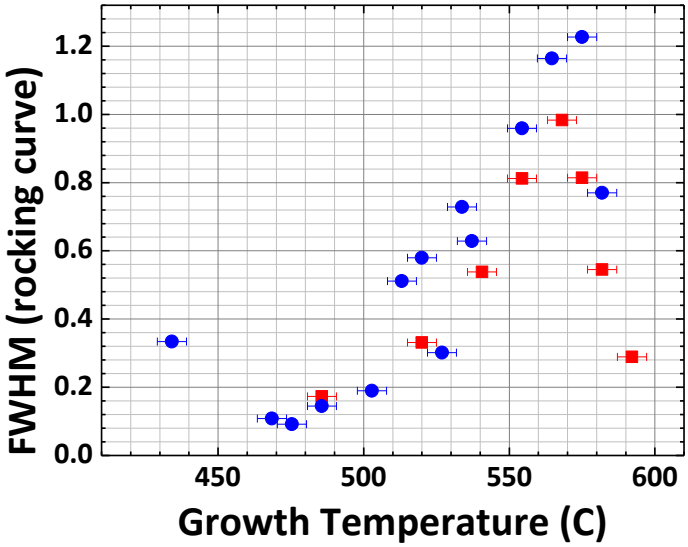

Figure 3.6: XRD rocking curves FHWM of the InGaN peak as a function of the growth temperature. Red squares, and blue circles are used for S1, and S2 samples respectively.

The variation of the XRD depends strongly on the number of defects in the film, and it is found that there is a direct correlation between XRD rocking curve FWHM and threading dislocation densities[36]. The rocking curve around the (0002) is sensitive only to *c*-component threading dislocations[34], and densities for these series were measured by TEM to range from low to high 10^{10} cm^3. However, the majority of threading dislocations is found to be of *a*-type (see figure 3.5), with densities three times the value of those for *c*-type. Such threading dislocations are associated to the strain relaxation since they are connected to misfit dislocation segments lying on the basal plane.

Also from the TEM investigation, it was found that the thickness of the samples decreases with T_{gr}, with nominal thicknesses reached for low temperature samples. For temperatures > 570° C, thicknesses decrease dramatically, due to the pronounced role of the InGaN decomposition and In desorption, as discussed in section 3.3.

Surface roughness was studied with AFM, and the results are presented in figure 3. Fig. 3.7a presents the root mean square (RMS) roughness as a function of the growth temperature, with examples of 10x10nm^2 images for a selection of T_{gr} below. For low temperatures, samples of S2, with growth under N-rich conditions, have a significantly increased RMS roughness compared to the rest of the samples. This, again, concurs with the fact that N-rich conditions give rise to growth of 3D structures, which in turn leads to rough surfaces. In fig. 3.7b, the AFM image of such a sample is presented. The surfaces in this region exhibit 'pits'. This picture changes for higher temperatures:

sections (II), and (III) both include samples with RMS roughness lower than 10nm, and examples of this are presented in fig. 3.7c, and 3.7d respectively. Here, the layer-by-layer growth mode accommodated by slightly metal-rich conditions, results in much smoother surfaces. Best results are obtained for T_{gr}≈550^{o} C. This, however, is possibly more related with the fact that the conditions are closer to stoichiometry at that point, than with temperature effects.

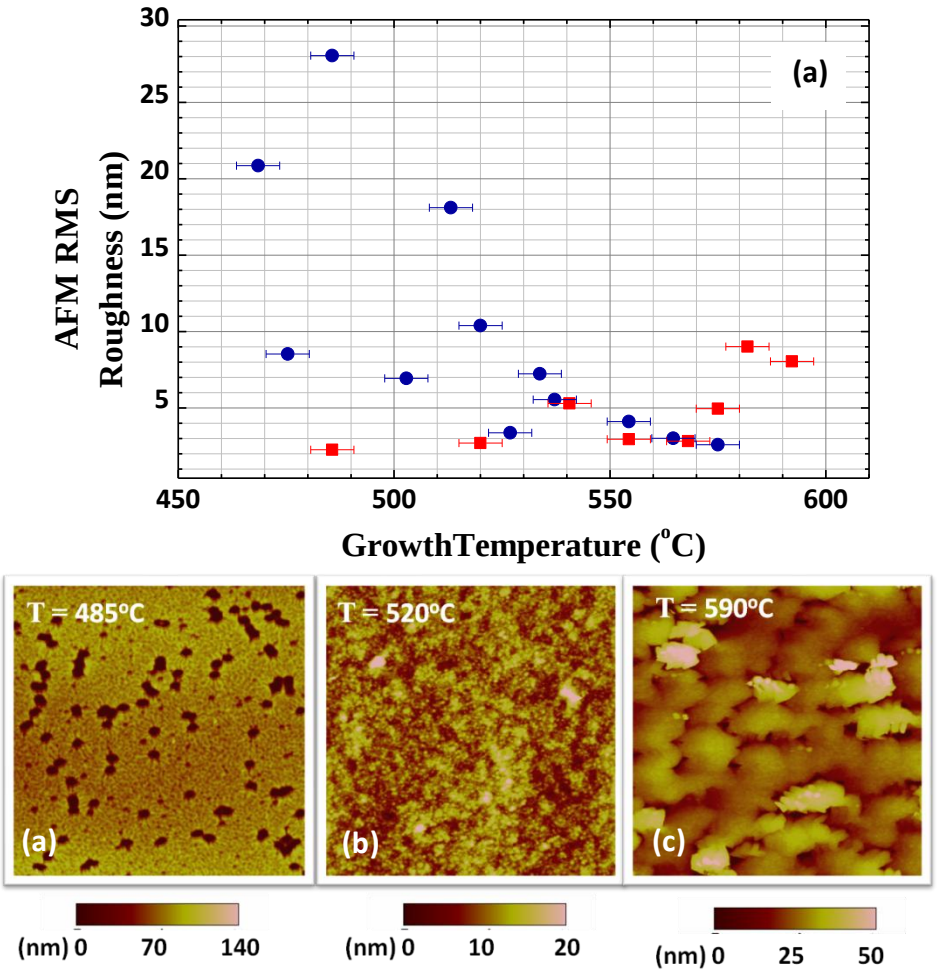

Figure 3.7: (a) AFM RMS roughness as a function of growth temperature; red squares and blue dots correspond to series S1 and S2 respectively. (b), (c) and (d) show 10nmx10nm AFM images for samples grown at substrate temperatures 485^{o}C, 520^{o}C, and 590^{o}C respectively.

3.5 Optoelectronic properties

3.5.1 Hall mobitilites and scattering mechanisms

To investigate the electrical properties of the films, Hall effect measurements were carried out at room temperature for samples in S1, and S2 (see chapter 2 for specifications). Figure 3.8a, 3.8b, and 3.8c show the results as a function of growth temperature, for electrical resistivity, mobility, and carrier density respectively. It is noted here, that contribution from the underlying GaN layer was found not to be significant, and has not been taken into account. Resistivity appears to be a very

strong function of substrate Tempterature, with values increasing as the temperature rises for both series. Carrier mobility also appears to be strongly dependent on T_{gr}, with values decreasing significantly for higher temperatures. However, for lower temperatures, very high mobilities are measured, of the order of ~100 cm^2/V. Such values, for InGaN compositions in the range of 40% to 50%, are higher than what has been previously reported in the literature [37, 38]. Carrier density does not seem to be significantly changing with temperature, with values ranging in the order of ~10^{18} cm^3, and only slightly dropping as the temperature increases.

Transport properties for alloy systems can be complex to investigate. Effects of impurity concentration, acoustic phonon, and optical phonon, and dislocation density are considered for the endpoints GaN, and InN, and have been investigated in literature [39-41], but for the alloy system, one must also consider the effect of alloy disorder scattering [42], which naturally becomes more pronounced for In contents close to the middle of the compositional range, and limits carrier mobility significantly. To clarify the mobility's dependence on temperature and to investigate the different scattering mechanisms, samples' mobilities are plotted as a function of InN mole fraction, in figure 3.9. Along with the experimental data, theoretical calculations [43, 44] of carrier mobilities limited by different mechanisms, namely by optical phonon, Coulomb, and alloy disorder scattering are shown. The calculations assume a carrier concentration of about $10^{18}cm^3$ [43], as is the case for these series. Out of these three mechanisms, alloy scattering is found to have the strongest restrictive effect. However, its effect is limited compared to the experimental values, and its reliance on InN mole fraction does not follow the same trend. Other mechanisms (Coulomb scattering and optical phonon scattering) have an even smaller effect on the carrier mobilities.

In figures 3.10a, and 3.10 b the carrier mobilities are plotted against the electron densities, with the size of each of the plotted points being proportional to the XRD rocking curve FWHM around the (0002), and (105) reflections respectively. Information on the substrate temperature of each sample is also included in the figures. It is obvious that the higher values for mobilites correspond to lower FHWM values. As we have discussed previously, it is found that higher FHWM values correspond to increased threading dislocation densities. Therefore, we could attribute dislocation scattering to be the mechanism dominating the electron mobility values.

Theoretical predictions for the mobilities limited by dislocation scattering [44, 45] were calculated assuming different values for dislocation densities. The results are presented in figures 3.11a, and 3.11b as a function of InN mole fraction, along with the experimental data. The measurements seem to follow the trend predicted by dislocation scattering. The dislocation densities according to this analysis should be of the order of $10^{11}cm^{-2}$. It is reminded that TEM found the threading dislocation densities to be ~10^{10} cm^{-2} but this does not take into account other types of dislocations that could also introduce carrier scattering.

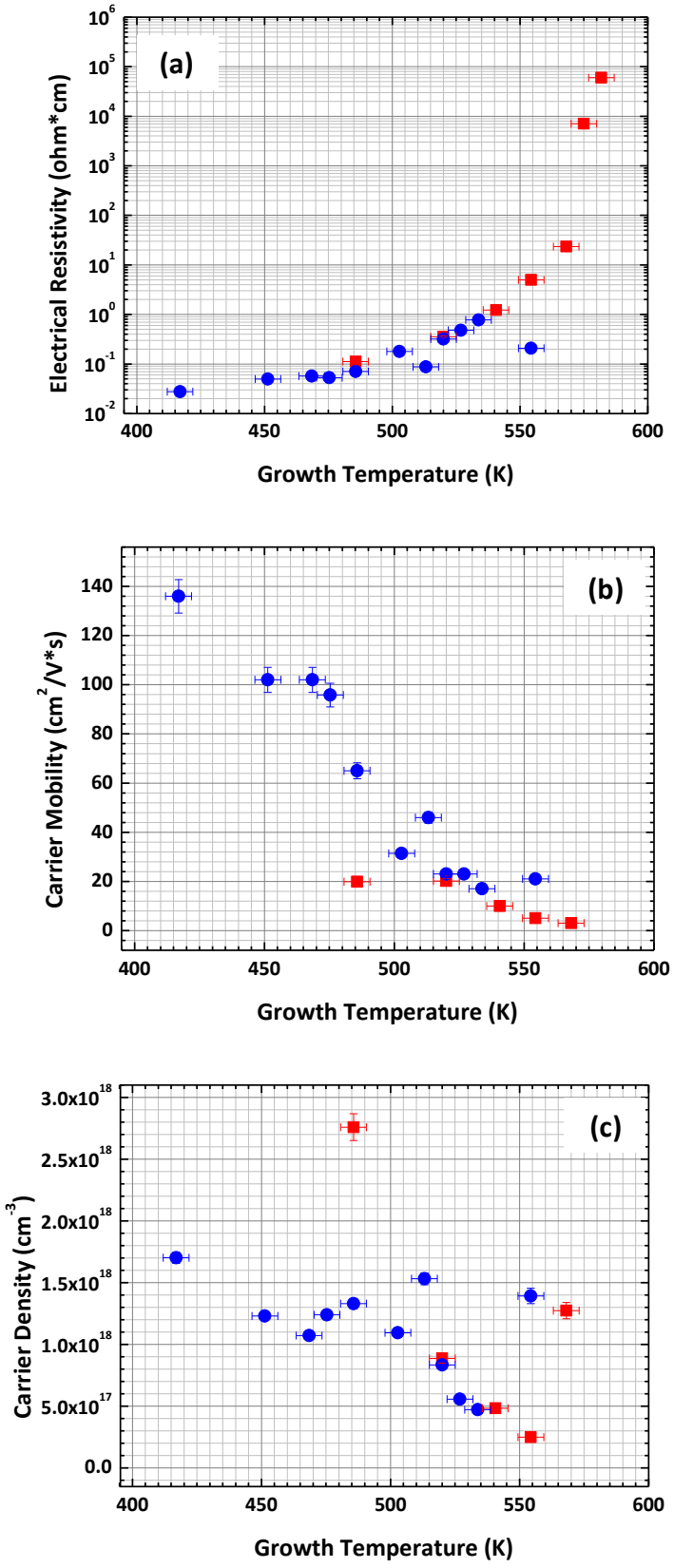

Figure 3.8: Hall resistivity (a), carrier mobility (b) and carrier density (c) as a function of growth temperature Red squares and blue dots correspond to series S1 and S2 respectively

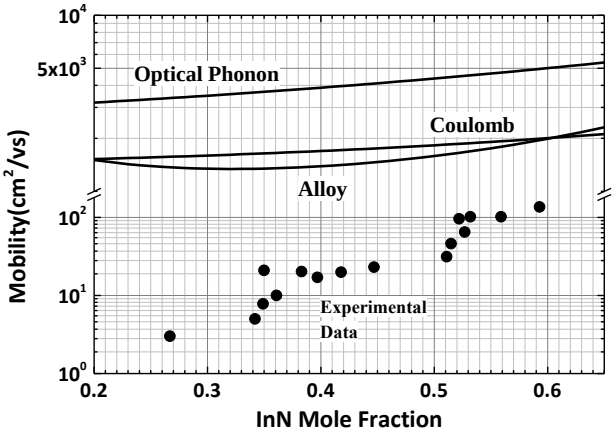

Figure 3.9: Hall mobility of all S1 and S2 samples as a function of InN mole fraction. Theoretical predictions of mobility for scattering mechanisms, namely alloy, optical phonon, and Coulomb scattering (calculated for n=1×1018 cm-3) are also shown.[43]

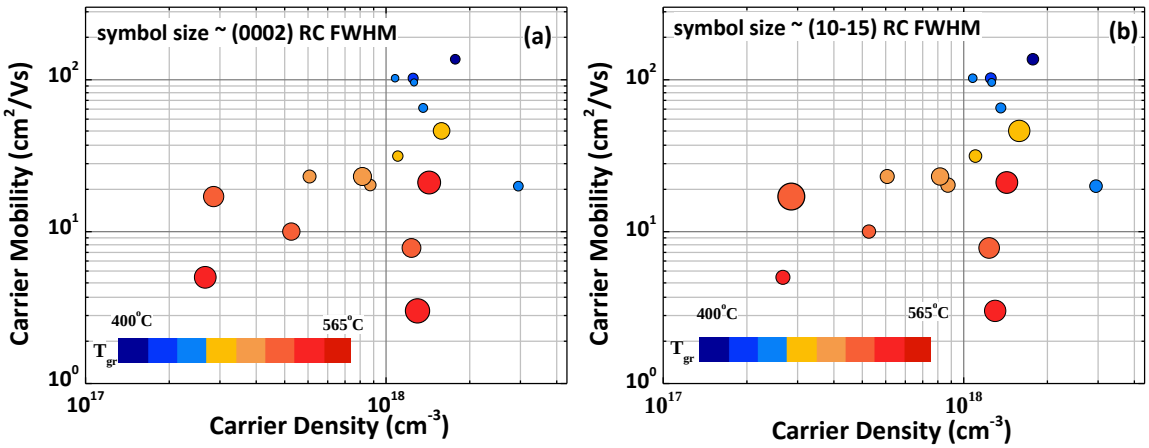

Figure 3.10: Carrier mobility as a function of carrier density, and correlation with the (0002) and (1015)XRD rocking curves' FWHM. Symbols are coloured according to each samples growth temperature (blue for low temperatures, and red for high temperatures). Symbol sizes in (a) and (b) are proportional to the RC FWHM of (0002) and (1015) reflections, respectively.

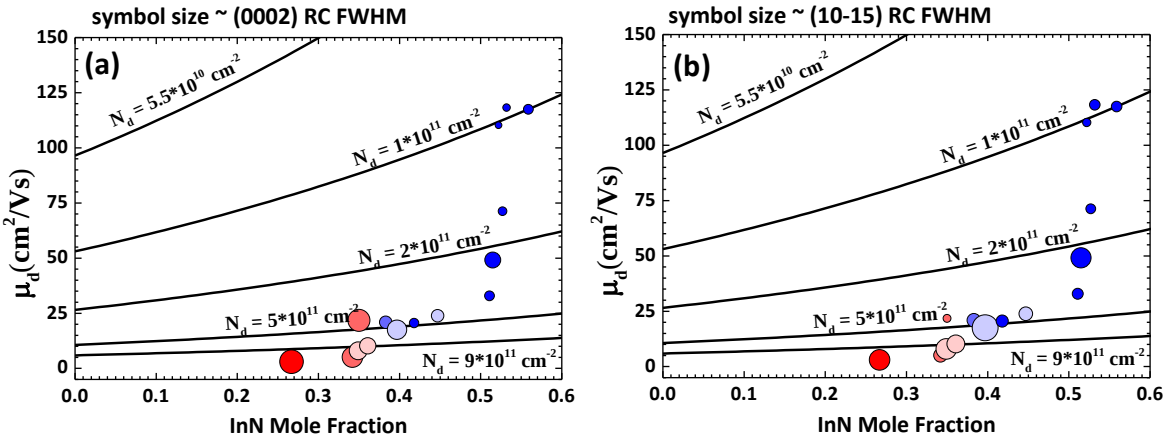

Figure 3.11: Carrier mobilities as a function of the InN mole fraction. Symbols are coloured according to each samples growth temperature (blue for low temperatures, and red for high temperatures). Symbol sizes in (a) and (b) are proportional to the RC FWHM of (0002) and (1015) reflections, respectively. Theoretical calculation for the mobility are also presented, for different values of dislocation densities.[45]

3.5.2 Photoluminescence measurements.

All samples exhibited strong photoluminescence emission at low temperatures. Some characteristic examples of the photoluminescence spectra are presented in Fig. 3.12a. As it can be seen, a large range of emission energies is covered. The modulation in the spectra is attributed to interference from the GaN substrate. PL intensity at room temperature was also significant for most of the samples. Especially strong emission was observed for samples at low temperatures grown at N-rich conditions. The photoluminescence FWHM at low temperature is of the order of 100-200meV for most of the sample range, and it is found to have a week dependence on substrate temperature. For samples with T_{gr} above 475° C the FWHM slightly decreases with temperature. However, samples at low temperatures (again, grown under effective N-rich conditions) display FHWM lower than 100meV. The PL peak positions are found to be quite close to the band gap, and in figure 3.12b they are plotted against InN mole fraction, with only strain effect taken into account for correction.

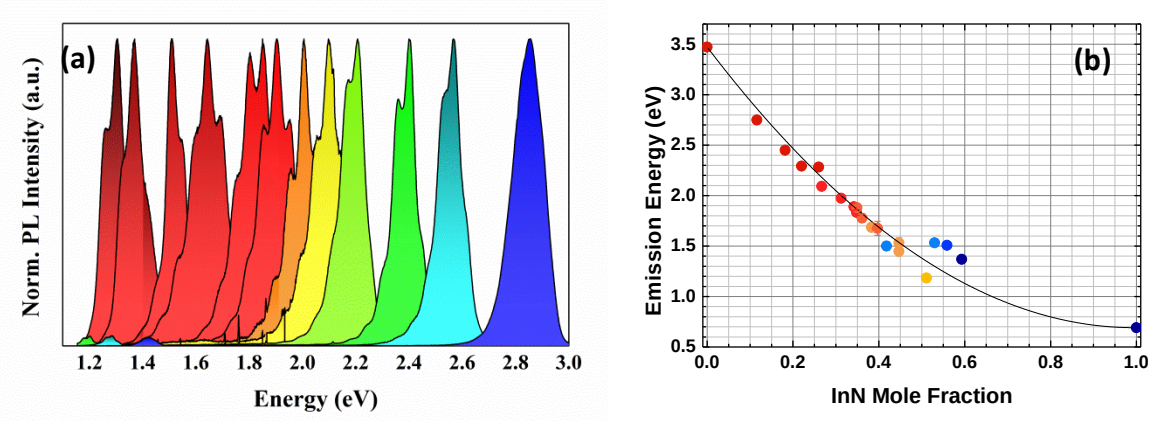

Figure 3.12: (a) Characteristic examples of normalized PL spectra for samples discussed in the present chapter. (b) PL peak position as a function of the InN mole fraction.

REFERENCES

1. Herman, M.A. and H. Sitter, *Molecular Beam Epitaxy Fundamentals and Current Status*. 2013, Berlin: Springer Berlin.
2. Van Hove, J.M. and P.I. Cohen, *Reflection high energy electron diffraction measurement of surface diffusion during the growth of gallium arsenide by MBE.* Journal of Crystal Growth, 1987. **81**(1): p. 13-18.
3. Rosini, M., et al., *Indium surface diffusion on InAs $(2\ifmmode\times\else\texttimes\fi{}4)$ reconstructed wetting layers on GaAs(001).* Physical Review B, 2009. **79**(7): p. 075302.
4. Mula, G., et al., *Surfactant effect of gallium during molecular-beam epitaxy of GaN on AlN (0001).* Physical Review B, 2001. **64**(19): p. 195406.
5. Gallinat, C.S., et al., *A growth diagram for plasma-assisted molecular beam epitaxy of In-face InN.* Journal of Applied Physics, 2007. **102**(6): p. 064907.
6. Adelmann, C., et al., *Dynamically stable gallium surface coverages during plasma-assisted molecular-beam epitaxy of (0001) GaN.* Journal of Applied Physics, 2002. **91**(12): p. 9638-9645.
7. Fernández-Garrido, S., et al., *In situ GaN decomposition analysis by quadrupole mass spectrometry and reflection high-energy electron diffraction.* Journal of Applied Physics, 2008. **104**(3): p. 033541.
8. Averbeck, R. and H. Riechert, *Quantitative Model for the MBE-Growth of Ternary Nitrides.* physica status solidi (a), 1999. **176**(1): p. 301-305.
9. Arrhenius, S., *Über die Reaktionsgeschwindigkeit bei der Inversion von Rohrzucker durch Säuren*, in *Zeitschrift für Physikalische Chemie*. 1889. p. 226.
10. Karpov, S.Y. and Y.N. Makarov, *A Quantitative Model of Surface Segregation in III-V Ternary Compounds.* MRS Proceedings, 2011. **618**.
11. Karpov, S.Y. and Y.N. Makarov, *Indium segregation kinetics in InGaAs ternary compounds.* Thin Solid Films, 2000. **380**(1): p. 71-74.
12. Moseley, M., et al., *Observation and control of the surface kinetics of InGaN for the elimination of phase separation.* Journal of Applied Physics, 2012. **112**(1): p. 014909.
13. Papadomanolaki, E., et al., *Molecular beam epitaxy of thick InGaN(0001) films: Effects of substrate temperature on structural and electronic properties.* Journal of Crystal Growth, 2016. **437**: p. 20-25.
14. Ho, I.h. and G.B. Stringfellow, *Solid phase immiscibility in GaInN.* Applied Physics Letters, 1996. **69**(18): p. 2701-2703.
15. El-Masry, N.A., et al., *Phase separation in InGaN grown by metalorganic chemical vapor deposition.* Applied Physics Letters, 1998. **72**(1): p. 40-42.
16. Doppalapudi, D., et al., *Phase separation and ordering in InGaN alloys grown by molecular beam epitaxy.* Journal of Applied Physics, 1998. **84**(3): p. 1389-1395.
17. Yamaguchi, T., et al., *Growth of thick InGaN films with entire alloy composition using droplet elimination by radical-beam irradiation.* Journal of Crystal Growth, 2013. **377**: p. 123-126.
18. Iliopoulos, E., et al., *InGaN(0001) alloys grown in the entire composition range by plasma assisted molecular beam epitaxy.* physica status solidi (a), 2006. **203**(1): p. 102-105.
19. Adelmann, C., et al., *Gallium adsorption on (0001) GaN surfaces.* Physical Review B, 2003. **67**(16).
20. Koblmüller, G., C.S. Gallinat, and J.S. Speck, *Surface kinetics and thermal instability of N-face InN grown by plasma-assisted molecular beam epitaxy.* Journal of Applied Physics, 2007. **101**(8): p. 083516.
21. Gačević, Ž., et al., *A comprehensive diagram to grow (0001)InGaN alloys by molecular beam epitaxy.* Journal of Crystal Growth, 2013. **364**: p. 123-127.

22. Adelmann, C., et al., *Indium incorporation during the growth of InGaN by molecular-beam epitaxy studied by reflection high-energy electron diffraction intensity oscillations.* Applied Physics Letters, 1999. **75**(22): p. 3518-3520.
23. Storm, D.F., *Incorporation kinetics of indium and gallium in indium gallium nitride: A phenomenological model.* Journal of Applied Physics, 2001. **89**(4): p. 2452-2457.
24. Morkoç, H. and I. Wiley. *Handbook of nitride semiconductors and devices*. 2008; Available from: http://onlinelibrary.wiley.com/book/10.1002/9783527628438.
25. Pereira, S., et al., *Interpretation of double x-ray diffraction peaks from InGaN layers.* Applied Physics Letters, 2001. **79**(10): p. 1432-1434.
26. Liliental-Weber, Z., et al., *Structural perfection of InGaN layers and its relation to photoluminescence.* physica status solidi (c), 2009. **6**(12): p. 2626-2631.
27. Liliental-Weber, Z., et al., *Relaxation of InGaN thin layers observed by X-ray and transmission electron microscopy studies.* Journal of Electronic Materials, 2001. **30**(4): p. 439-444.
28. Ramaiah, K.S., et al., *Characterization of GaN and In x Ga1−xN films grown by MOCVD and MBE on free-standing GaN templates and quantum well structures.* Journal of Materials Science: Materials in Electronics, 2003. **14**(4): p. 233-245.
29. Pereira, S., et al., *Strain and composition distributions in wurtzite InGaN/GaN layers extracted from x-ray reciprocal space mapping.* Applied Physics Letters, 2002. **80**(21): p. 3913-3915.
30. Holec, D., et al., *Critical thickness calculations for InGaN/GaN.* Journal of Crystal Growth, 2007. **303**(1): p. 314-317.
31. Pereira, S., et al., *Structural and optical properties of InGaN/GaN layers close to the critical layer thickness.* Applied Physics Letters, 2002. **81**(7): p. 1207-1209.
32. Parker, C.A., et al., *Determination of the critical layer thickness in the InGaN/GaN heterostructures.* Applied Physics Letters, 1999. **75**(18): p. 2776-2778.
33. Valdueza-Felip, S., et al., *High In-content InGaN layers synthesized by plasma-assisted molecular-beam epitaxy: Growth conditions, strain relaxation, and In incorporation kinetics.* Journal of Applied Physics, 2014. **116**(23): p. 233504.
34. Vickers, M.E., et al., *In-plane imperfections in GaN studied by x-ray diffraction.* Journal of Physics D: Applied Physics, 2005. **38**(10A): p. A99-A104.
35. Moram, M.A. and M.E. Vickers, *X-ray diffraction of III-nitrides.* Reports on Progress in Physics, 2009. **72**(3): p. 036502.
36. Bazioti, C., et al., *Defects, strain relaxation, and compositional grading in high indium content InGaN epilayers grown by molecular beam epitaxy.* Journal of Applied Physics, 2015. **118**(15): p. 155301.
37. Pantha, B.N., et al., *Single phase InxGa1−xN (0.25≤x≤0.63) alloys synthesized by metal organic chemical vapor deposition.* Applied Physics Letters, 2008. **93**(18): p. 182107.
38. Gunes, M., et al., *A comparative study of electrical and optical properties of InN and In0.48Ga0.52N.* Microelectronics Journal, 2009. **40**(4): p. 872-874.
39. Chin, V.W.L., T.L. Tansley, and T. Osotchan, *Electron mobilities in gallium, indium, and aluminum nitrides.* Journal of Applied Physics, 1994. **75**(11): p. 7365-7372.
40. Miller, N., et al., *Effect of charged dislocation scattering on electrical and electrothermal transport inn-type InN.* Physical Review B, 2011. **84**(7).
41. Abdel-Motaleb, I.M. and R.Y. Korotkov, *Modeling of electron mobility in GaN materials.* Journal of Applied Physics, 2005. **97**(9): p. 093715.
42. Aydogu, S., M. Akarsu, and O. Ozbas, *InN and In1−XGaX N: calculation of hall mobilities and effects of alloy disorder and dislocation scatterings.* Materials Science in Semiconductor Processing, 2012. **15**(4): p. 347-352.
43. Hsu, L., et al., *Electron mobility in InN and III-N alloys.* Journal of Applied Physics, 2007. **102**(7): p. 073705.

44. Donmez, O., et al., *The role of dislocation-induced scattering in electronic transport in GaxIn1-xN alloys.* Nanoscale Research Letters, 2012. **7**(1): p. 490.
45. Ng, H.M., et al., *The role of dislocation scattering in n-type GaN films.* Applied Physics Letters, 1998. **73**(6): p. 821-823.

CHAPTER 4: InGaN Decomposition

4.1 Introduction

In the previous chapter, we mentioned that the thermal decomposition of InGaN plays a central role in the MBE growth of InGaN by altering the effective growth conditions and thus limiting the indium incorporation in the alloy. For that reason, it becomes essential to understand and describe the process in as much detail and precision as possible

This is not a straightforward problem. In-N bonds are much weaker than Ga-N bonds[1] and, at the temperatures typically used for InGaN growth, the decomposition rate for InN is several orders of magnitude larger than that for GaN[2, 3]. As a result, InGaN decomposition's dependence on temperature is very complicated and still not very well understood. Even for the alloy components GaN, and InN seperately, the decomposition rates are still not very well defined. An Arrhenius [4] dependence on temperature is often assumed, but the activation energies found in literature can range from 3.1 eV to 3.9 eV for GaN[2, 5-8], and anywhere from 1.12eV to 1.92eV[9-11], and even 4.4eV[12] for InN.

It follows the above discussion that not only is the decomposition rate for $In_xGa_{1-x}N$ a function of temperature, but also depends on the composition x of the alloy. What is more, to control growth conditions in an effective way, one needs to qualitatively describe the decomposition rate. InGaN. Several models have been proposed in the literature, but there is not one that has been widely accepted. A few of them are discussed here.

The simplest model used to describe the decomposition rate, according to Gacevic et al.[10], is a linear function of x:

$$F_{InGaN}^{Dec} = xCe^{-E_a^{InN}/kT} \qquad (4.1)$$

where *k* is the Boltzmann constant, *T* the temperature, *C* a constant, and E_a^{InN} the activation energy for the decomposition of InN. A slightly more sophisticated case is considered by Averbeck et al.[8], which assumes the activation energy to also be a function of *x*:

$$F_{InGaN}^{Dec} = xCe^{-E_a(x)/kT} \qquad (4.2)$$

Lastly, Turski et al[13], goes a step further and considers the decomposition rate to depend on arrival rates as well as temperature. The activation energy, in this case is assumed to vary linearly with InN mole fraction between the activation energies of GaN and InN:

$$F_{InGaN}^{Dec} = \left(\frac{C_1}{F_N} + \frac{C_2}{F_{Ga}}\right) \cdot (F_N - F_{Ga})e^{-\frac{E_a(x)}{kT}} \qquad (4.3)$$

with

$$E_a(x) = xE_a^{InN} + (1-x)E_a^{GaN} \qquad (4.4)$$

To assess the decomposition models proposed in the literature, let us at first consider the preliminary series S3 and S4 discussed in chapter 3.2. These series consist of samples grown at

T_{gr}=520° C, so we can eliminate the temperature factor, and look into dependence on film composition. Selecting the samples grown at effective **metal-rich** conditions, and according to equation (3.3), we can extract the decomposition rate as follows:

$$F_{InGaN}^{Dec} = \Delta F_N = F_N - F_N' = F_N - F_{GR} \qquad (4.5)$$

where F_{GR} the growth rate. Growth rates are calculated using xSEM measurements of the samples' thicknesses, and the results as a function of InN mole fraction are presented in figure 4.1 along with predicted values for the models discussed above.

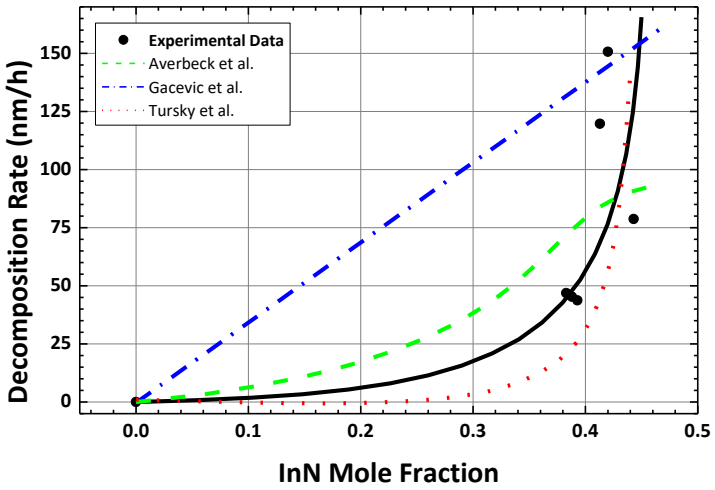

Figure 4.1: Decomposition rate as a function of InGaN mole fraction. Experimental data are represented by black circles. The green, blue, and red lines correspond to the models found in [8],[10], and [13] respectively.

It is clear from figure 4.1 that, while some of the models seem to be describing the decomposition rate better than others, there is still a long way before we can predict the rates in an efficient and accurate way. In this chapter, a thorough study of the thermal decomposition of InGaN during MBE growth is presented. A qualitative model is proposed to predict the decomposition rate at given growth conditions. What is more, we look into how thermal decomposition affects the indium incorporation, and the quality of the InGaN films. The optimum conditions for InGaN films are investigated, and how those conditions are related to decomposition and desired indium content.

To investigate InGaN decomposition a large number of samples were grown by MBE, and are discussed here. In total, 8 series of samples were grown, and the parameters for each one are presented in table IV. A few supplementary samples were also grown, not included in table IV. Arrival rates are given in GaN eq. values, as usual. For each of the series, growth temperature and nominal nitrogen rate F_N were kept unchanged. Within each series, samples were grown with different Ga nominal rates, ranging from very low to almost equal to the N rate. For each sample, the In nominal rate was adjusted according to the RHEED observations, so that effective metal-rich conditions would be maintained. Deposition time was typically 90min, although for some of the samples with very high decomposition rates, longer deposition times were employed to reach adequate thicknesses. All films discussed here were grown on free-standing GaN(0001) wafers. Ex situ, XRD measurements were performed to measure the films' lattice constants, relaxation and InN mole fraction, according to the specifications of chapter 2. Thicknesses were measured by

spectroscopic ellipsometry, and were verified from cross sectional SEM images. Further characterization of the films includes SEM, AFM, and photoluminescence measurements.

SERIES	Growth Temperature (° C)	Nominal N arrival rate (nm/h)	Number of samples
A	485	200	7
B	520	230	7
C	520	300	7
D	535	300	7
E	555	300	3
F	485	160	4
G	555	275	3
H	570	275	4

Table IV: Growth parameters (growth temperature, nitrogen arrival rates), a number of samples for series A-H.

4.2 Model for InGaN thermal decomposition

To calculate the decomposition rate, as mentioned above, each sample's thickness was measured. The thickness, translated into GaN equivalent thickness, was then divided by the deposition time to give the sample's growth rate. The growth rate was then extracted from the nominal arrival rate to yield the value of the decomposition rate.

However, to make sure that this method gives an accurate measure of the decomposition rate, we need to confirm that the growth conditions for each sample this analysis takes into consideration were effectively metal-rich, meaning effective nitrogen flux was lower than the total effective metal flux. Effective rates, as it was discussed in the previous chapter, could be very different from nominal rates, especially since decomposition can be very high for these particular experiments. In fact, for most of the samples discussed here, the nominal nitrogen rate was higher than the nominal metal rates. The indium rate was adjusted during growth by observing the RHEED intensity, with the goal of maintaining excess of metal on the sample surface for the duration of the epitaxial process. However, additional steps were taken to make certain this was true. Samples were also checked for indium droplets, and/or accumulated indium upon removal from the growth chamber. Relaxation of the samples, as measured by XRD was also used as an indicator, as N-rich conditions lead to 100% relaxation. Samples which did not satisfy the above criteria were not taken into account.

To demonstrate the extent to which decomposition alters the effective growth conditions, in figure 4.2, a RHEED image is shown for a sample grown with nominal rates of 23 nm/h, 52nm/h, and 300nm/h GaN eq rates for Ga, In and N respectively. The nominal rate for nitrogen is higher than the total metal rates by more than 200nm/h. Yet, the decomposition is so great, that the RHEED is completely dark, due to indium accumulated on the sample surface. Upon removal from the chamber, a thin layer of indium was observed on the InGaN surface.

Figure 4.2: RHEED image for a sample grown with nominal rates of 23 nm/h, 52nm/h, and 300nm/h GaN eq rates for Ga, In and N respectively. RHEED appears to be completely dark, due to excessive indium accumulation.

The results for most of the series studied here are presented in figure 4.3. Figure 4.3a shows the decomposition rates as a function of resulting InN mole fraction. As we can see, there is no clearly discernible trend, and data seem to be irregularly scattered. However, if, instead of InN mole fraction, we consider the parameter

$$x' = 1 - \frac{F_{Ga}}{F_N} \quad (4.6)$$

which is a function of nominal growth conditions, and not effective ones, a much more noticeable pattern arises (fig, 4.3b). This means that, for MBE growth, the decomposition depends less on the InN mole fraction of the resulting alloy, and more on the surface stoichiometry during growth. The concept behind this reasoning can be understood as follows. It has been established that Ga is preferentially incorporated over In. Therefore, at any instant, out of the arriving nitrogen atoms on the growth front, the available nitrogen for In to form bonds with is given by $F_N - F_{Ga}$. This, of course, assumes that the decomposition rate for GaN is very low, and Ga-N bonds are not destroyed once they are formed. This is a logical assumption for the temperatures discussed here, as we have mentioned. For effectively indium-rich conditions (which is always the case here), enough indium is present on the growth surface for the available nitrogen to form bond with, but a lot of them are destroyed right at the surface, and are never incorporated into the bulk crystal. From these In-N bonds that are destroyed, the N atoms are lost, while In atoms accumulate on the surface, provided the In desorption happens at a lower rate than the decomposition rate. The decomposition rate can be, in many cases, higher than the incorporation rate, which explains why a large excess of nitrogen in nominal values still yields metal-rich conditions, and leads to indium accumulation on the sample surface. The ratio, then of In-N bonds to total Nitrogen atoms is dynamically given by (4.6). Indium atoms that are incorporated into the bulk crystal are presumably more difficult to result in decomposition. The incorporated indium can then be written as

$$F_{In}^{*} = F_N - F_{Ga} - F_{InGaN}^{Dec} \quad (4.7)$$

and the indium mole fraction can then be found by:

$$x = \frac{F_{In}^{*}}{F_N - F_{InGaN}^{Dec}} = 1 - \frac{F_{Ga}}{F_N'} \quad (4.8)$$

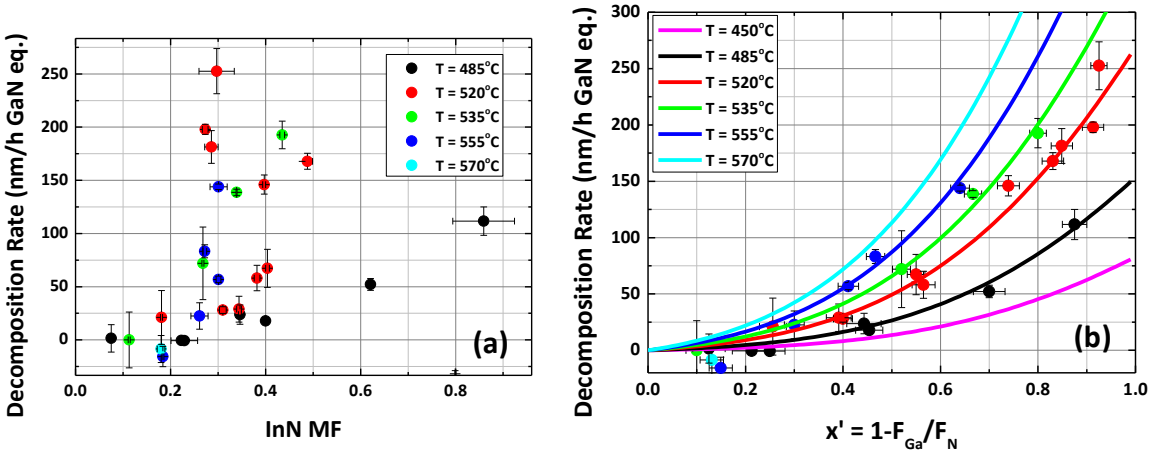

Figure 4.3: Decomposition rate as a function of (a) InN mole fraction, and (b) parameter x'. Different temperatures are represented by different colors, according to the figures legends.

According to figure 4.3b, the decomposition rate seems to increase with x' in an exponential manner, which means very high decomposition rates for lower Ga fluxes. Additionally, as expected, there is a strong dependence on temperature, which should be described by one, or more activation energies.

For a qualitative description of the InGaN decomposition as a function of the parameter *x'*, two models were considered and fitted. The first approach (model A) considers a linear dependence of the activation energy, similar to Turski et al[13]. The activation energy varies between two values, E_1 for *x'*=1, and E_2 for *x'*=0. However, the varying parameter is not InN mole fraction, but *x'*. Additionally, the model also considers a linear dependence on *x'* for the prefactor, as is given by eq. (4.9)

$$F_{InGaN}^{Dec} = [C_1 x' + C_2(1-x')]\exp\{-[\mathrm{E}_1 \mathrm{x}' + \mathrm{E}_2(1-\mathrm{x}')]/\mathrm{kT}\} \quad (4.9)$$

Model A was fitted to the experimental data to give four fitting parameters. A second, simpler model B was also considered, in an attempt to minimize the number of fitting parameters. According to model B, the decomposition rate is given by:

$$F_{InGaN}^{Dec} = \frac{2x' C_1 \exp\left(-\frac{E_1}{kT}\right)}{1-\exp\left[-\frac{E_2(x'-1)}{kT}\right]} \quad (4.10)$$

The two models, along with the fitting parameters for each of them are summarized in table V. Figure 4.4 presents a comparison of the models.

A model	B model
$F_{InGaN}^{Dec} =$ $[C_1 x' + C_2(1-x')]\exp\{-[\mathrm{E_1 x' + E_2(1-x')}]/\mathrm{kT}\}$	$F_{InGaN}^{Dec} = \frac{2x' C \exp\left(-\frac{E_1}{kT}\right)}{1-\exp\left[-\frac{E_2(x'-1)}{kT}\right]}$
$C_1 = 4.470 \cdot 10^7$ nm/h GaN eq.	$C = 6.714 \cdot 10^7$ nm/h GaN eq.
$C_2 = 2.256 \cdot 10^8$ nm/h GaN eq.	$E_1 = 0.85eV$
$E_1 = 0.82eV$	$E_2 = 0.20eV$
$E_2 = 1.21eV$	

Table V: Summary of the two models, with the respective fitting parameters.

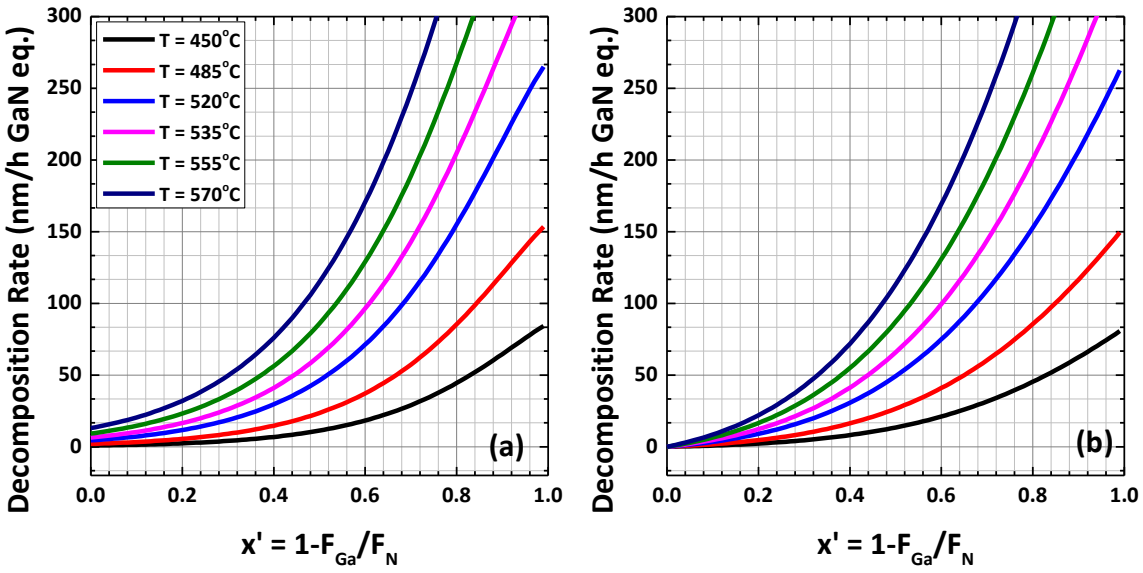

Figure 4.4: Decomposition rates as a function of parameter x' as predicted by (a) model A, and (b) model B.

As we can see, the two models give very similar results for the decomposition rate. The only significant difference is that model B yields ~0 decomposition rate for x'≈0, whereas model A does not. This means model B assumes zero decomposition for GaN at all temperatures. As we mentioned before, this is not an unreasonable assumption for the temperature range discussed for these experiments. For higher temperatures, this, of course, ceases to be true, but outside the temperatures examined here, there is no information to take into account anyway.

4.3 Decomposition and In incorporation

Figure 4.5 presents the InN mole fraction as a function of parameter *x'*, for series A-H, with different colors to represent different growth temperatures. The InN mole fraction as predicted by the decomposition models described in the previous paragraph is also shown. There are no

significant differences in the InN MF as calculated by models A, and B, so from now on, no distinction will be made between the two. According to our study, we can divide the variation of InN MF as a function of *x'* into three sections. To discuss these in detail and clearly, figure 4.6a presents the InN MF for series D only, along with the calculation according to our decomposition model. RHEED images are also presented (fig. 4.6b) for most of the samples of that series.

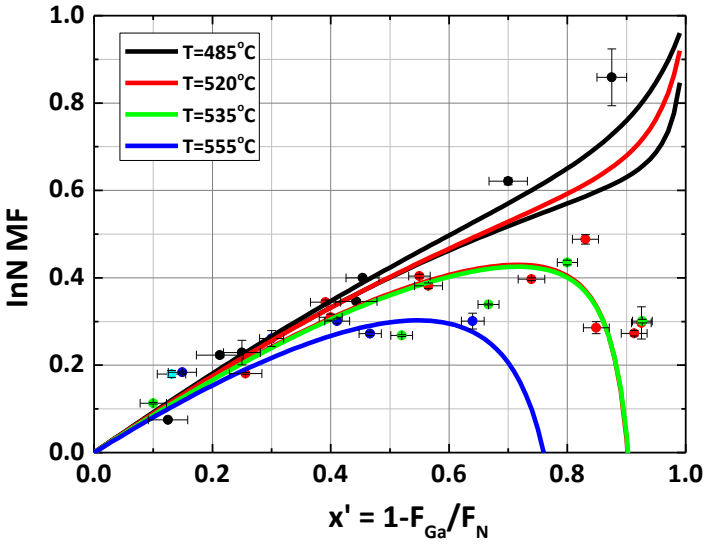

Figure 4.5: InN mole fraction as a function of parameter x', for series A,B,C,D,E,F. Different colors are used to represent different growth temperatures, as indicated by the figure legend. Experimental data are represented by circles, while solid lines represent the InN mole fraction, as predicted by the decomposition model.

Section (I): For relatively high Ga fluxes, the decomposition rate is limited. Then, according to equations (4.6) and (4.8):

$x \approx x'$ (4.11)

and InN MF increases in an almost linear fashion. Since the decomposition is not significant, the growth conditions are easy to regulate. This, as seen in fig. 4.6b, results in streaky RHEED images (x'=0.2).

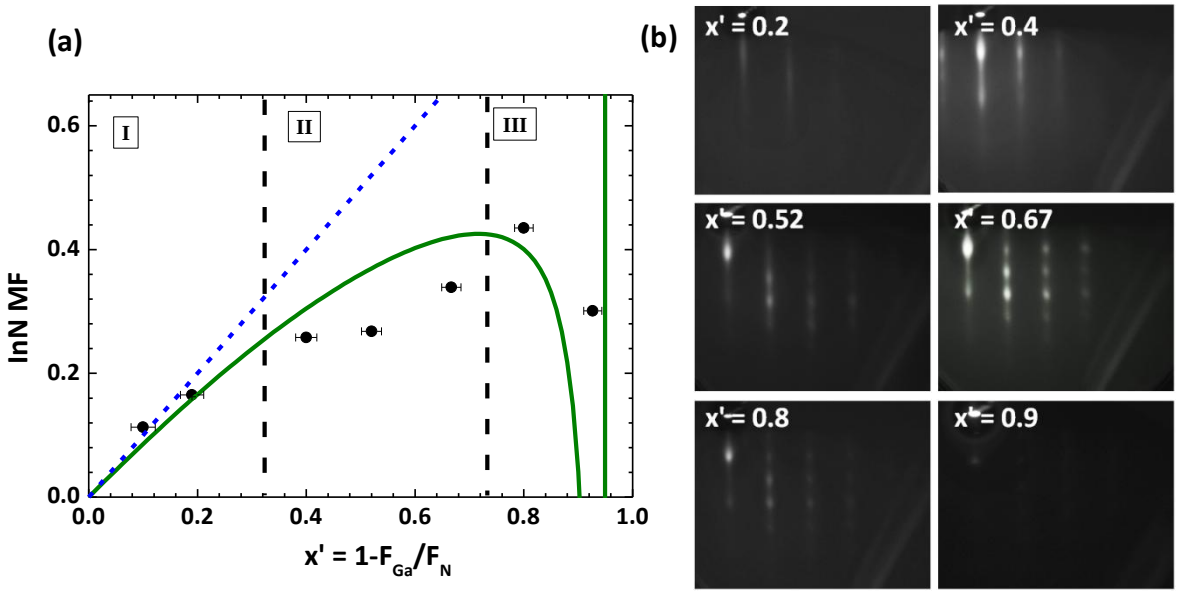

Figure 4.6: (a) InN mole fraction as a function of parameter x' for series D. Circles represent experimental points, and the solid line represents the value predicted by the decomposition model. The dashed blue line indicates InN MF for zero decomposition (x'=x). Sections I, II, and III are also marked. (b) Characteristic RHEED images for samples belonging to series D with values for the respective x' parameters indicated for each image.

Section (II): For intermediate Ga rates, as the decomposition starts to become more and more significant, InN mole fraction starts to deviate from the x=x' line, and eventually reaches a maximum value and saturates for this part of the graph. This section is characterized by RHEED images which get progressively less streaky as the x' parameter increases. The growth conditions are also more difficult to control here, since decomposition leads to indium accumulation.

A temperature-related limit for the incorporation of In in InGaN has often been reported in the literature[9, 10, 14]. Similar incorporation limitations have been reported for other III-N alloys, such InAlN[15]. As the decomposition rate increases for higher x' values, it could account for such limitations.

Section(III): For low Ga rates, the decomposition becomes very high. According to the model, a very rapid drop in InN MF is predicted, and for even lower Ga rates (in figure 4.6, for x'>0.9) the decomposition rate exceeds the N arrival rate, which practically means that no film is deposited. In reality, the InN MF becomes very difficult to predict in this part, because of the great value of the gradient. High decomposition rate leads to excess indium accumulation, which in turn results in very low intensity RHEED images (x'=0.8, and x'=0.9 in figure 4.6b). Some of the samples grown in these conditions exhibited a thin film of indium on their surface, upon removal from the growth chamber. This much accumulation also often results in inhomogeneities in the films' composition, and phase separation. This will also be discussed in following paragraphs, with relation to the structural characterization of the films. The connection between intense decomposition and phase separation is not fully understood. However, it has been found that certain sites are more favorable for indium incorporation than others, and the very rough surfaces resulting from severe decomposition could mean slightly different incorporation probabilities for different types of surface irregularities. What is more, excessive decomposition renders the regulation of the accumulating indium layer

impossible. Indium that accumulates on the sample surface has been shown to arrange into clusters, and these islands are responsible for producing In-rich nanostructures in the film[16, 17].

Figure 4.7 presents a few SEM and AFM images from samples grown in section (III), to give the reader a sense of the extreme conditions under which growth takes place for these samples. Often times the decomposition seems to be so high that the InGaN film appears obliterated in the SEM, and AFM images. Sections of the film appear somtimes to be missing, and what film is left is not uniform in thickness, and extremely rough.

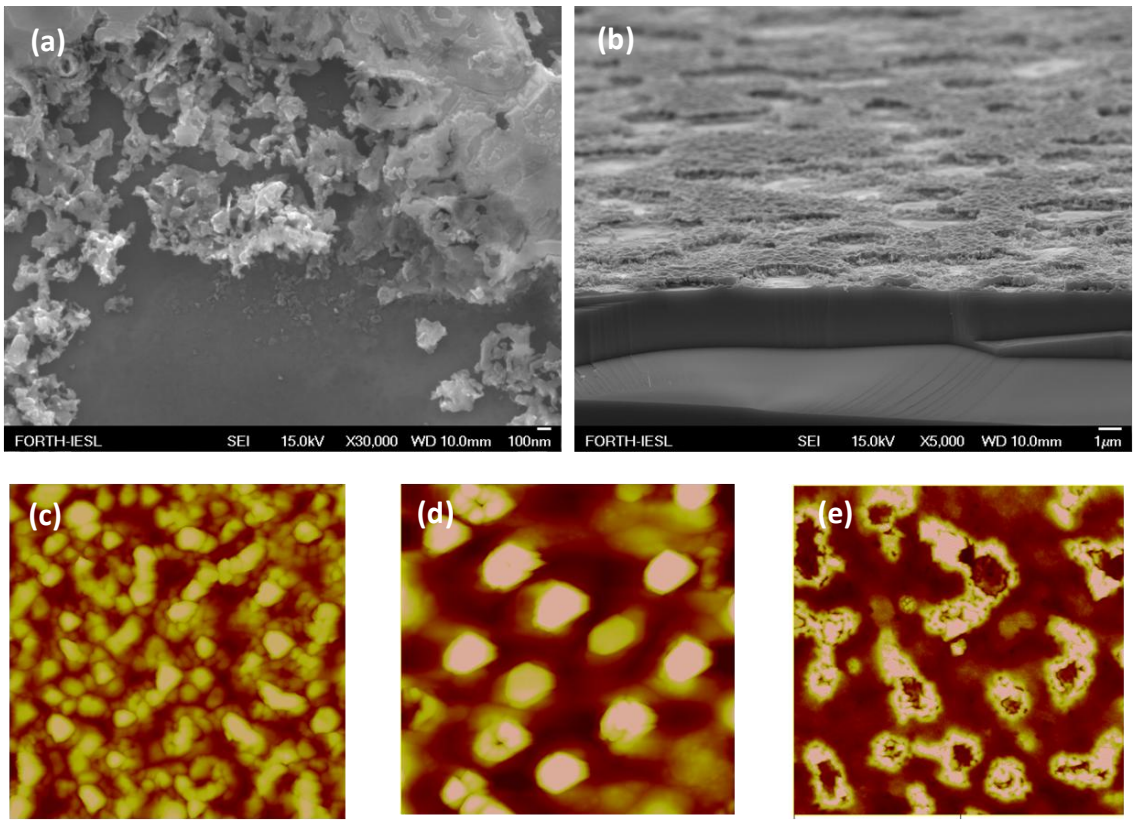

Figure 4.7: Characteristic SEM ((a), and (b)), and AFM ((c), (d), and (e)) images for samples grown under extreme decomposition conditions (section III).

Let us now consider In incorporation as a function of growth temperature, and N arrival rate. Figure 4.8a shows the InN MF calculated according to our model, as a function of the parameter x', at different substrate temperatures for a given N arrival rate of 300nm/h GaN eq. Figure 4.8b also shows the predicted InN MF as a function of x'; this time, the growth temperature has been kept at a fixed value of T_{gr}=520^{o} C, and the arrival rate of nitrogen is changed.

As we can see in figure 4.8a, the incorporation increases as the substrate temperature becomes lower, and the decomposition rate decreases. Between temperatures 535^{o}C and 520^{o}C, there is a change for section (III), and it no longer demonstrates a rapid drop, but rather a steep increase for very low Ga rates. However, the decomposition is still quite intense for this range of Ga rate, and, for such extreme conditions, other factors may influence the incorporation, and it is not straightforward to calculate the InN MF. For decreasing temperatures, we can consider the respective sections (I),

(II), and (III) as moving progressively to the right of the plot. Eventually, for very low temperatures, with no significant decomposition the InN MF approximates the x=x' line.

A similar behavior is observed for figure 4.8b. This time, the incorporation increases as the Nitrogen rate becomes higher, and the decomposition rate is not as important in comparison. However, after a point, to increase In incorporation slightly, a dramatic increase in N rate is demanded. This might not be feasible, since N rates are limited for most MBE systems. The decrease of T_{gr} then becomes the only option for successfully developing high In content InGaN alloys.

Again, these observations seem to agree with results from literature[18], that report that enhanced in incorporation in InGaN films is often observed either by lowering the substrate temperature, or by increasing the growth rates.

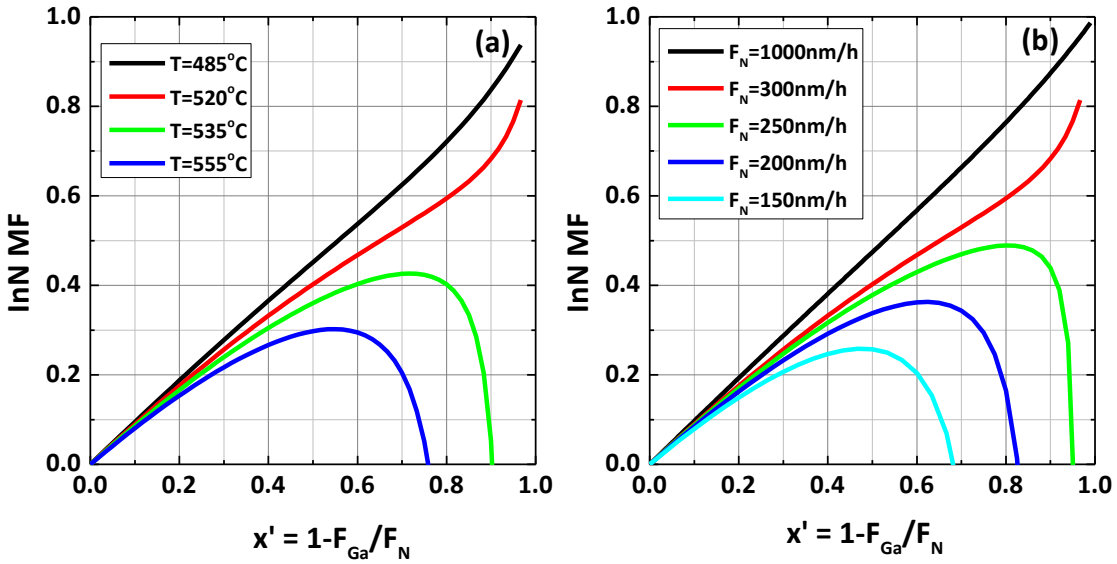

Figure 4.8: InN MF predicted by the decomposition model as a function of the parameter x' In (a) different temperature cases are presents for a given N arrival rate of 300 nm/h GaN eq, while in (b) different nitrogen rates are considered for a given value of substrate temperature of 520°C.

4.4 Decomposition and structural properties

In figure 4.8, characteristic examples o SEM images for series C (fig. 4.8a), along with the plot for the InN MF as a function of x' (figure 4.8b) for quick reference. We can easily recognize from the SEM images the progression of the InGaN decomposition that takes place, until section (III) images (x'=0.73, x'=0.87, and x'=0.96), which exhibit very rough surface morphologies, with 3D structures, and non-uniformities. The best surface morphologies are observed for samples grown with conditions that correspond to x' around the transition from section (I) to section (II) (see fig. 4.8b). Samples with even lower x', often exhibit pits on the surface (fig. 4.8a, x'=0.23).

The surface roughness of the samples was assessed by AFM, and the results, presented in figure 4.9, confirm the above observations. For high Ga rates, all of the sample surfaces have an RMS roughness lower than 10nm, with most values being around 5nm. For lower Ga rates, intense decomposition leads to the dramatic deterioration of the RMS roughness of surfaces.

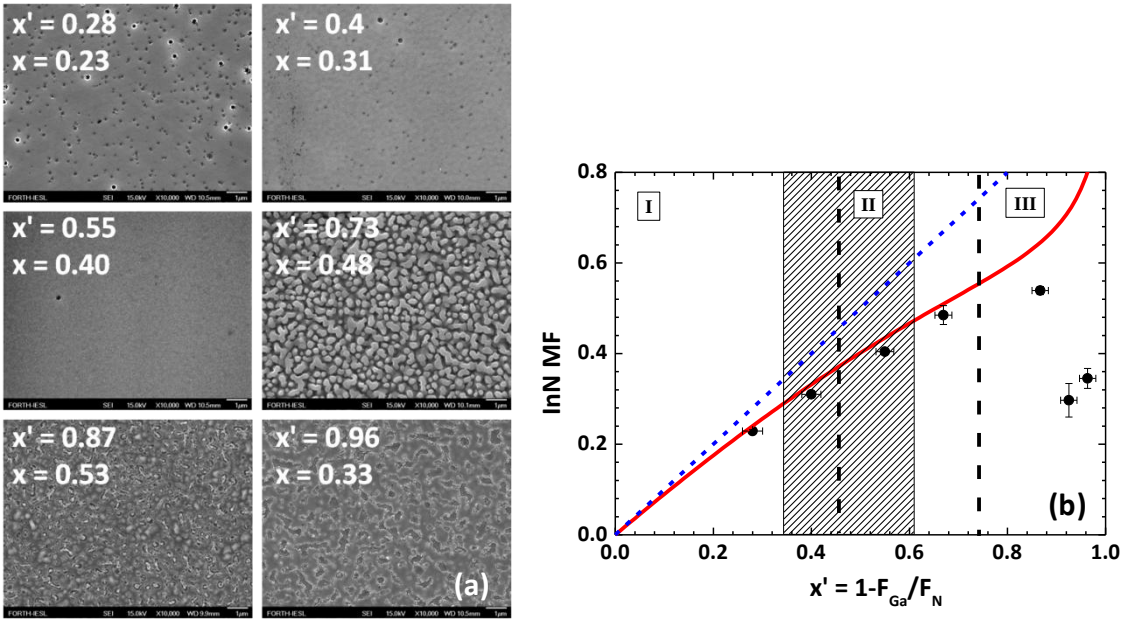

Figure 4.8: (a) Characteristic examples o SEM images for series C. For each image the value of the InN mole fraction and the x' parameter of the respective samples are indicated. (b) InN mole fraction as a function of parameter x' for series C. Circles represent experimental points, and solid line represents the value predicted by the decomposition model. The dashed blue line indicates InN MF for zero decomposition (x'=x). Sections I, II, and III are marked. The shadowed part of the figure indicates the conditions for which best surface morphologies are obtained.

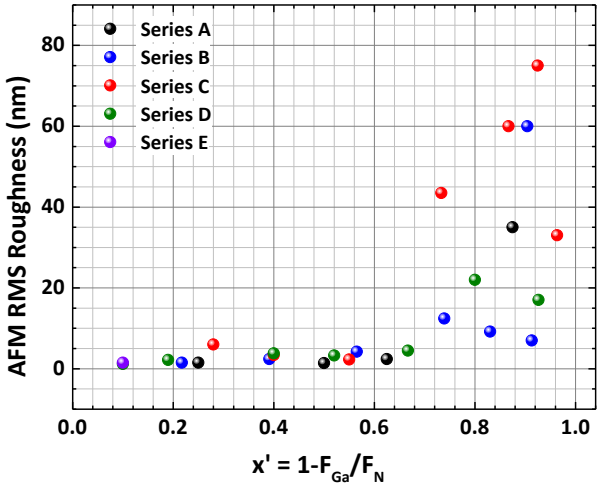

Figure 4.9: AFM surface roughness as a function of parameter x' for series A, B, C, D, and E.

Figure 4.10 presents a selection of HR-XRD symmetric ω-2θ scans for the (0002) reflections of InGaN films for series B (figure 4.10a), again, with the respective plot for the InN MF (figure 4.10b). For high Ga fluxes, samples exhibit single, narrow peaks, which suggests uniform composition in the films. However, this changes for lower Ga fluxes (higher x'). The InGaN peaks then start to become

broader, lower in intensity, and a lot of the time double peaks and phase separation is observed in the films (XRD spectrum with x'=0.89). It would be reasonable to assume, as it was mentioned before, that phase separation and inhomogeneities here are related to very high decomposition rates, and the difficulty to regulate the indium accumulating on the surface in this conditions range. Again, the best results from XRD scans are obtained for x' close in value to the point of transition between sections (I) and (II). Growth with lower x' values results in broader, shorter XRD InGaN peaks (figure 4.11a, x'=0.26).

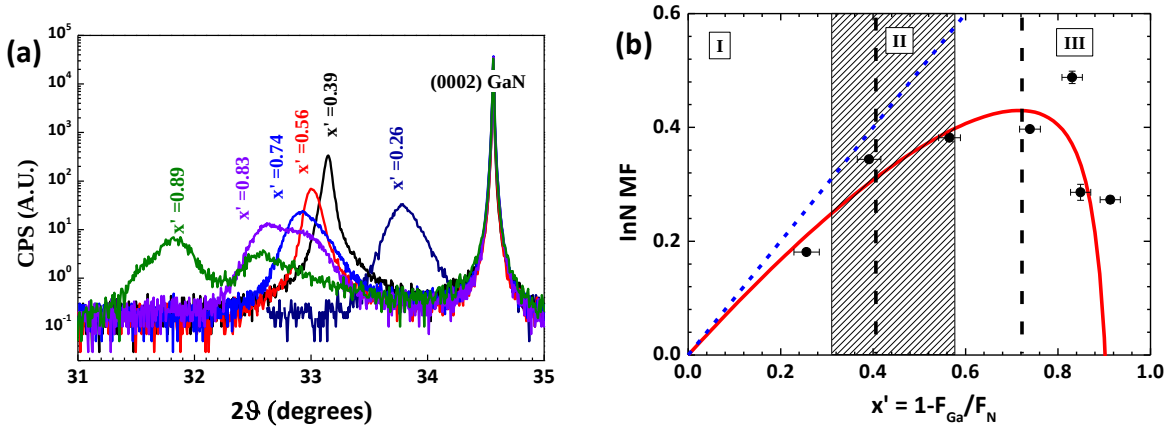

Figure 4.10: (a) Representative examples of HR-XRD *ω-2ϑ* scans around the (0002) Bragg reflection for samples of series B. The value of the x' parameter for each sample is indicated (b) InN mole fraction as a function of parameter x' for series B. Circles represent experimental points, and solid line represents the value predicted by the decomposition model. The dashed blue line indicates InN MF for zero decomposition (x'=x). Sections I, II, and III are marked. The shadowed part of the figure indicates the conditions for which best surface morphologies are obtained

4.5 Decomposition and optical properties

All samples exhibited strong photoluminescence emission at low temperatures. Peak positions cover the entire range of energies from 0.7eV to 3.4eV. The low temperature photoluminescence FHWM seems to have a dependence on x', as it is presented in figure 4.11a. High Ga rates result in low PL FWHM, in the order of 100meV. As the Ga rate decreases, the FWHM increases greatly in value, which agrees with all other characterization of the films. PL peak positions are found to be reasonably close to the energy band gap, and a bowing parameter of 2.77eV is derived directly from the PL centres without any other correction except strain effects (figure 4.11b).

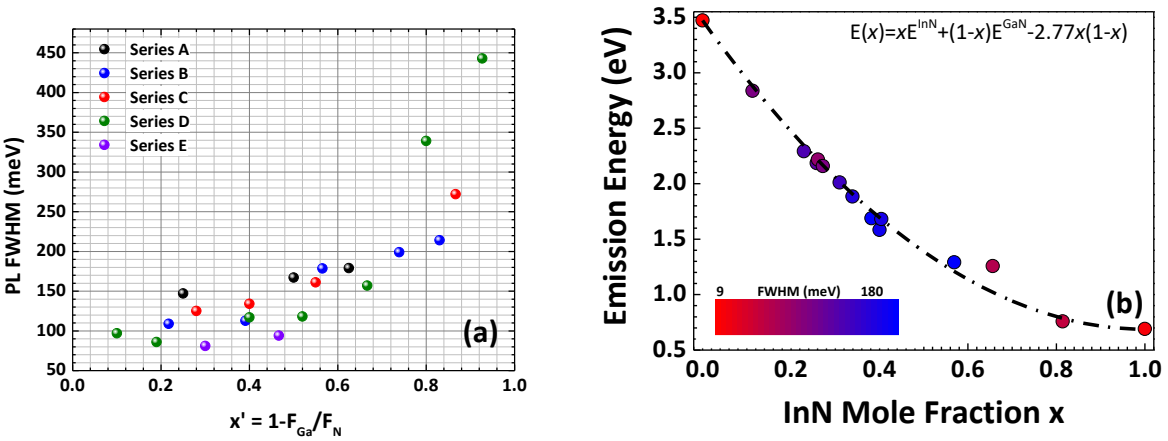

Figure 4.11: (a) LT PL FWHM as a function of parameter x' for series A, B, C, D, and E. (b) Emission energy as a function of InN mole fraction for samples discussed in this chapter. Strain effects have been taken into account.

4.6 Optimum window for growth

According to the full characterization of series A-H that is discussed in this chapter, we conclude that the optimum conditions for InGaN growth with InN mole fraction x, are obtained from the plot of the InN MF versus the parameter x', which depends on the nominal arrival rates. Best results are obtained for films grown in the transition region from sections (I), and (II). This window, for a given growth temperature and N arrival rate, should yield InN MF slightly lower than the maximum possible. For lower Ga rates, decomposition is so great that it affects film properties and inhibits In incorporation. On the other hand, higher Ga rates result in slightly poorer morphological and optical characteristics. For a given N arrival rate, the growth window will progressively move to lower x' values, as the temperature increases. This means that higher In-content InGaN films require the significant reduction of the growth temperature.

Figure 4.12 presents series A-H, and marks the optimum window schematically. The arrow indicates the direction of the window displacement as the temperature increases.

Once the optimum window for growth is defined, uniform samples can be obtained across the compositional range, with excellent structural qualities, without any phase separation. Figure 4.13 presents a range of such films with HR-XRD spectra (4.13a) and PL emission spectra (4.13b).

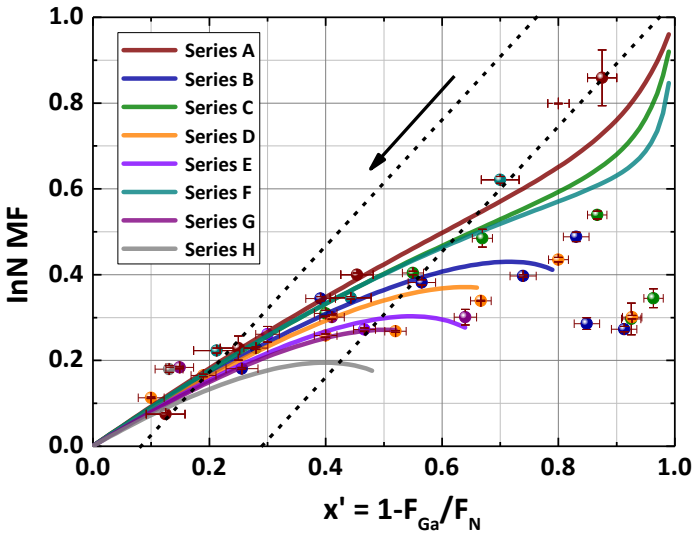

Figure 4.12: InN mole fraction as a function of parameter x' for series A-H. Colors for the respective series are indicated in the figure legend. The section between the dashed lines marks the growth window for optimum film quality. Arrow indicates the direction in which the window shifts as the growth temperature increases.

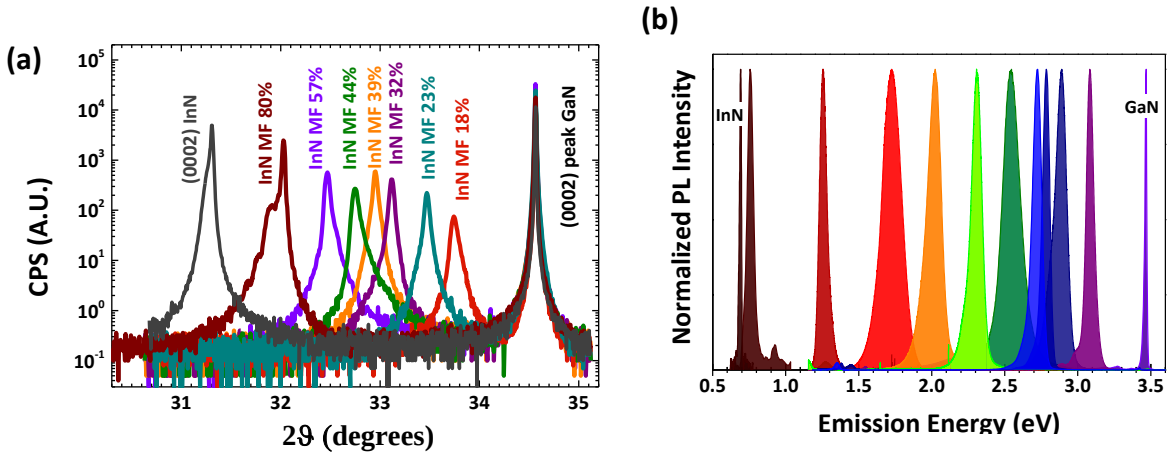

Figure 4.13: Characteristic examples of samples grown within the optimum growth window. (a) HR-XRD *ω-2ϑ* scans around the (0002) Bragg reflection. (b) Low temperature photoluminescence spectra.

REFERENCES

1. Thaler, G.T., et al., *Thermal stability of thin InGaN films on GaN.* Journal of Crystal Growth, 2010. **312**(11): p. 1817-1822.
2. Ambacher, O., et al., *Thermal stability and desorption of Group III nitrides prepared by metal organic chemical vapor deposition.* Journal of Vacuum Science & Technology B: Microelectronics and Nanometer Structures Processing, Measurement, and Phenomena, 1996. **14**(6): p. 3532-3542.
3. Karpiński, J., J. Jun, and S. Porowski, *Equilibrium pressure of N2 over GaN and high pressure solution growth of GaN.* Journal of Crystal Growth, 1984. **66**(1): p. 1-10.
4. Arrhenius, S., *Über die Reaktionsgeschwindigkeit bei der Inversion von Rohrzucker durch Säuren*, in *Zeitschrift für Physikalische Chemie*. 1889. p. 226.
5. Fernández-Garrido, S., et al., *In situ GaN decomposition analysis by quadrupole mass spectrometry and reflection high-energy electron diffraction.* Journal of Applied Physics, 2008. **104**(3): p. 033541.
6. Grandjean, N., et al., *GaN evaporation in molecular-beam epitaxy environment.* Applied Physics Letters, 1999. **74**(13): p. 1854-1856.
7. L'vov, B.V., *Kinetics and mechanism of thermal decomposition of GaN.* Thermochimica Acta, 2000. **360**(1): p. 85-91.
8. Averbeck, R. and H. Riechert, *Quantitative Model for the MBE-Growth of Ternary Nitrides.* physica status solidi (a), 1999. **176**(1): p. 301-305.
9. Nath, D.N., et al., *Growth model for plasma-assisted molecular beam epitaxy of N-polar and Ga-polar InxGa1−xN.* Journal of Vacuum Science & Technology B, Nanotechnology and Microelectronics: Materials, Processing, Measurement, and Phenomena, 2011. **29**(2): p. 021206.
10. Gačević, Ž., et al., *A comprehensive diagram to grow (0001)InGaN alloys by molecular beam epitaxy.* Journal of Crystal Growth, 2013. **364**: p. 123-127.
11. Gallinat, C.S., et al., *A growth diagram for plasma-assisted molecular beam epitaxy of In-face InN.* Journal of Applied Physics, 2007. **102**(6): p. 064907.
12. Koblmüller, G., C.S. Gallinat, and J.S. Speck, *Surface kinetics and thermal instability of N-face InN grown by plasma-assisted molecular beam epitaxy.* Journal of Applied Physics, 2007. **101**(8): p. 083516.
13. Turski, H., et al., *Nonequivalent atomic step edges—Role of gallium and nitrogen atoms in the growth of InGaN layers.* Journal of Crystal Growth, 2013. **367**: p. 115-121.
14. Valdueza-Felip, S., et al., *High In-content InGaN layers synthesized by plasma-assisted molecular-beam epitaxy: Growth conditions, strain relaxation, and In incorporation kinetics.* Journal of Applied Physics, 2014. **116**(23): p. 233504.
15. Fernández-Garrido, S., Ž. Gačević, and E. Calleja, *A comprehensive diagram to grow InAlN alloys by plasma-assisted molecular beam epitaxy.* Applied Physics Letters, 2008. **93**(19): p. 191907.
16. Chen, H., et al., *Surface structures and growth kinetics of InGaN(0001) grown by molecular beam epitaxy.* Journal of Vacuum Science & Technology B: Microelectronics and Nanometer Structures Processing, Measurement, and Phenomena, 2000. **18**(4): p. 2284-2289.
17. Chen, H., et al., *Spontaneous Formation of Indium-Rich Nanostructures on InGaN(0001) Surfaces.* Physical Review Letters, 2000. **85**(9): p. 1902-1905.
18. Moseley, M., et al., *Control of surface adatom kinetics for the growth of high-indium content InGaN throughout the miscibility gap.* Applied Physics Letters, 2010. **97**(19): p. 191902.

CHAPTER 5: Indium desorption

5.1 Introduction

Metal desorption has been already been identified as the main mechanism that limits the effective rates for metals during MBE growth. To be more precise, adsorption and desorption are the mechanisms that determine the amount of metal present at any moment on the epitaxial surface, which is probably the most crucial factor affecting the growth mode, and consequently the film's morphology and properties.

In chapter 1, we mentioned the importance of a Ga bilayer covering the surface during MBE growth of GaN. It has been found that the existence of a Ga adlayer acts as a surfactant[1], and gives N adatoms the required mobility on the surface to accommodate 2D growth, which results in smooth surfaces and inhibits the introduction of stacking faults[2, 3]. Inadequate or no Ga coverage has been found to give rise to Straski-Krastanow mode, and leads to 3D structures and increased dislocations[4]. However, to gain the benefits of the metal adlayer, one needs to understand the mechanics for adsorption and desorption, in order to adjust the growth conditions to effectively regulate the metal coverage.

Adsorption and desorption of gallium on GaN surfaces have been extensively studied and is fairly well understood. It has been shown that Ga is adsorbed on the GaN(0001) surface as a laterally contracted bilayer[5]. According to this, when Ga atoms are adsorbed on the sample surface, they are arranged into two adlayers on top of the Ga-terminated surface, a bottom adlayer, consisting approximately of 1ML Ga[6], and a top adlayer, consisting of 1.3-1.6 MLs of Ga. [5-7]. The result is a a bilayer stucture consisting of 2.3-2.7 MLs of Ga total. After this bilayer structure is complete, additional Ga accumulates on the top adlayer to from Ga droplets[3, 8].For higher growth temperatures, it is possible to stabilize the Ga bilayer structure under certain Ga fluxes, and thus control the growth process.

Desorption of Ga takes place at different rates depending on whether it happens from the bottom layer, the top layer, or the droplet state. Experimental measurements of the Ga desorption have been reported for different substrates. For desorption from the bilayer. activation energies range from 1.24eV[9] to 5.1eV[6] for GaN(0001) surfaces, and 3.5eV[10] for a 6H-SiC(0001) surface, and 2.8eV[4] for AlN(0001). Measurements for desorption from the droplet state seem to yield more consitstent results with activation energies ranging from 2.5eV[10] to 2.8[9], values which are close to the activation energy for Ga evaporation from liquid Ga. Desorption rates are inherently difficult to measure, due to the fact that there is uncertainty in experimentally determining the surface coverage precisely. Additionally, the rate equations that describe the evolution of the metal coverage are quite complicated with many unknown parameters, including the desorption rates, as well as transfer rates between the different metal states.

Indium has been proposed as a surfactant for growth of such materials as GaN[11] and AlGaN[12], so some research has been performed, but the precise mechanics for In adsorption and desorption are yet to be fully understood. For InGaN growth, in particular, which is the focus of this study, it has already been shown that effective growth conditions are a crucial factor that affects quality of the resulting film, the alloy homogeneity, as well as incorporation of In, for high-In, quality InGaN films. It is, therefore crucial to collect more information on Indium adsorption and desorption kinetics on the GaN(0001) surface. For this reason, a thorough study of In adsorption and desorption by means of monitoring RHEED intensity was performed, and is presented in this chapter. Different In states on the GaN(0001) surface were identified, activation energies for In desorption were extracted, and a correlation was found to exist between In desorption rates and the In coverage.

High resistivity GaN(0001)wafers were used to study the adsorption/desorption kinetics of In. The evolution of the RHEED specular beam intensity was monitored and recorded in real time. For the setup specifications, the reader is referred to chapter 2. For each experiment, the sample was kept at a constant temperature, high enough to observe significant rates of desorption. The indium flux was also kept at a constant value, and the sample was exposed to it for a duration of 20s. In between measurements, there was a waiting time sufficient for the surface to fully recover and the intensity to return to its original value. Experiments were performed at a temperature range from 540^{o}C to 605^{o}C, and for varying indium fluxes.

5.2 Evolution of the RHEED intensity transient

In figure 5.1 the variation of the normalized specular RHEED intensity is presented for a set of indium impinging fluxes ranging from 0.35ML/s to 0.75ML/s. at a fixed temperature of 582^{o}C. The shaded part of the plot indicates the time period for which the indium shutter remains open. Upon the opening of the shutter, a rapid decrease of RHEED intensity is observed. After the initial rapid drop, RHEED intensity continues to decrease at a much lower rate until the shutter closes. As soon as the indium flux is interrupted, the intensity begins to recover to its initial value. The recovery rate is at first comparable to the latter part of the shaded portion, and following this, the intensity continues to increase at a much lower rate. Furthermore, there is also a variety of observed peaks and valleys both during deposition and desorption. Such specific features will be discussed in greater detail below.

To discuss the adsorption and desorption process, and correlate it to the transient evolution of the RHEED intensity in more detail, an example of a RHEED response is presented in figure 5.2, with the time scale adjusted to more clearly show features of interest. Like before, the shaded part signifies the time during which the In shutter is open. Some important time intervals are also marked and defined, and will be discussed below.

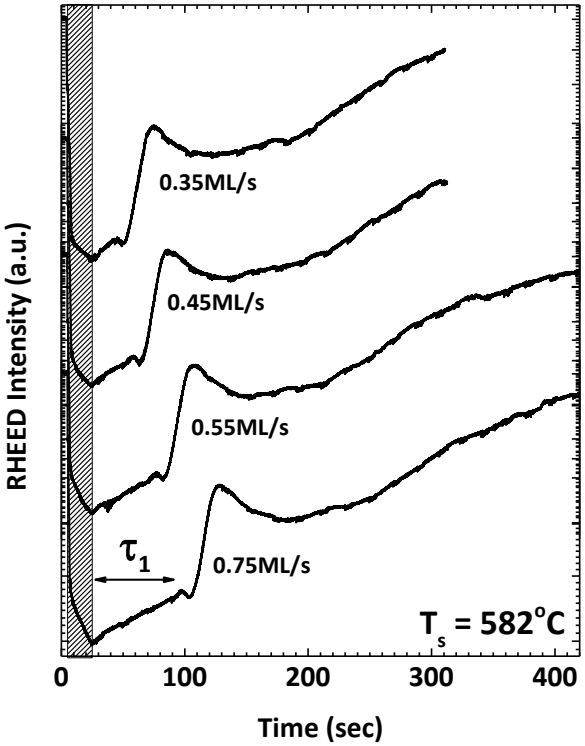

Figure 5.1: Set of transient responses of the normalized RHEED specular intensity for 20s of In adsorption (shaded part) and subsequent desorption as substrate temperature T_s=582°C. The respective In rates for each response are indicated.

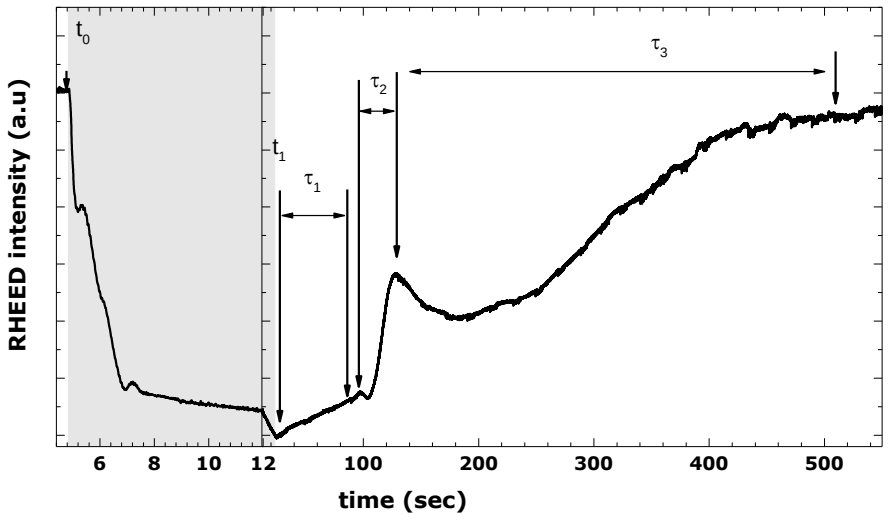

Figure 5.2: A characteristic example of the transient response of the RHEED intensity is shown, with definition of features that are used for this study.

The evolution of the RHEED transient response can be interpreted according to the following scenario. When the shutter opens, at time t_0, indium rate F_{In} starts impinging on the GaN surface. Initially, indium is adsorbed onto the surface in a two-dimensional way. This process corresponds to

the early fast decrease of the RHEED intensity, that seems to follow a nearly exponential decay, caused by the shading of the GaN surface by the metal. For this part, there are some oscillations observed, which presumably correspond to points of constructive interference from layers of indium that have been completed as the adsorption takes place in a two-dimensional, layer-by-layer way. Subsequently, the first rapid drop in intensity is succeeded by a further drop of intensity, which, however, happens at a much slower rate than previously, and follows an almost linear decay. In this part, indium adsorption no longer happens in layers. The slower drop in intensity is rather related to the fact that, after initial wetting of a surface described before, the excess metal that accumulates on the surface arranges into clusters. Decrease in intensity is caused by the accumulation of indium, and the increase of the clusters volume.

Upon interruption of F_{In} at time t_1, desorbing of indium from the surface happens in similar stages. At first, there is a slow increase in intensity, with a rate that is comparable to the latter part of the adsorption portion of the transient. This slow increase happens for a time duration τ_1, as it is marked in figures 5.1, and 5.2. This part signifies the time necessary for the accumulated metal clusters to disappear from the surface. This presumably, happens by either direct desorption from the indium droplets, or the indium stored in the clusters here provides a supply of excess material to replenish the indium that desorbs from the bilayer below. The intensity at the end of τ_1 returns to the value it previously had before the accumulation of indium droplets. After the excess indium n is exhausted, there is a change in the evolution of the RHEED intensity, which, again would suggest desorption takes place from a two-dimensional structure. The intensity is eventually returned to its original value, before the opening of the shutter, but this portion of the transient is much slower: while delay τ_1 is of the order of a few tens of seconds, full recovery of the RHEED intensity takes place over several minutes. Oscillations are again observed in this part, which could be correlated to a layer-by-layer depletion of the indium covering the surface. Two time intervals are defined and will be discussed here, τ_2 from the first to the second recorded intensity peak, and τ_3 from the second recorded peak to recovery. It should be noted that, while time τ_1 seems to directly depend on the impinging indium rate F_{In} (see fig. 5.1), times τ_2 , and τ_3 only depend on the substrate temperature during the experiment.

5.3 Indium adsoprtion

To further investigate the indium adsorption, and to correlate the particular features of the RHEED intensity transient responses with the indium coverage of the surface, an additional set of experiments were performed. For these experiments, the sample was kept at 485°C In such conditions, the sample temperature is low enough to safely assume any desorption can be considered negligible and all of the deposited indium remains on the GaN surface. The measurement was repeated three times, for different values of F_{in}: 0.05, 0.1, and 0.2 ML/s. In between each measurement, the substrate temperature was raised to allow for In desorption from the GaN surface, and recovery of RHEED intensity to its original value.

In figure 5.3, the results of these measurements are presented, with the normalized RHEED specular intensity being plotted as a function of the deposited indium, which equals at any time t:

$$D = F_{In}(t - t_0) \qquad (5.1)$$

where D is the amount of deposited In in MLs, F_{In} the impinging In rate in ML/s, and t_0 the time when In deposition is initiated. Zero deposition would coincide here with the opening of the In shutter.

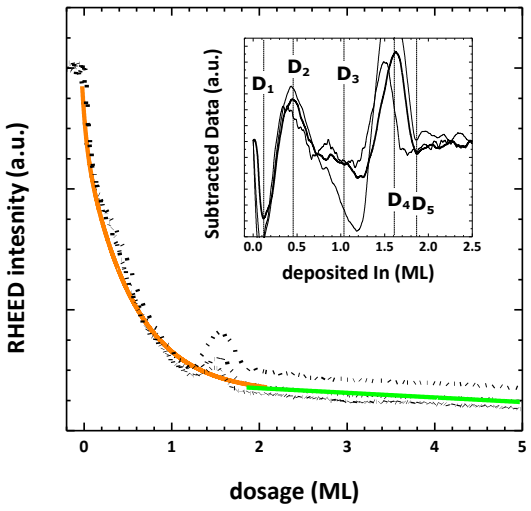

Figure 5.3: Variation of the normalized RHEED specular intensity plotted versus the amount of deposited indium at temperature T_S=485^{o}C. The green line marks the part of In accumulation. Before that, intensity is found to decay in an exponential manner here fitted by the red line. Inset presents the data after the exponential part has been subtracted. Local maxima and minima are marked.

Like before, the adsorption intensity evolution can be roughly split in two parts. The portion fitted by the green line in figure 5.3 marks the slow decrease in intensity that is related with droplets being present on the surface. Before that, the baseline of the intensity drop is found to follow an exponential decay, fitted by the red line in figure 5.3. The inset of figure 5.3 presents the particular intensity features, after the red baseline has been subtracted.

We can see from figure5.3 that the droplet state appears to begin at close to 2MLs GaN eq. of indium deposition. This suggests that prior to the formation of indium droplets, the two-dimensional indium structure consists of approximately 2 monolayers. This is similar to the bilayer structure that has been observed for Ga, as it was described in the introduction of this chapter. Furthermore, the two peaks presented in the inset of figure 5.4 suggest 2 completed monolayers of indium before accumulation starts to take place. We can theorize, therefore, that the indium adsorption happens in the following stages: Impingning indium on the GaN surface, at fist adsorbs into a single indium monolayer, here on referred to as the bottom monolayer. After the bottom monolayer is completed, a second monolayer, here on referred to as the top monolayer, is formed. After the top monolayer has also been completed, further indium that impinges on the surface starts to accumulate into droplets.

Particular feature of the adsorption transient, however, are not straightforward to correlate to indium coverage, due to several factors. Inaccuracies of the experimental setup along with errors in the values of indium fluxes, and substrate temperatures result in uncertainties of the experimental data, as we can see from the inset of figure 5.3. The surface densities of each of the two monolayers is also unknown.

Since it is difficult to form a conclusion for the surface densities for the two indium monolayers, we will, from now on, assume that each of them consists of 1ML in GaN eq. Returning to the transient response of figure 5.2, assuming the peak in intensity signifies a completed monolayer, we

can define τ_2, and τ_3 as the time it takes for the top and bottom monolayers to disappear respectively.

5.4 Rate equations

According to the above discussion, and taking into account all the possible contributing processes, the time gradient of the indium coverage can generally be described by a set of rate equations as follows:

$$\frac{\partial\theta_b}{\partial t} = F_{In}(1-\theta_b) + k_{t-b}\theta_t(1-\theta_b) - \gamma_b(\theta_b - \theta_t) \qquad (5.2)$$

$$\frac{\partial\theta_t}{\partial t} = F_{In}(\theta_b - \theta_t) + k_{n-t}n(\theta_b - \theta_t) - k_{t-b}\theta_t(1-\theta_b) - \gamma_t(\theta_t - n) \quad (5.3)$$

$$\frac{\partial n}{\partial t} = F_{In}(1-n) + k_{n-t}(\theta_b - \theta_t) - \gamma_n n \qquad (5.4)$$

where θ_b, and θ_t the surface coverages for the top and bottom monolayer respectively, n represents the amount of indium stored in the indium droplets, γ_b, γ_t, and γ_n are the desorption rates from the bottom monolayer, top monolayer, and droplets, and k_{t-b}, k_{n-t}, are the transfer rates between the top and bottom monolayer, and droplets and top monolayer respectively. A schematic representation of all these processes is presented in figure 5.4.

To extract these rate equations, we have assumed surface densities for the bottom and top monolayers equal to unity, as mentioned before. Furthermore, the equations assume a Langmuir[13] isotherm for the desorption of indium from the two monolayers. This does not appear to be a precise assumption, as we will discuss in the following paragraphs. Additionally, continuing with the analysis of the RHEED intensity transients, we will make the reasonable assumption that, during In desorption, $\theta_t \approx 1$, for the time it takes for the droplets to disappear, and $\theta_b \approx 1$ while the top monolayer desorbs.

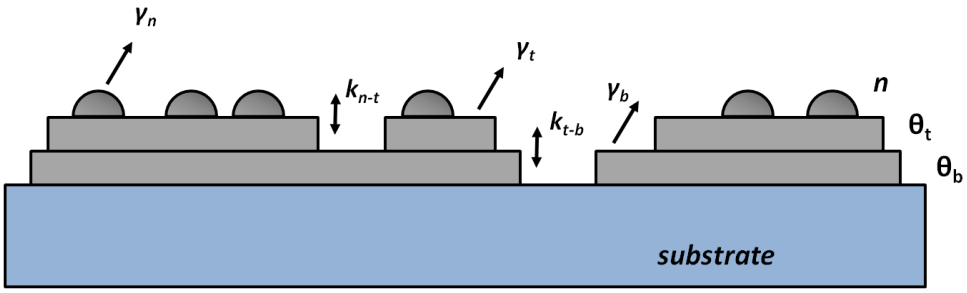

Figure 5.4: A schematic representation of the processes assuming a bilayer model for the indium coverage on the GaN surface.

5.5 Desorption from the bilayer

We have mentioned in paragraph 5.1 that time τ_3 depends on the impinging indium rate F_{In}. In figure 5.5 time τ_1 is plotted as a function of F_{In}, for different substrate temperatures. It is obvious that the dependence follows a linear trend, which points to the time interval becoming zero for a certain value of F_{In}. This is explained as follows:

According to the assumptions mentioned above, during deposition, at the moment the droplets start to accumulate, $\theta_t = 1$. Desorption from the bilayer reaches its maximum value, which is γ_t. By the time the shutter closes, the total amount of indium n_{max} that has accumulated into droplets can be approximated with the following equation:

$n_{max} = (F_{In} - \gamma_t)\Delta t$ (5.5)

where Δt corresponds to the time of indium accumulation into droplets

This, of course, assumes $F_{In} > \gamma_t$, which is always true in our case. Similarly, if τ_3 is the time it takes for n to exhaust, we can write:

$n_{max} = \gamma_t \tau_3$ (5.6)

According to the above, for $F_{In} = \gamma_t$, $n_{max} = 0$, and $\tau_3 = 0$. Thus, the maximum bilayer desorption γ_t can be found by extrapolating the value of F_{In} for which $\tau_1 = 0$. This, of course, does not consider desorption directly from the droplets, but that is inconsequential, since this would be identical for the adsorption and desorption part of the process.

Applying this method for a range of temperatures varying from 560°C to 605°C, an activation energy of $E_a = 2.03 \pm 0.07eV$ is obtained for the bilayer desorption, with a prefactor of $2.43 \cdot 10^{14} \pm \pm 0.03 \cdot 10^{14}$ when $\theta_t = 1$. The respective Arrhenius plot is presented in figure 5.5b

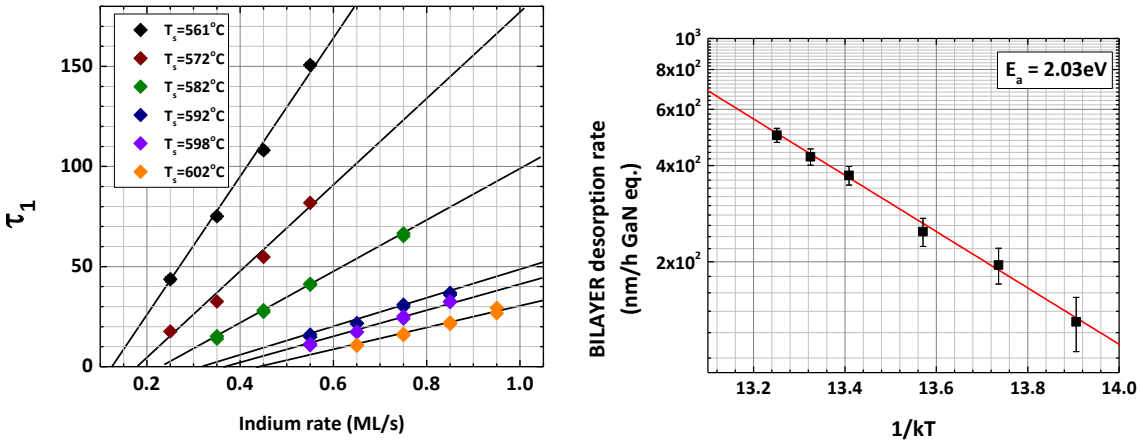

Figrue 5.5: (a) Time delay τ_1 as a function of the impinging In rate, for different substrate temperatures. (b) Arrhenius plot for the bilayer desorption; each point is extracted by extrapolating the flux for which τ_1=0 for each substrate temperature.

5.6 Coverage as a function of time

We now consider time intervals τ_2, and τ_3, which have been previously defined as the time it takes for the top and bottom monolayer to desorb, respectively. Figure 5.6a, and 5.6c present characteristic examples of these two time spans, isolated from the rest of the RHEED intensity transient, for reasons of clarity. Let us assume, for each case, that the normalized RHEED intensity, I, as a function of the surface coverage, θ, can be described by a second degree polynomial [14]:

$I(\theta) = a\theta^2 + b\theta + c$ (5.7)

For each case of the top and bottom, the following conditions apply:

$$\left\{\begin{matrix} I(1) = I_0 \\ I(0) = I_{max} \\ I(\theta_{min}) = I_{min} \end{matrix}\right\} \qquad (5.8)$$

Where I_0, the initial value of the RHEED intensity, and I_{min}, and I_{max}, the minimum, and maximum value respectively. All these parameters are shown and defined in figures 5.6a, and 5.6b. For the minimum intensity value, it further applies, supposing that the coverage decreases monotonically with time:

$$\frac{\partial I}{\partial t} = \frac{\partial I}{\partial \theta}\frac{\partial \theta}{\partial t} = 0 \rightarrow \frac{\partial I}{\partial \theta} = 0 \ \left(with \ \frac{\partial \theta}{\partial t} \neq 0\right) \qquad (5.9)$$

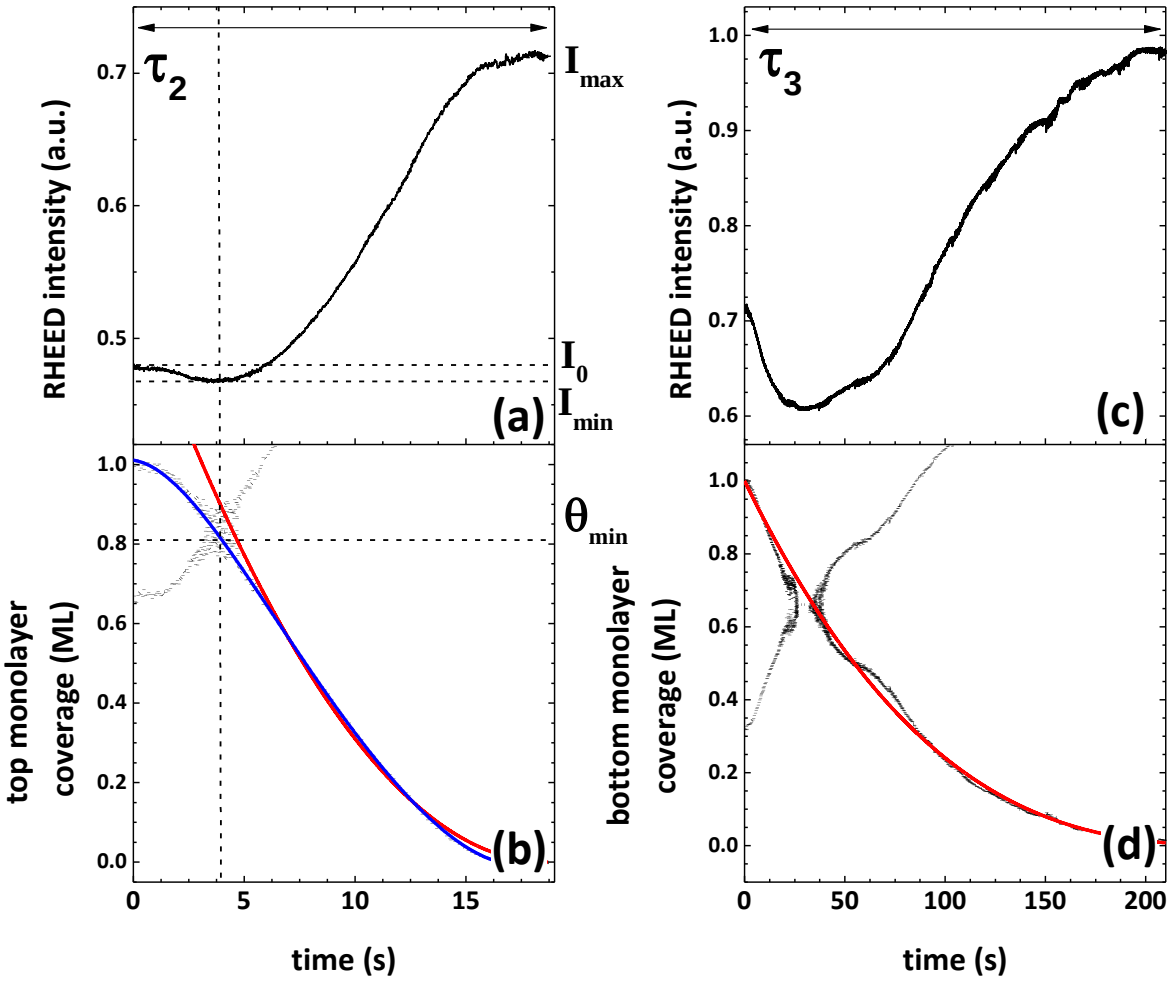

Figure 5.6: (a), and (c) present the portions of a characteristic RHEED intensity transient that correspond to times τ_2, and τ_3 respectively. (b), and (d) present the surface coverage as a function of time for the top and bottom monolayers respectively, as these are extracted according to equations (5.8), and (5.9). In figure 5.6c, a blue line is used to indicate the coverage evolution for clarity, as a guide for the eye. The red lines represent fits with equation (5.12)

Applying equations (5.8), and (5.9) to each case, we extract the coverage as a function of time for the top, and bottom monolayer. Results are presented in figues 5.6b, and 5,6d respectively.

Let us first consider the case of the bottom monolayer coverage (fig. 5.6d). For F_{In}=0, and ϑ_t=0, the rate equations of paragraph 5.4, yield:

$$\frac{\partial\theta_b}{\partial t} = -\gamma_b\theta_b \quad (5.10)$$

By integration of equation (5.10), we calculate the bottom monolayer coverage as a function of time:

$\theta_b(t) = e^{-\gamma_b t}$ (5.11).

This, as we have mentioned before, assumes a Langmuir dependence of the desorption rate on the surface coverage[15]. Fitting equation (5.11) to our experimental data, however, appears to be unsatisfactory. The coverage value, however, seems to be much better fitted, if we consider a non-Langmuir dependence, described by the following rate equation:

$$\frac{\partial\theta_b}{\partial t} = -\gamma_b{\theta_b}^{\beta} \quad (5.12)$$

where the desorption rate does not have a linear dependence on the surface coverage, but rather is proportional to the surface coverage to the power of a factor, β.

Integration of equation (5.11), gives:

$$\theta_b(t) = [1-\gamma_b(1-\beta)t]^{1/1-\beta} \quad (5.13)$$

Figure 5.7a presents the bottom monolayer coverage as a function of time, and the two cases discussed above are also presented. The dashed line corresponds to the Langmuir isotherm, whereas the solid line corresponds to the non-Langmuir case, as described by equation (5.13). It is obvious that the latter case provides a much better fit for the experimental data extracted from the RHEED intensity transients.

Such a dependence on indium coverage could be interpreted as follows. For partial coverage, the adlayer would be arranged in islands around nucleation points. It is not unreasonable to assume that it would be more energetically favorable for an indium atom to desorb from the adlayer island edges rather than from the top island surface. If this is the case, then the rate of desorption depends more on the circumference of the islands than on their surface.

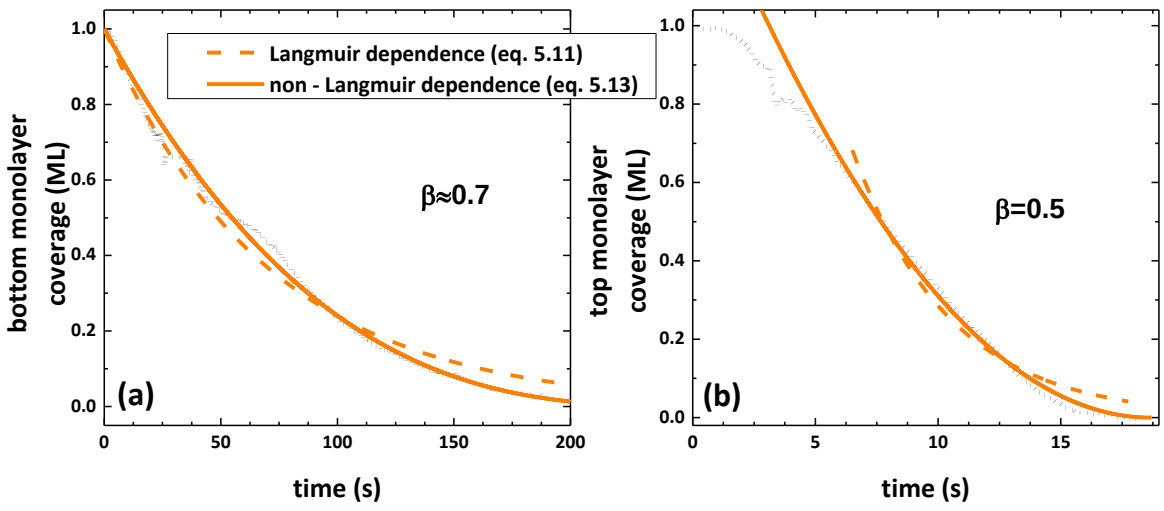

Figure 5.7: Bottom (5.7a), and top (5.7b) layer coverage as a function of time, as extracted from the experimental measurement of the RHEED intensity. The dashed and solid lines represent the dependence of coverage on time as these are calculated by assuming a Langmuir and non-Langmuir dependence on coverage of the desorption rate respectively.

Fitting with equation (5.13) for all the obtained measurements was performed and yields a power factor β=0.69±0.06, and desorption rates that are described by activation energy Ea=3.12±0.23eV, and a prefactor of $14.87 \cdot 10^{18} \pm 0.65 \cdot 10^{18}$. The corresponding Arrhenius plot is presented in figure 5.8a.

As we can see from figure 5.6b, the top monolayer coverage seems to have a more complicated dependence on time. The first part of the coverage evolution, in particular seems to decrease at a lower rate and is concave downward as opposed to both the bottom monolayer transient, and the rest of the top monolayer transient. These both are concave downward. This could be due to the fact that at the first stages of desorption for the top monolayer, the RHEED intensity is affected by the previous part of the transient (where droplets are present) in one of two ways. First, it is possible that the top monolayer coverage drops to a value smaller than 1 for $n \neq 0$, i.e. the indium droplets have not been completely exhausted and some residue material is still present on the top monolayer. The second reason is that the RHEED intensity here is much too close to its minimum value, which is dictated by background fluorescence of the screen due to electron dispersion. The errors, therefore, in this area are proportionally much greater, as the real value of intensity is masked by the background fluorescence. For the second part of the transient, however, which is concave upwards, the coverage can be fitted quite well, if we again consider:

$$\frac{\partial \theta_t}{\partial t} = -\gamma_t {\theta_t}^{\beta} \rightarrow \theta_t(t) = [1 - \gamma_t (1-\beta) t]^{1/1-\beta} \qquad (5.14)$$

with a factor of β=0.5. Figure 5.7b presents the top monolayer coverage as a function of time along with the fit of the coverage as described by equation (5.14) represented by the solid line. Again, the dashed line corresponds to a Langmuir dependence of desorption rate on coverage, and it is found that it is inadequate to describe the evolution of coverage with time. Fitting with equation (5.14) for all the obtained measurements results in the Arrhenius plot presented in figure 5.8b. It is found that the desorption rate is described by activation energy E_a=2.67±0.19eV, and a prefactor of $3.98 \cdot 10^{17} \pm 0.30 \cdot 10^{17}$.

The reader, however, should keep in mind that for such low intensity vales, there are large errors, as it is discussed above, and it is possible that the top monolayer transient of figure 5.7b does not accurately describe the actual evolution of the surface coverage during that time.

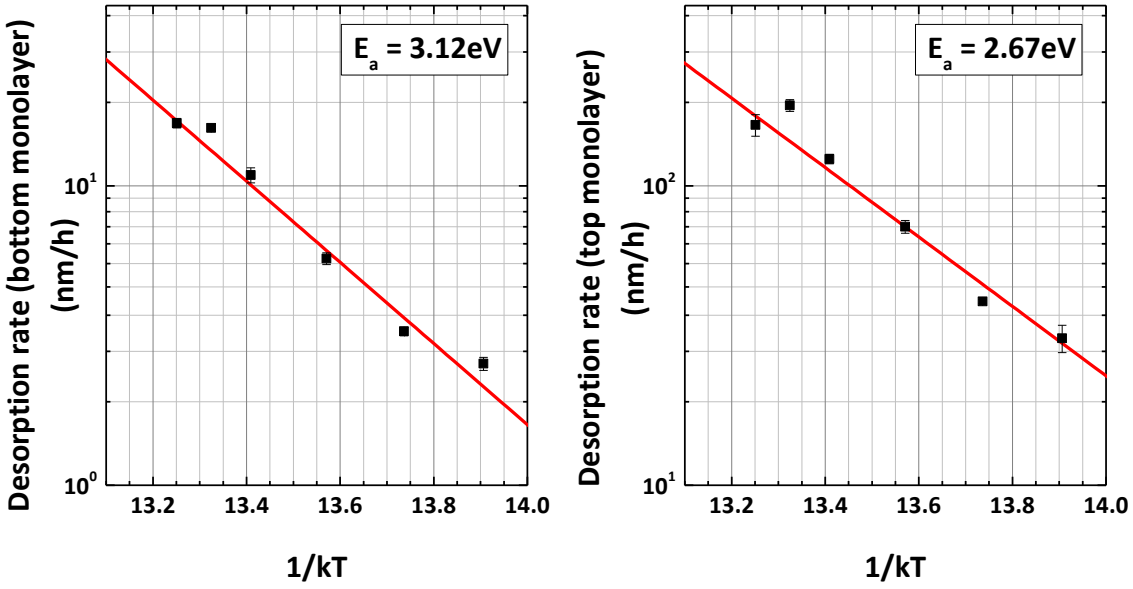

Figure 5.8: Arrhenius plots for the bottom (a) and top (b) layer desorption as resulting from the fit with equation (5.13)

REFERENCES

1. Copel, M., et al., *Surfactants in epitaxial growth.* Physical Review Letters, 1989. **63**(6): p. 632-635.
2. Morkoç, H. and I. Wiley. *Handbook of nitride semiconductors and devices*. 2008; Available from: http://onlinelibrary.wiley.com/book/10.1002/9783527628438.
3. Adelmann, C., et al., *Dynamically stable gallium surface coverages during plasma-assisted molecular-beam epitaxy of (0001) GaN.* Journal of Applied Physics, 2002. **91**(12): p. 9638-9645.
4. Mula, G., et al., *Surfactant effect of gallium during molecular-beam epitaxy of GaN on AlN (0001).* Physical Review B, 2001. **64**(19): p. 195406.
5. Northrup, J.E., et al., *Structure of GaN(0001): The laterally contracted Ga bilayer model.* Physical Review B, 2000. **61**(15): p. 9932-9935.
6. Adelmann, C., et al., *Gallium adsorption on (0001) GaN surfaces.* Physical Review B, 2003. **67**(16).
7. Smith, A.R., et al., *Reconstructions of GaN(0001) and (0001) surfaces: Ga-rich metallic structures.* Journal of Vacuum Science & Technology B: Microelectronics and Nanometer Structures Processing, Measurement, and Phenomena, 1998. **16**(4): p. 2242-2249.
8. Brandt, O., et al., *Ga adsorption and desorption kinetics onM-plane GaN.* Physical Review B, 2004. **69**(16).
9. He, L., et al., *Gallium desorption kinetics on (0001) GaN surface during the growth of GaN by molecular-beam epitaxy.* Applied Physics Letters, 2006. **88**(7): p. 071901.
10. Zheng, L.X., M.H. Xie, and S.Y. Tong, *Adsorption and desorption kinetics of gallium atoms on $6H\ensuremath{-}\mathrm{SiC}(0001)$ surfaces.* Physical Review B, 2000. **61**(7): p. 4890-4893.
11. Widmann, F., et al., *Improved quality GaN grown by molecular beam epitaxy using In as a surfactant.* Applied Physics Letters, 1998. **73**(18): p. 2642-2644.
12. Monroy, E., et al., *Surfactant effect of In for AlGaN growth by plasma-assisted molecular beam epitaxy.* Journal of Applied Physics, 2003. **93**(3): p. 1550-1556.
13. Langmuir, I., *The Vapor Pressure of Metallic Tungsten.* Physical Review, 1913. **2**(5): p. 329-342.
14. Van Hove, J.M. and P.I. Cohen, *Reflection high energy electron diffraction measurement of surface diffusion during the growth of gallium arsenide by MBE.* Journal of Crystal Growth, 1987. **81**(1): p. 13-18.
15. Vol'kenshtein, F.F., *Electronic processes on semiconductor surfaces during chemisorption*. 1991, New York: Consultants Bureau.

CHAPTER 6: Conclusions

6.1 Summary of key points

Having studied the kinetic processes for InGaN decomposition, and In desorption individually, we will presently try to apply this knowledge to investigate how they affect the growth of InGaN. We will consider their effect on the growth conditions, and correlate it with results for In incorporation and film properties. With the new information, we will return the discussion to InGaN growth as a function of temperature by re-examining samples from series S1, and S2 of chapter 3. Before we begin, let us review some key points from the previous chapters.

Effective growth conditions vs nominal growth conditions: At the time of InGaN MBE growth, the nominal arrival rates are not indicative of the actual growth conditions on the sample surface. The effective arrival rates are affected by the desorption and decomposition rates according to the following (see chapter 3):

$F'_{Ga} = F_{Ga}$ (6.1)

$F'_{In} = F_{In} - F_{In}^{des}$ (6.2)

$F'_{N} = F_{N} - F_{InGaN}^{Dec}$ (6.3)

Effective growth conditions are then defined as metal-rich, for $F'_{Ga} + F'_{In} - F'_{N} > 0$, and N-rich for $F'_{Ga} + F'_{In} - F'_{N} < 0$. The effective growth conditions are the key to determining the growth mode and process for In incorporation, and therefore, film properties and composition.

InGaN growth as a function of substrate temperature: In chapter 3, samples of series S1, and S2 were grown with varying substrate temperatures. Judging by evidence provided by RHEED monitoring, surface morphologies, and the growth mode, it was suggested that samples of S2 with very low growth temperatures were grown under effective N-rich conditions (section (I) of figure 3.2). Samples with intermediate temperatures were grown under III-rich conditions (section (II)), and for higher substrate temperatures (section (III)) evidence points to growth under near stoichiometry.

Lower substrate temperatures were found to promote growth of InGaN films with uniform composition, with no phase separation. The samples structural and electrical properties were also found to benefit from the reduction of the growth temperature.

Preferential incorporation of Ga: For metal-rich conditions, when the available nitrogen sites are limited, it was shown that Ga is always incorporated into the InGaN lattice with priority over In (see chapter 3). Then the indium content of the resulting InGaN film can be calculated by:

$x = 1 - \frac{F'_{Ga}}{F'_{N}}$ (6.4).

For N-rich conditions on the other hand, when there is an abundance of nitrogen sites, InN mole fraction is given by:

$x = \frac{F'_{In}}{F'_{In} + F'_{Ga}}$ (6.5)

Model for InGaN thermal decomposition: For effective metal-rich conditions, the decomposition rate was precisely determined (chapter 4). It was revealed that although InGaN decomposition has an Arhenius-type dependence on the substrate temperature, its dependence on the film composition –as previously suggested in literature- is questionable. It rather appears to be a strong function of the growth surface stoichiometry, as described by the nominal arrival rates, with the aid of parameter x':

$$x' = 1 - \frac{F_{Ga}}{F_N} \quad (6.6)$$

Excessive decomposition rates were found to be detrimental to the alloys homogeneity, structural, and optical properties as evident by results from XRD, AFM, and PL. With these criteria, an optimum growth window for InGaN films was identified for different In contents and growth temperatures.

Indium bilayer: It was established that indium is adsorbed into a GaN (0001) surface in a structure that is very similar to the well-known Ga-bilayer (chapter 5). First, a bottom layer wets the GaN surface. This layer is characterized by coverage θ_b, and a maximum desorption rate of γ_b. Once this bottom layer is full, adsorption continues and a second monolayer is formed, with characteristic variables coverage θ_t, and a maximum desorption rate of γ_t. When this layer is also completed, any more indium impinging on the surface accumulates on top of it to form indium droplets. The desorption process follows symmetrical steps. First, indium stored in the droplets is exhausted, while the bilayer underneath remains intact; then, for the time it takes the top layer to desorb, $\theta_b \approx 1$; as a final step, the bottom monolayer is also desorbed.

The desorption rate from the top, and bottom monolayer is found to have a non-Langmuir dependence on coverage. The rate equation that better describes top, and bottom monolayer desorption is

$$\frac{\partial \theta}{\partial t} = -\theta^{\beta}\gamma \rightarrow F_{In}^{des} = \theta^{\beta}\gamma \quad (6.7)$$

with $\beta \approx 0.7$ for the bottom monolayer. $\beta = 0.5$ is suggested for the top monolayer, even though further investigation is needed to confirm this.

6.2 In incorporation as a function of surface coverage

To elucidate the effect of the kinetic mechanisms on the growth process, let us reconsider the samples of series S1, and S2 first discussed in chapter 1. Figure 6.1 presents again the InN mole fraction as a function of substrate temperature for both series. Sections (I), (II), and (III) are also shown.

We first consider effective metal-rich conditions. Then the InN mole fraction should be calculated by equation (6.4) as discussed above. The calculation should be straightforward, because it is only a function of the known nominal Ga, and N rates, and the rate of InGaN decomposition, which precisely predicted by the model of chapter 4. The result of this calculation is presented by the green lines in figure 6.1 for both series S1, and S2.

It is clear from figure 6.1 that the InN mole fraction predicted by equation (6.4) is in very good agreement with the experimental data of series S1, and S2, for section (II). It is reminded that section (II) samples were previously identified as grown under effective metal-rich conditions. For these samples, droplets are always observed on the film surface, which, according to the discussion of chapter 5, means a complete indium bilayer.

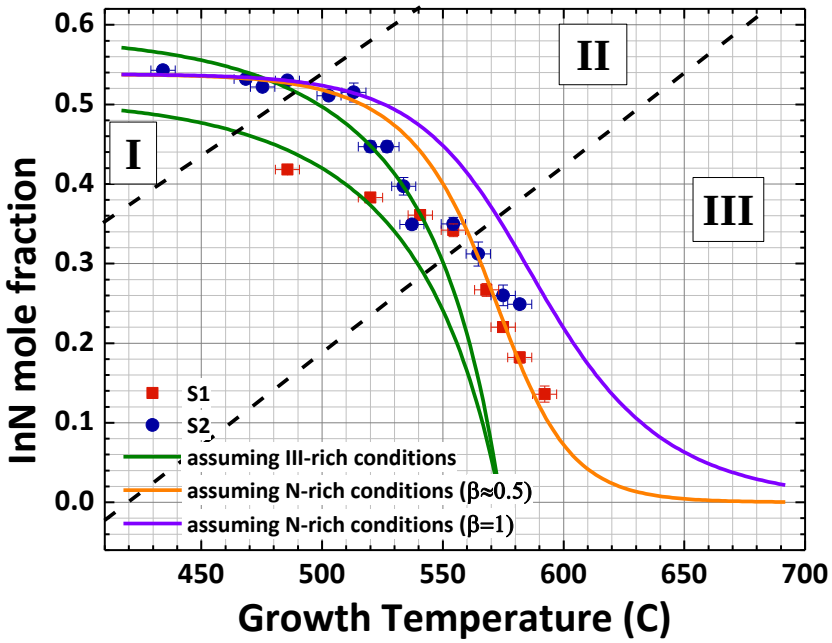

Figure 6.1:.InN mole fraction as a function of growth temperature for series S1, and S2 samples. Sections (I), (II), an (III) are shown. The green lines are predictions for the InN mole fraction, assuming effective N-rich conditions, for both series. The blue and orange lines are predictions assuming effective N-rich conditions. The blue line considers a Langmuir dependence on coverage for the In desorption (β=1), while the blue line considers a non-Langmuir dependence (β=0.5).

It follows that for section (II) samples, and effective metal-rich conditions:

$$\left.\begin{matrix}\theta_t = 1\\ \theta_b = 1\end{matrix}\right\} \qquad (6.8)$$

Next, we consider N-rich conditions. In this case, In incorporation depends on metal nominal arrival rates, as well as the indium desorption. According to the desorption rates measured in chapter 5, desorption from the bottom layer is very low to considerably affect the growth conditions in this temperature rate. Let us, therefore, consider the bottom monolayer complete, and a desorption rate from the top monolayer, according to equation (6.7). As discussed in chapter 5, the desorption rate has an Arrhenius dependence on temperature, and it further depends on the indium coverage, according to equation (6.7). The indium coverage, however, is unknown. To continue with the calculation, a first reasonable approximation for the coverage would be to set its value equal to the InN mole fraction. The In content can then be found by solving the following equation:

$$x = \frac{F_{In} - x^{\beta}\gamma}{F_{In} - x^{\beta}\gamma + F_{Ga}} \qquad (6.9)$$

In figure 6.1, two cases are shown. The blue line assumes β=1, and a Langmuir dependence of the desorption rate on temperature. The orange line assumes β=0.5 (non-Langmuir dependence).

For the very low substrate temperatures of section (I), the desorption rate is near zero, and the two lines converge to the InN MF value given by nominal values $\left(x = {}^{F_{In}}/_{F_{In} + F_{Ga}}\right)$. This value is also confirmed by the experimental data. Here, it is reminded that characterization of the samples

showed rough surfaces, and 3D structures, usually associated with growth under N-rich conditions. For section (III), the experimental data seem to follow the orange line very well. For this section, it is reminded that experimental evidence points to near stoichiometric growth.

Even though section (I) and section (III) samples both seem to follow the InN MF predicted by equation (6.9), there is significant difference in the two sections' samples from a morphological point of view. This could be explained by the presence or absence of the indium bilayer.

For section (I), desorption and decomposition happen at very low rates, and have very little effect on the growth conditions. In is quickly incorporated into the lattice and does not have the chance to stay on the surface. Coverage for the top monolayer is zero, and for the bottom layer, the coverage is lower than unity. Without the indium bilayer to act as a surfactant, the growth happes in a 3D way, resulting in the morphological characteristics typical for section one. We can write then that for section (I), or effective N-rich conditions:

$$\begin{Bmatrix} \theta_t = 0 \\ 0 \leq \theta_b < 1 \end{Bmatrix} \quad (6.10)$$

For section (III), on the other hand, desorption and decomposition rates cannot be overlooked. The fact that InN MF appears to be predicted by equation (6.8) quite accurately suggests that there is an excess of N atoms. Furthermore, the approximation $\theta_t \approx x$, suggests that the In bilayer is present for these conditions, with a full bottom monolayer, and a partially completed top monolayer. The presence of the bilayer, albeit in partial coverage, could account for the near stoichiometric effective conditions indicated by the experimental evidence. The completed In adlayer here could accommodate two-dimensional growth by increasing adatom mobility on the surface, leading to the smooth surface morphologies and streaky RHEED images that suggested the stoichiometry conditions in the first place. Then, for section (III) and effective near-stoichiometric conditions, it applies for the In coverage:

$$\begin{Bmatrix} 0 \leq \theta_t < 1 \\ \theta_b = 1 \end{Bmatrix} \quad (6.11)$$

The three cases described above are summarized schematically in figure 6.2.

Even though, these different cases describe the InN mole fraction quite well for the different branches of series S1, and S2, there are some issues that need to be addressed. Primarily, it is not clear from figure 6.1, at which temperature, and in what way, the transition between different sections and growth conditions happens. Especially for the transition between section (II) and (III), there is clearly a discontinuity between predicted metal-rich values (green lines), and stoichiometric values (orange line). This discontinuity, presumably, is due to the fact that, for section (II), the coverage was approximated with the InN mole fraction. Although this might be a reasonable assumption for higher temperatures, at the transition between metal-rich and stoichiometry, there appears a sudden change in the value of coverage from $\theta_t=1$ (section (II)) to $\theta_t<0.5$ (section (III)). It is much more likely, that as the temperature increases gradually, and the desorption and decomposition rates change slowly, the coverage also changes from $\theta_t=1$ to $\theta_t<0.5$ in a continuous manner. The problem then is, what is an adequate approximation for the In coverage?

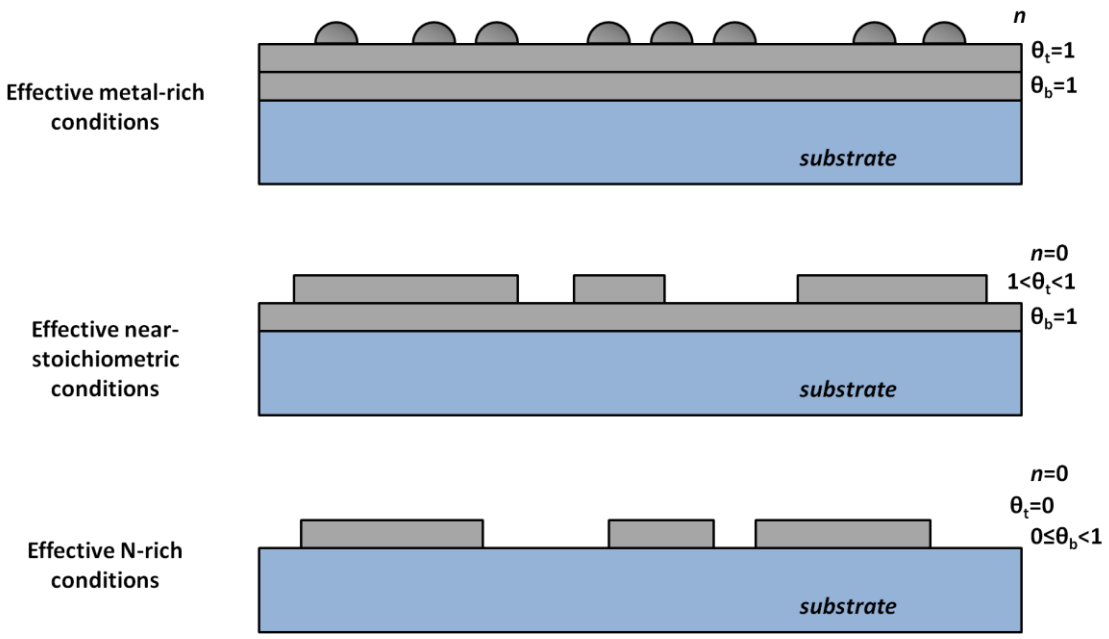

Figure 6.2:.Schematic representation of the indium structure on the sample surface during InGaN MBE, for three cases: effective metal-rich conditions, effective near-stoiciometric conditions, and effective N-rich conditions.

In order to find an approximation for the indium coverage, another problem arises. The effective arrival rates for all elements must be known. As far as metal rates are concerned, and, having determined the desorption rate, we have by now a quite clear picture. For section (III), the effective metal rates are given by:

$$F'_{Ga} = F_{Ga}$$
$$F'_{In} = F_{In} - \theta_t^{0.5}\gamma_t \qquad (6.12)$$

For the effective N arrival rate, however, the rate of InGaN decomposition needs to be known. It is reminded here that the model extracted in chapter 4 only applies to effective metal-rich conditions, ie for θ_t=1. For θ_t<1, the model needs to be adjusted to describe the decomposition rate more precisely. In figure 6.3, the green lines represent the decomposition rates as a function of temperature, for series S1, and S2, as these are predicted by our decomposition model, without any modification. If this was the case, the decomposition rate would quicky reach such a high value, that InGaN growth would almost be completely impossible. Thicknesses of samples belonging in section (III) certainly to not justify such high rates of decomposition. Furthermore, morphologically, the samples do not exhibit the characteristics related with such extreme decomposition conditions (see chapter 4).

A reasonable way to modify the decomposition model would be the following. For θ_t<1, there are parts of the surface where the top monolayer is present, and parts where it is not (figure 6.2). Where the top monolayer is present, conditions are locally very close to effective metal-rich. The decomposition model gives an accurate value for these parts of the surface. Where there is no top monolayer, excess N is such that the decomposition process is hindered altogether, or if it happens, the N atoms are replaced faster than they are lost. The total decomposition rate would then be $\theta_t F_{InGaN}^{Dec}(x', T_{gr})$, where $F_{InGaN}^{Dec}(x', T_{gr})$ is the decomposition rate according to the model, which,

as we know, depends on the growth temperature, as well as on parameter x'. Effective N arrival rate for section III is then:

$F_N' = F_N - \theta_t F_{InGaN}^{Dec}(x', T_{gr})$, (6.13)

The orange lines in figure 6.3 represent the model decomposition rate multiplied by the top monolayer coverage. Such rates of decomposition are more reasonable, and are in agreement with the sample characterization, as well as with the discussion that follows.

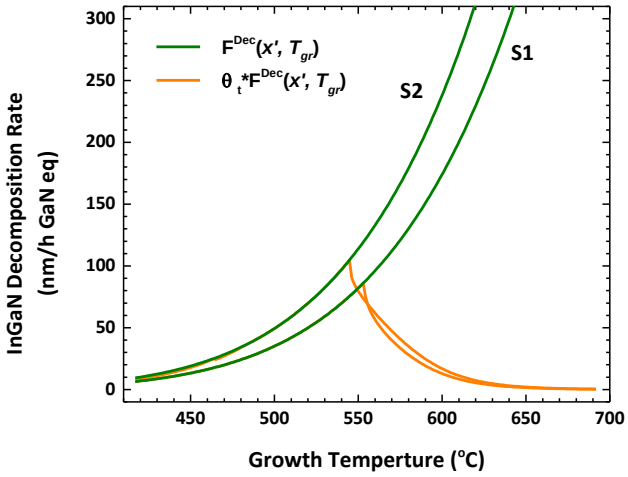

Figure 6.3:.InGaN decomposition rate as a function of temperature. The green lines are the values predicted by the decomposition model of chapter 4, for series S1, and S2. The orange lines are the values of the composition rates of the model multiplied by the respective In coverage for each temperature.

Taking all of the above into account, it was found that a good approximation for the In coverage would be the following:

$\theta_t = \frac{F_{In}'}{F_N' - F_{Ga}'} = \frac{F_{In} - \theta_t^{0.5}\gamma_t}{F_N - \theta_t F_{InGaN}^{Dec} - F_{Ga}}$ (6.14)

This approximation takes a similar approach to that of chapter 4, where it was found that surface conditions are more important in affecting the decomposition than the InN mole fraction. Equation (6.14) could be interpreted as the ratio of In atoms to the available In sites (those sites not occupied by Ga). It is a dynamic description of the surface conditions. Other approaches, including the III/V ratio were examined and it was found that they failed to describe the In coverage correctly.

Figure 6.4a presents the In coverage as it was calculated by equation (6.14), for series S1, S2. Using this value for the coverage, figure 6.4b presents the metal excess $F_{Ga}' + F_{In}' - F_N'$ as a function of the growth temperature for both series. This calculation seems to predict very well the effective growth conditions, as those have been described for sections (I), (II), and (III), which are shaded with different colors in figure 6.4b.

The calculation predicts a metal excess for all section (II) samples (shown with a blue background). On the other hand, a nitrogen excess is calculated for both sections (I), and (III). The temperatures at which the transitions between different effective conditions take place, are also well predicted.

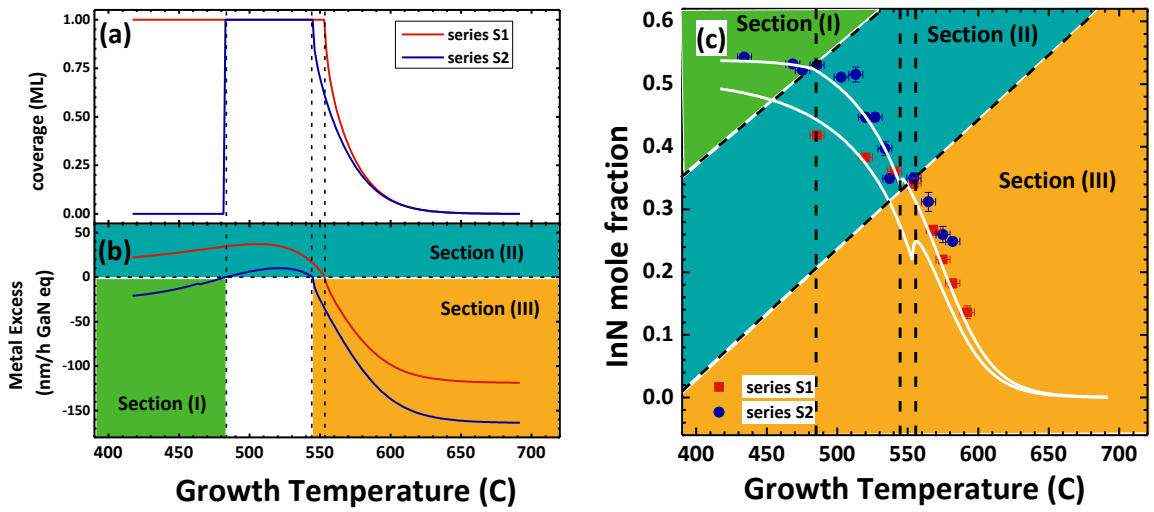

Figure 6.4:.(a) Indium coverage as a function of substrate temperature as given by solving equation (6.14) for series S1 (with red), and (S2). (b) Metal excess as a function of the substrate temperature as a result of effective growth conditions, for both series. The different sections are shadowed with different colors. (c) InN mole fraction as a function of temperature. Experimental results are presented by red squares (S1), and blue circles (S2). Sections (I), (II), and (III) are shadowed with the same colors are in figure (b).

Since the effective conditions can be well predicted, a calculation for the InN mole fraction as a function of temperature can be performed, by applying the appropriate formula for In incorporation (eq. (6.5) for metal-excess, and (6.6) for N-excess). The result of this calculation is presented in figure 6.4c with the white lines. Experimental results are also presented and sections (I), (II), and (III) are marked for reference. As we can see, the value for InN mole fraction follows a continuous line, and the calculation follows the experimental results with good agreement.

It should be noted here the calculation shown in figure 6.4b predicts a large nitrogen excess for section (III). This could be interpreted as a problem, since such a high nitrogen excess does not explain the sustenance of effective near-stoiciometric conditions. In such a case, the indium stored in the top monolayer would be consumed and conditions would soon switch to effective N-rich, with θ_t=0. However, the reader is reminded that for areas where the top monolayer is absent, we have considered that decomposition is either hindered, or N atoms are replaces faster than they are lost. The calculation of the metal excess shown in figure 6.4b considers the same thing. This hypothesis is reasonable and works for predicting the indium coverage and InN mole fraction, but to know the precise value of the metal excess, the decomposition rate for effective N-rich conditions should be known. If the decomposition at such areas is taken into account, it might counterpoise the N excess to zero. Unfortunately, there is no information available on decomposition for effective N-rich conditions, as we have explained before. It is, therefore, very difficult to make a safe assumption for the III/V ration in section (III). One thing of note, however, is that, at higher temperatures, for $\theta_t \approx 0$, the metal excess does appear to reach to a saturation value. This possibly corresponds to decomposition rate for effective N-rich conditions at such a temperature. Again, more information is needed to come to a clear conclusion on this matter.

CHAPTER 7: InGaN Heterostructures and ongoing research

7.1 Introduction

The present work has, in previous chapters, covered a detailed study on the kinetic processes that take place during epitaxy. These processes have been related to the growth conditions, namely the substrate temperature, and element arrival rates. A lot of the problems associated with the MBE growth of InGaN have been addressed, which now gives us a better understanding of how to develop quality InGaN materials for photovoltaic applications. In this direction, the present work will be concluded by presenting some initial results of InGaN heterostructures to be used in photovoltaic and other applications, as well as some results of preliminary InGaN photovoltaic devices. Of course, even though the ground has been laid, there is still a long way to go before efficient solar cells can be achieved. With a much better understanding of the material growth and properties, a number of further problems need to be addressed for device application. These problems go beyond the scope of the present work. The first steps, however, towards that goal have already been taken, and we will take a brief look at them in the present chapter. First, a few multiple InGaN/GaN quantum wells that were grown in the framework of this work will be discussed. Secondly, a different approach is examined, which involves InGaN on *p*-type Si heterostructures. Lastly, two preliminary photovoltaic devices that were developed are presented.

7.2 InGaN/GaN muptiple quantum well structures

InGaN/GaN multiple quantum wells (MQW) are structures of significance, not only for photovoltaic devices, where they can act as the active layer[1-4], but also for light emitting diodes[5], as well as laser diodes[6], where they are widely used. For such reasons, it would be interesting to extend the InGaN research to study the growth and characteristics of MQW structures. As a first step to that direction, a few preliminary InGaN/GaN multiple well structures were grown by Molecular Beam Epitaxy. High resistivity commercial GaN(0001)/*c*-Al_2O_3 wafers were used as substrates Reflection High Energy Electron Diffraction (RHEED) was used to monitor the growth in situ, and after the samples were removed from the growth chamber, they were characterized by High-Resolution X-ray Diffraction (HR-XRD), Transmission Electron Microscopy (TEM), and photoluminescence (PL) spectroscopy. The samples that will be discussed here include G2587 a MQW structure of 10 periods, and a series of four samples, which includes samples G2906, G2908, G2909, and G2914, with identical growth conditions for the InGaN layer, and different number of periods. The growth details for the InGaN layer for each of the samples are summarized in table VI, along with nominal thicknesses for the InGaN well, and GaN barrier layers, number of periods for

each sample, and whether or not the MQW structure was completed with a GaN cap layer. For the GaN barrier layers, the growth temperature was 700°C, but in the G29- series samples, part of the GaN layers were grown at a lower temperature as a way to prevent indium desorption and roughening for the InGaN layer. These details are also included in table VI.

Sample	InGaN well layer					
	Nominal InN MF	Nominal thickness (nm)	T_{gr} (°C)	N rate (nm/h GaN eq.)	Ga rate (nm/h GaN eq.)	In rate (nm/h GaN eq.)
G2587	40%	2.73	485	280	168	116
G2906	10%	3	590	75	65	127
G2908	10%	3	590	75	65	127
G2909	10%	3	590	75	65	127
G2914	10%	3	590	75	65	127

Sample	GaN barrier layer			Number of periods	GaN cap layer (nm)
	Total Nominal GaN barrier thickness (nm)	Low Temperature GaN (°C)	Low Temperature GaN thickness (nm)		
G2587	15	No	0	10	No
G2906	14	620	2	3	150
G2908	14	620	2	3	150
G2909	14	620	2	2	150
G2914	14	620	2	4	150

Table VI: Growth details for the InGaN/GaN MQW structures discussed in this chapter.

Figures 7.1a, b, c, and d present a few characteristic RHEED images acquired during the growth of sample G2587. The observed RHEED patterns were streaky for the growth of all the GaN barrier layers. As far as the growth of the InGaN layers is concerned, the RHEED patterns were less streaky, and gradually became spottier as the growth progressed, and more InGaN layers were deposited. This suggests that for the first few InGaN layers, growth happened in a way that closely approximated two-dimensional growth, and as more layers were deposited, the growth surface exhibited more three-dimensional structures. This observation agrees with TEM results. A HR-TEM image of sample G2587 is presented in figure 7.1(e). A rather raffled structure is revealed, especially for the InGaN layers closer to the top. The roughening of the MQW layers can be due to the lack of the low-temperature GaN layer for this sample. A more detailed TEM study of this sample can be found in [7].

Results from the characterization of sample G2587 with XRD are presented in figure 7.2. In figure 7.2a the symmetric ω-2ϑ scan around the (0002) Bragg point is shown. We can clearly make out a clean, narrow peak from the InGaN layers, which has a significant intensity. Furthermore, the Reciprocal Space Map (RSM) around the $(10\bar{1}5)$ reflection, shown in figure 7.2b reveals that the elastic strain for the InGaN layers is close to 100%. From fringe analysis[8], we calculate a total thickness of 127.02±5.68nm for the entire structure, and a period thickness of 12.80±0.22nm and an average composition of 0.10±0.01 InN MF, which is close to the value predicted by the nominal

conditions. It was attempted to fit the data to model simulation results to acquire exact values for the thickness and composition of the InGaN layer, but the results were inconclusive, likely due to the raffled structure of the layers.

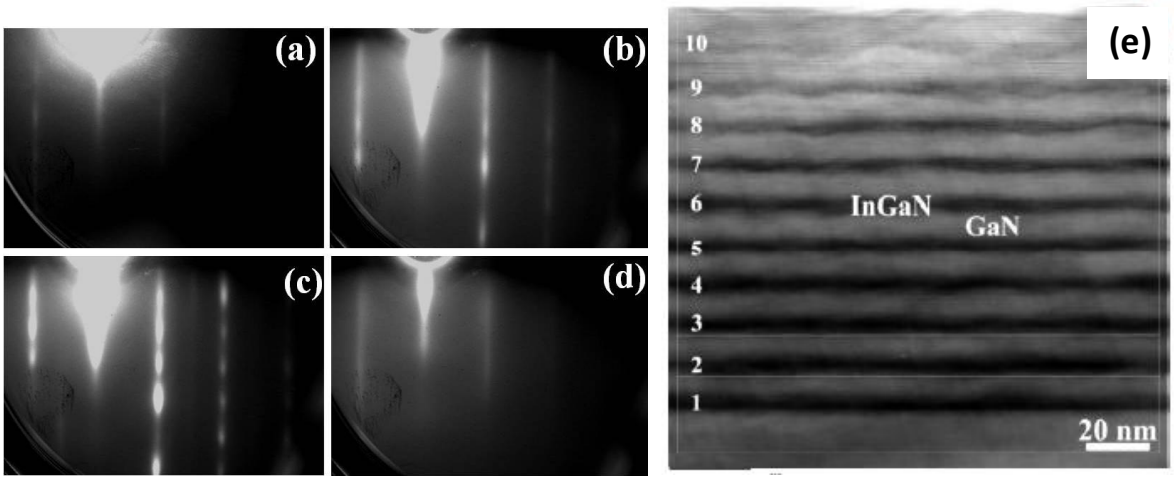

Figure 7.1: Figures (a), (b), (c), and (d) present RHEED images obtained during the MBE growth of sample G2587 for the first InGaN well layer, the first GaN barrier layer, the second InGaN well layer, and second GaN barrier layer respectively. Figure (e) is an HRTEM overall image of the sample G2587 MQW structure obtained along the $[11\bar{2}0]$ projection direction[7]

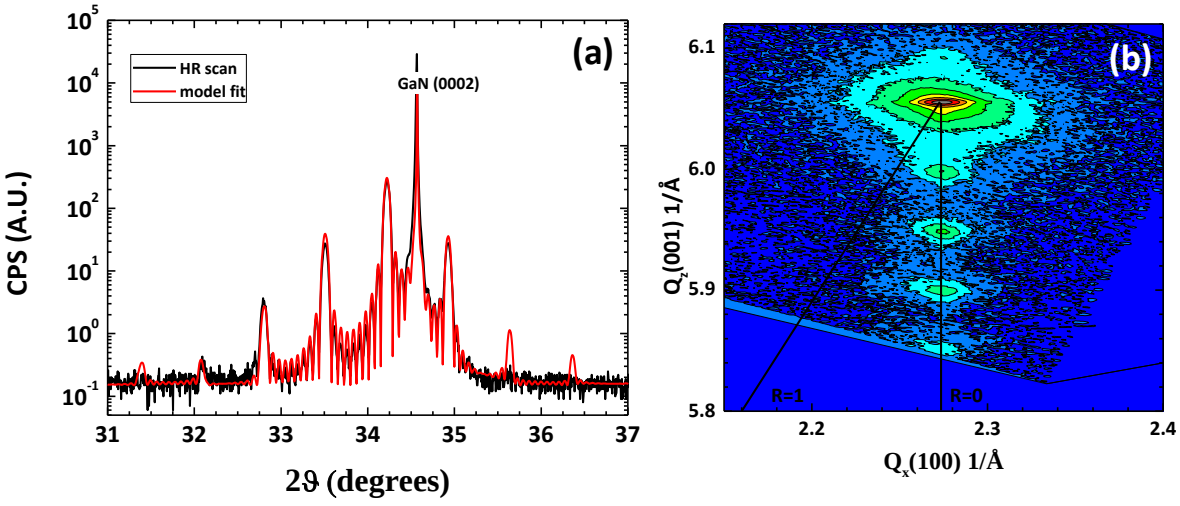

Figure 7.2: In (a), the HR-XRD ω-2ϑ scans around the (0002) Bragg reflection for sample G2587 is presented. In (b) the RSM around the $(10\bar{1}5)$ reflection for sample G2587 is presented. The lines labeled R=0 and R=1 mark expected peak positions of fully strained and fully relaxed InGaN layers respectively.

PL measurements at different temperatures were also performed. The PL emission spectrum of sample G2587 is shown in figure 7.3a. We can distinguish two distinctive emission bands related to the InGaN/GaN structure: one is centered at 2.35eV, referred to as I_1, and one at 2.91eV, referred to as I_2. Both bands show high PL emission intensity, suggesting strong confinement of carriers. This is

further supported by figure 7.3b, where the integrated PL intensity as a function of temperature is presented for each band, as well as for the GaN peak for comparison. The decrease of PL intensity as the temperature rises is much slower for the InGaN/GaN MQW peaks than it is for the GaN peak, especially in the case of I_1. Such strong carrier confinement can be a significant advantage when considering light emitting applications in longer wavelengths.

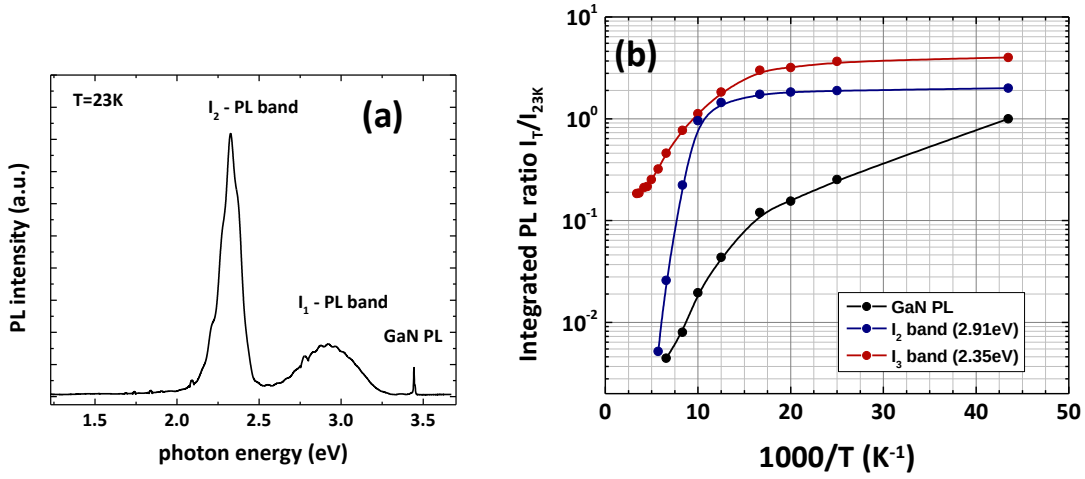

Figure 7.3: In (a), the low temperature (23K) PL emission spectrum of sample G2587 is presented. (b) shows the evolution of the integrated PL intensity of I_1, I_2, and GaN peaks as a function of temperature. The intensity for each band is normalized to its respective value at 23K. The curves are relatively shifted for clarity.

For series G29- samples, a lower number of periods was realized, with a lower target for the InGaN layer InN MF (10%). For these samples, the RHEED patterns were consistent throughout the duration of the growth. This is possibly due to the InN MF of the InGaN layer being considerably lower than that of sample G2857, which means a lower lattice mismatch, along with the fact that the GaN barrier layers were grown in part at a lower temperature. Figure 7.4a presents an example of a HR-XRD ω-2ϑ scans around the (0002) Bragg reflection, along with the fitting to the simulated model, which gave much better results this time. The model parameters were 0.12 InN MF for the InGaN layers, and thicknesses of 2.62nm, and 12.02nm for the InGaN, and GaN layers respectively. These results are close to the nominal values. In figure 7.4b the room temperature photoluminescence spectra are presented for series G29- samples. The PL emission intensities for the MQW structures seem to be comparable to the GaN substrate emission peak. Overall, these preliminary results on InGaN/GaN multiple quantum well structures appear to be very encouraging for application.

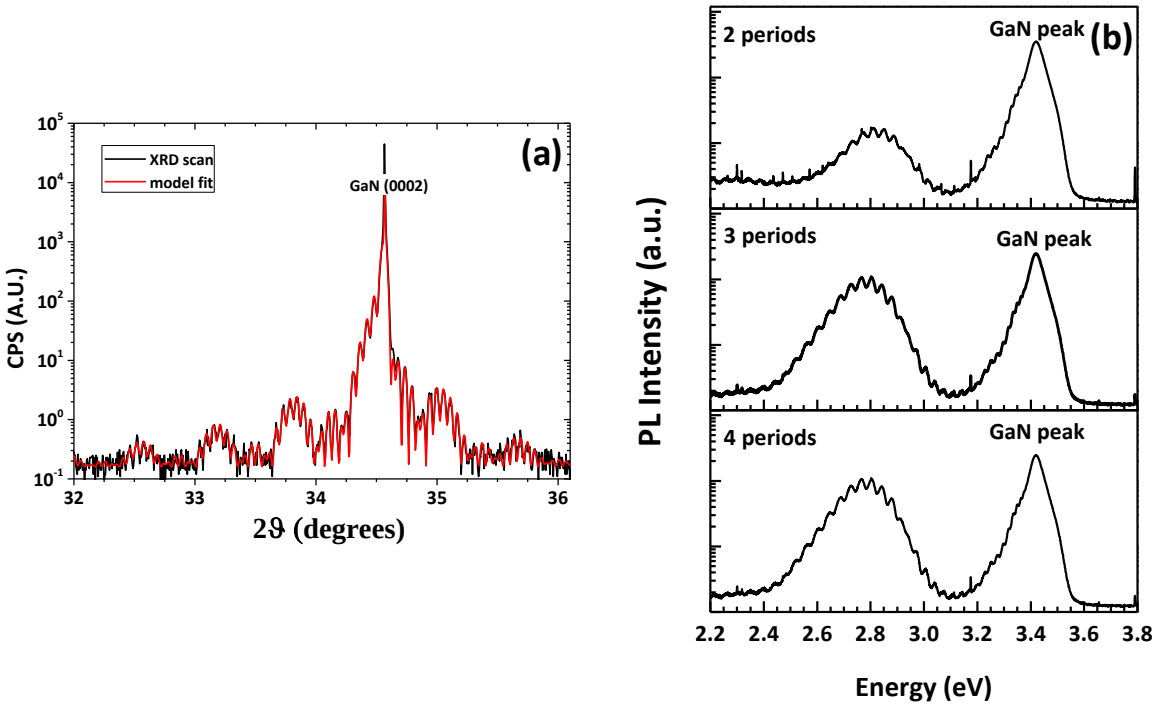

Figure7.4 In (a), a characteristic HR-XRD *ω-2ϑ* scan around the (0002) Bragg reflection for one of series S29-samples is presented with the black line, while the red line is the result of fitting the XRD spectrum to the model structure with parameters 0.12 InN MF for the InGaN layers, well thicknesses of 2.62nm, and barrier thickness 12.02nm. In (b) the PL emission spectra for the series MQW structures of 2 periods (top spectrum), 2 periods (middle spectrum), and 4 periods (bottom spectrum).

7.3 InGaN/*p*-Si(111) heterostructures

The second approach towards applying the InGaN material to photovoltaic devices, is to try to grow InGaN thin films on Si substrates. The reason for this is that Si substrates are much cheaper than the commercial GaN(0001)/*c*-Al_2O_3 or free-standing GaN(0001) wafers that have been used so far in this work, so if we could grow InGaN films on Si with qualities comparable to the ones grown on GaN, there would be great potential for device application.

To look into this hypothesis, a series of three samples was grown by MBE on *p*-type Si(111) substrates, to make a *p-n* heteorstructure. The growth details for each of these samples are summarized in table VII. For two of these samples, a thin AlN layer was deposited prior to the deposition of the InGaN layer, to investigate whether or not such a step improved the crystalline quality of the InGaN film. The samples were subsequently characterized by HR-XRD. Figure 7.5 presents the spectra for the symmetric HR-XRD *ω-2ϑ* scans around the Si(111) Bragg reflection. The intensity of the InGaN off-axis reflection peaks was too low, to make it possible to acquire accurate measurements for the *a*- lattice parameter and, therefore, The composition was calculated by determining the value for the InGaN *c*- lattice parameter from the position of the InGaN peak for the (0002) reflection and assuming full relaxation for the InGaN epilayers.

SAMPLE	AlN layer	T_{gr} (°C)	Ga rate (nm/h GaN eq.)	In rate (nm/h GaN eq.)	N rate (nm/h GaN eq.)	Deposition time (min)
G2509	1nm	485	168	112	280	90
G2510	-	555	168	135	280	72
G2512	1nm	500	168	112	280	75

Table VII: Growth details for the InGaN/*p*-Si(111) heterostructures discussed in this chapter.

Table VIII presents the results from the XRD characterization of these films. It is clear that, indeed, the thin AlN buffer layer improved the film structural quality, as the sample with the largest value of rocking curve FHWM is the one without such a step. It also appears that a lower substrate temperature benefits the crystal quality, as the sample grown at the lowest temperature possesses the lowest RC FWHM, and shows the most symmetric peak in figure 7.5. This agrees with results for InGaN films grown on GaN substrates, where we have seen that lower substrate temperatures yield better crystal quality for samples with higher indium contents. Overall, however, it appears that InGaN films grown on Si(111) substrates are structurally inferior to the ones grown on GaN, and it would still take a lot of effort to improve their quality.

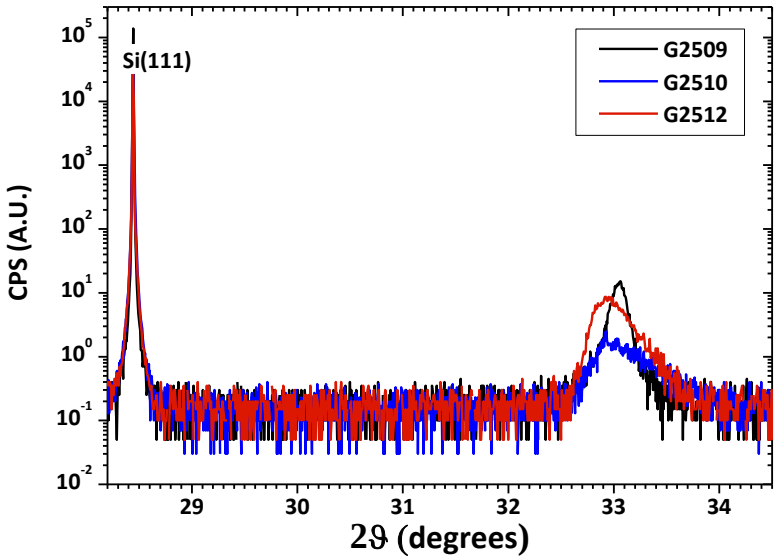

Figure 7.5: Symmetric HR-XRD ω-2ϑ scan around the Si(111) Bragg reflection for the InGaN/*p*-Si(111) heterostructures discussed.

SAMPLE	InN Mole Fraction	Rocking Curve FWHM
G2509	0.45	0.907
G2510	0.48	3.539
G2512	0.46	2.142

Table VIII: XRD characterization results for the InGaN/*p*-Si(111) heterostructures.

7.4 Two basic solar cell devices

Finally, this chapter is concluded with presenting some initial results from two preliminary photovoltaic devices. The first one is based on a polycrystalline InGaN alloy, and the second is a device developed with bulk InGaN film.

The first device discussed in this paragraph involved polycrystalline InGaN thin films. Polycrystalline InGaN films are a good alternative choice for photovoltaic devices when the goal is to develop large area applications. For the device, a polycrystalline InGaN film was grown by the method of Molecular Beam Deposition[9-11] on a *p*-type Si(111) wafer. The sample, here on referred to as G2889, was grown at 450^{o}C with 20 min deposition time. The element arrival rates were 240, 96, and 150 nm/h GaN eq for N, Ga, and In respectively. Prior to device development, the structural properties of the InGaN alloy were characterized by X-ray diffraction, and the optical and luminescent properties of the film were studied by spectroscopic ellipsometry and PL measurements respectively. The symmetric ω-2ϑ scan around the Si(111) Bragg reflection is presented in figure 7.6a, while figure 7.6b shows the results from spectroscopic ellipsometry and photoluminescence measurements. The alloy composition was calculated after extracting the value for the *c* lattice parameter from the symmetric scan and assuming zero value for the strain relaxation, and a 66% InN MF was found for the sample. Using the Scherrer equation, a 42nm value was calculated for the crystallite size. After the sample growth and structural and optical characterization, a thin layer of Au was deposited on the backside of the p-Si to form the bottom ohmic contact. As for the top contact, the conventional photolithographic lift-off technique was used to define the active area of the devices in a grid configuration. Then, 100nm of Au was deposited on the InGaN film as an ohmic contact. In figure 7.7 J-V,curves for different light intensities are presented, for sample G2889. A maximum conversion efficiency of 0.07% was measured for 5 sun illumination, with a maximum filling factor of 29.2% (observed for 1sun illumination).

For the second device discussed in this paragraph, a *p*-GaN(0002)/Al_2O_3 substrate was used. Even though the most popular approach when it comes to PV devices is to grow the active InGaN layer on top of a *n*-GaN substrate, and then cap it with a *p*-GaN layer, for our case, the *n-i-p* structure is used as the preferred architecture. One of the advantages of this approach is that the polarization fields can be exploited to enhance the carrier extraction efficiency of the device [12]. For this device, here on referred to as sample G2989, prior to InGaN growth, a Si_3N_4 pattern was used for the definition of active areas. Subsequently, the InGaN film was grown by MBE. Epitaxy took place at 505^{o}C, with arrival rates for N, Ga, and In 230, 120, and 100 nm/h GaN eq. respectively, and deposition time 40min. These values, according to the kinetic mechanics of MBE previously discussed, correspond to nominal values of 40% InN mole fraction, and 150nm film thickness. A 5nm InN layer was also deposited on top of the InGaN layer. Following the film growth, the Si_3N_4 was lifted off using diluted HF, to expose the *p*-GaN substrate. This method was employed, because it was found that Reactive Ion Etching (RIE), which is typically used for mesa definition after InGaN growth, resulted in surface inversion on the *p*-GaN substrate. For *p*-ohmic contacts a Pd/Ni/Au stacking sequence was used whereas a Ti/Ni/Au stacking sequence was used to form ohmic contacts on InGaN. The J-V,curves for different light intensities are presented, for sample G2889 in figure 7.8. A maximum conversion efficiency of $2.52 \cdot 10^{-4}$% was measured for 2.5 sun illumination.

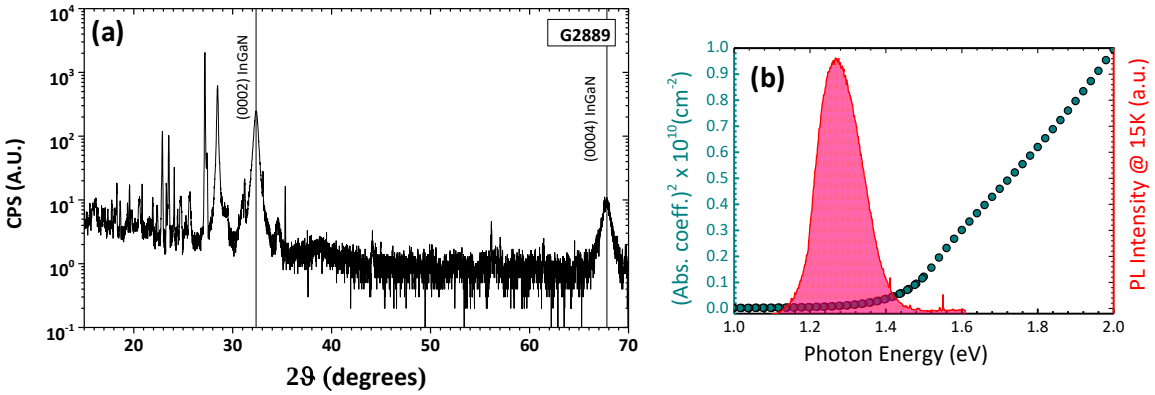

Figure7.6: (a) Symmetric ω-2ϑ scan around the Si(111) reflection for polycrystalline InGaN sample G2889. (b) Absorption coefficient and PL emission spectrum for sample G2889.

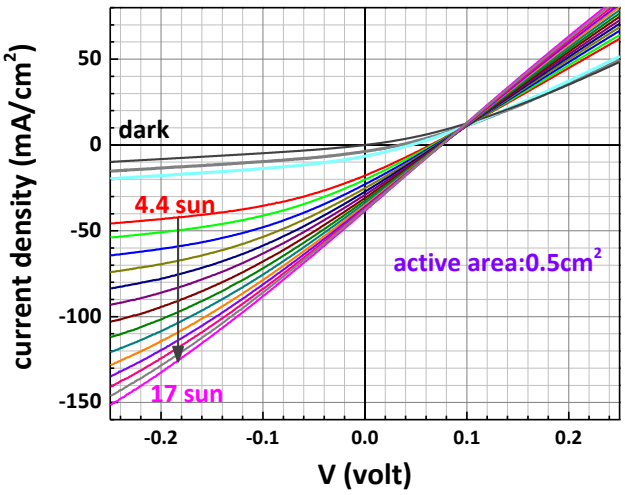

Figure7.7: J-V curves for different light intensities for the photovoltaic device.

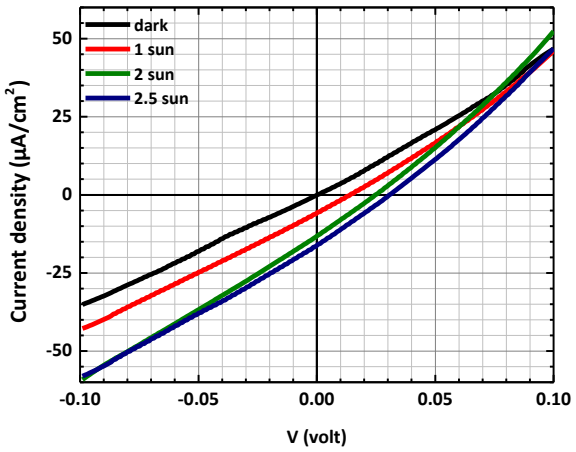

Figure 7.8: J-V curves for different light intensities for sample G2989.

REFERENCES

1. Liou, B.W., *Design and fabrication of InxGa1−xN/GaN solar cells with a multiple-quantum-well structure on SiCN/Si(111) substrates.* Thin Solid Films, 2011. **520**(3): p. 1084-1090.
2. Lai, K.Y., et al., *Effect of indium fluctuation on the photovoltaic characteristics of InGaN/GaN multiple quantum well solar cells.* Applied Physics Letters, 2010. **96**(8): p. 081103.
3. Farrell, R.M., et al., *High quantum efficiency InGaN/GaN multiple quantum well solar cells with spectral response extending out to 520 nm.* Applied Physics Letters, 2011. **98**(20): p. 201107.
4. Dahal, R., et al., *InGaN/GaN multiple quantum well solar cells with long operating wavelengths.* Applied Physics Letters, 2009. **94**(6): p. 063505.
5. Shuji, N., et al., *Superbright Green InGaN Single-Quantum-Well-Structure Light-Emitting Diodes.* Japanese Journal of Applied Physics, 1995. **34**(10B): p. L1332.
6. Shuji, N., et al., *InGaN-Based Multi-Quantum-Well-Structure Laser Diodes.* Japanese Journal of Applied Physics, 1996. **35**(1B): p. L74.
7. Bazioti, C., et al., *Structure and strain variation in InGaN interlayers grown by PAMBE at low substrate temperatures.* physica status solidi (b), 2015. **252**(5): p. 1155-1162.
8. Vickers, M.E., et al., *Determination of the indium content and layer thicknesses in InGaN/GaN quantum wells by x-ray scattering.* Journal of Applied Physics, 2003. **94**(3): p. 1565-1574.
9. Nobuo, M. and K. Kenji, *Amorphous GaAs Films by Molecular Beam Deposition.* Japanese Journal of Applied Physics, 1980. **19**(9): p. 1583.
10. Kazazis, S.A., et al., *Effect of rapid thermal annealing on polycrystalline InGaN thin films deposited on fused silica substrates.* Thin Solid Films, 2016. **611**: p. 46-51.
11. Flory, F.R., *Thin films for optical systems*. 1995, New York: Dekker.
12. Kazazis, S.A., E. Papadomanolaki, and E. Iliopoulos, *Polarization-Engineered InGaN/GaN Solar Cells: Realistic Expectations for Single Heterojunctions* IEEE Journal of Photovoltaics, submitted.

APPENDIX A: PUBLICATIONS

Journal Publications

1. S.A. Kazazis, **E. Papadomanolaki**, and E. Iliopoulos, 'Polarization-Engineered InGaN/GaN Solar Cells: Realistic Expectations for Single Heterojunctions', manuscript submitted to *Journal of Photovoltaics*.

2. S.A. Kazazis, **E. Papadomanolaki**, M. Androulidaki, K. Tsagaraki, A. Kostopoulos, E. Aperathitis and E. Iliopoulos, 'Effect of rapid thermal annealing on polycrystalline InGaN thin films deposited on fused silica substrates', *Thin Solid Films* **611**, 46 (2016).

3 **E. Papadomanolaki**, C. Bazioti, S.A. Kazazis, M. Androulidaki, G.P. Dimitrakopulos and E. Iliopoulos, 'Molecular beam epitaxy of thick InGaN(0001) films: Effects of substrate temperature on structural and electronic properties,' *J. Cryst. Growth* **437**, 20 (2016)

4. C. Bazioti, **E. Papadomanolaki**, Th. Kehagias, T. Walter, J. Smalc-Koziorowska, E. Pavlidou, Ph. Komninou, Th. Karakostas, E. Iliopoulos, G.P. Dimitrakopulos, 'Defects, strain relaxation, and compositional grading in high indium content InGaN epilayers grown by molecular beam epitaxy', *J. Appl. Phys.* **118**, 155301 (2015)

5. C. Bazioti, **E. Papadomanolaki**, Th. Kehagias, M. Androulidaki, G. P. Dimitrakopulos, and E.Iliopoulos, 'Structure and Strain Variation in InGaN Interlayers Grown by PAMBE at Low Substrate Temperatures,' *Phys. Status Solidi* B **252**, 1155 (2015) **Cited: 2(0)**

Conference Proceedings Publications

1. M. Katsikini, F. Pinakidou, E. C. Paloura, J. Arvanitidis, S. Ves, U. Reinholz, E. Papadomanolaki and **E. Iliopoulos**, 'Simulation of the EXAFS and Raman spectra of InxGa1-xN utilizing the equation of motion routine of FEFF8', *J. of Physics: Conference Series* **712**, 012126 (2016)

2. P. Dimitrakis, P. Normand, C. Bonafos, **E. Papadomanolaki** and E. Iliopoulos, 'GaN Quantum Dots as Charge Storage Elements for Memory Devices,' *MRS Proceedings*, **1430** (2012).

APPENDIX B: CONFERENCE PRESENTATIONS

1. **E. Papadomanolaki**, S.A. Kazazis, C. Bazioti, F. Kalaitzakis, G.P. Dimitrakopulos and E. Iliopoulos, 'InGaN Heteroexpitaxy on GaN(0001) for Photovoltaic Applications', EXMATEC-2016, June 2016, Aveiro, Portugal.

2. S.A. Kazazis, **E. Papadomanolaki**, M. Androulidaki, and E. Iliopoulos, 'Dielectric Functions and Bowing Parameter of InGaN Alloys in the Entire Composition Range' 6th International Conference on Micro-Nanoelectronics, Nanotechnologies & MEMs (Micro & Nano 2015), October 2015, Athens, Greece.

3. S.A. Kazazis, **E. Papadomanolaki**, M. Androulidaki, and E. Iliopoulos, 'Rapid Thermal Annealing Effects on Polycrystalline InGaN Deposited on Fused Silica Substrates', 6th International Conference on Micro-Nanoelectronics, Nanotechnologies & MEMs (Micro & Nano 2015), Athens, October 2015, Greece.

4. M. Katsikini, F. Pinakidou, E. C. Paloura, J. Arvanitidis, S Ves, U. Reinholz, **E. Papadomanolaki**, E. Iliopoulos, 'Simulation of the EXAFS and Raman spectra of $In_xGa_{1-x}N$ utilizing the equation of motion routine of FEFF8', XXXI PCSSPMS, September 2015, Thessaloniki, Greece.

5. C. Bazioti, **E. Papadomanolaki**, Th. Kehagias, T. Walther, J. Smalc-Koziorowska, E. Pavlidou, Ph. Komninou, Th. Karakostas, E. Iliopoulos, and G. P. Dimitrakopulos, 'Microstructural evolution in high alloy content InGaN films grown by molecular beam epitaxy', XXXI PCSSPMS, September 2015, Thessaloniki, Greece.

6. **E. Papadomanolaki**, S. Kazazis, A. Georgakilas, and E. Iliopoulos, 'Growth Kinetics of InGaN Films by Plasma-Assisted Molecular Beam Epitaxy on (0001) GaN', 11th International Conference on Nitride Semiconductors (ICNS-11), August 2015, Beijing, China.

7. **E. Papadomanolaki**, C. Bazioti, S.A. Kazazis, M. Androulidaki, K. Tsagaraki, A. Georgakilas, G. P. Dimitrakopulos, and E. Iliopoulos, 'Phase Separation, Structural Quality, and Optoelectronic Properties of InGaN films in the Entire Compositional Range Grown by RF-MBE', 11th International Conference on Nitride Semiconductors (ICNS-11), August 2015, Beijing, China.

8. S.A. Kazazis, **E. Papadomanolaki**, M. Androulidaki, K. Tsagaraki, A. Kostopoulos, E. Aperathitis, and E. Iliopoulos, 'Rapid Thermal Annealing Effects on Polycrystalline InGaN Deposited on Fused Silica Substrates', 11th International Conference on Nitride Semiconductors (ICNS-11), August 2015, Beijing, China.

9. S.A. Kazazis, **E. Papadomanolak**i, M. Androulidaki, and E. Iliopoulos, 'Dielectric Functions and Bowing Parameter of InGaN Alloys in the Entire Composition Range', 11th International Conference on Nitride Semiconductors (ICNS-11), August 2015, Beijing, China.

10. G.P. Dimitrakopulos , C. Bazioti, **E. Papadomanolaki**, Th. Kehagias, T. Walther, J. Smalc-Koziorowska, E. Pavlidou, Ph. Komninou, Th. Karakostas, and E. Iliopoulos, ''Modes of Defect Introduction and Indium Distribution in InGaN Epilayers Grown by Molecular Beam Epitaxy', 11th International Conference in Nitride Semiconductors (ICNS-11), August 2015, Beijing, China.

11. M. Katsikini, F. Pinakidou, E. C. Paloura, J. Arvanitidis, S Ves, U. Reinholz, **E. Papadomanolaki**, and E. Iliopoulos, 'Simulation of the EXAFS and Raman spectra of $In_xGa_{1-x}N$ utilizing the equation of motion routine of FEFF8', 16th International Conference in X-ray absorption fine structure, August 2015, Karlsruhe, Germany.

12. C. Bazioti, **E. Papadomanolaki**, Th. Kehagias, M. Androulidaki, G.P. Dimitrakopulos, and E. Iliopoulos, 'Structural and optical properties of low-temperature InGaN thin layers and multi-quantum well grown by PAMBE', EMRS Spring Meeting, May 2015, Lille, France.

13. C. Bazioti, **E. Papadomanolaki**, Th. Kehagias, T. Walther, J. Smalc-Koziorowska, Ph. Komninou, E. Iliopoulos, and G.P. Dimitrakopulos, 'Strain accommodation and indium incorporation in InxGa1-xN epilayers grown by molecular beam epitaxy'', XIX Microscopy of Semiconducting Materials, March 2015, Cambridge, Great Britain.

14. C. Bazioti, Th. Kehagias, T. Walther, **E. Papadomanolaki**, E. Iliopoulos, G.P. Dimitrakopulos, 'Strain relaxation of high In-content InGaN epilayers grown by PAMBE', IMC-2014, September 2014, Prague, Czech Republic.

15. C. Bazioti, T. Kehagias, **E. Papadomanolaki**, E. Iliopoulos., G.P. Dimitrakopulos, 'Indium Incorporation, Interfacial Properties, and Strain Relaxation at InGaN Interlayers Grown by PAMBE,' IMC-2014, September 2014, Prague, Czech Republic.

16. **E. Papadomanolaki**, C. Bazioti, Th. Kehagias, A. Georgakilas, G. P. Dimitrakopulos, and E. Iliopoulos, 'RF-MBE of InGaN Epilayers on GaN(0001): Substrate Temperature Effects on Indium Incorporation Kinetics and Films' Defect Structure,' International Workshop on Nitride Semiconductors (IWN-2014), August 2014, Wroclaw, Poland.

17. P. Dimitrakis, P. Normand, C. Bonafos, **E. Papadomanolaki**, and E.Iliopoulos, 'GaN Quantum Dots for Nano-floating Gate Memory Capacitors,' International Workshop on Nitride Semiconductors (IWN-2014), August 2014, Wroclaw, Poland.

18. C. Bazioti, Th. Kehagias, **E. Papadomanolaki**, E. Iliopoulos, and G. P. Dimitrakopulos, 'Structure and Strain Variation of InGaN Interlayers Deposited by PAMBE; International Workshop on Nitride Semiconductors (IWN-2014), August 2014, Wroclaw, Poland.

19. C. Bazioti, Th. Kehagias, Th. Walther, **E. Papadomanolaki**, E. Iliopoulos, and G. P. Dimitrakopulos, 'Evolution of Strain Relaxation with Alloy Content in InGaN Thin Films Grown by PAMBE,' International Workshop on Nitride Semiconductors (IWN-2014), August 2014, Wroclaw, Poland.

20. S. A. Kazazis, **E. Papadomanolaki**, M. Androulidaki, K. Tsagaraki, A. Kostopoulos, E. Aperathitis, and E. Iliopoulos, 'Effect of Rapid Thermal Annealing on Polycrystalline InGaN Deposited on Fused Silica Substrates,' International Workshop on Nitride Semiconductors (IWN-2014), August 2014, Wroclaw, Poland.

21. C. Bazioti, G.P. Dimitrakopulos, Th. Kehagias, Th. Walther, **E. Papadomanolaki**, and E. Iliopoulos, 'Quantitative Transmission Electron Microscopy of High Alloy Content InGaN Deposited by PAMBE: from Epilayers to Quantum Wells,' E-MRS 2014 Fall Meeting, September 2014, Warsaw, Poland.

22. C. Bazioti, Th. Kehagias, E. Papadomanolaki, E. Iliopoulos, G.P. Dimitrakopulos, "Structural Behavior of High Indium Content InGaN Quantum Wells grown by PAMBE", EDS-2014, Göttingen, Germany, September 2014.

23. C. Bazioti, Th. Kehagias, T. Walther, **E. Papadomanolaki**, E. Iliopoulos, and G.P. Dimitrakopulos, 'Strain-Induced Defect Microstructure of High Alloy Content InGaN Epilayers grown by Plasma-Assisted Molecular Beam Epitaxy,' EDS, September 2014, Göttingen, Germany.

24. **E. Papadomanolaki**, C. Bazioti, S. Kazazis, Th. Kehagias, A. Georgakilas, G.P. Dimitrakopulos, E. Iliopoulos 'High In Content InGaN Films Grown by Plasma-Assisted Molecular Beam Epitaxy for Photovoltaic Applications,' XXX PCSSPMS, September 2014, Heraklion, Crete.

25. S.A. Kazazis, **E. Papadomanolaki**, M. Androulidaki, K. Tsagaraki, A. Kostopoulos, E.Aperathitis, and E. Iliopoulos, 'Effect of rapid thermal annealing on polycrystalline InGaN deposited on fused silica substrates,' XXX PCSSPMS, September 2014, Heraklion, Crete.

26. Th. Kehagias, C. Bazioti, G.P. Dimitrakopulos, Th. Walther, **E. Papadomanolaki**, and E. Iliopoulos, 'Strain Accommodation in InGaN Epilayers and Interlayers with High Alloy Content Towards Efficient Photovoltaics,' XXX PCSSPMS, September 2014, Heraklion, Crete.

27. C. Bazioti, Th. Kehagias, T. Walther, **E. Papadomanolaki**, E. Iliopoulos, and G.P. Dimitrakopulos, 'Mesoscale Phase Separation and Strain Relaxation Phenomena in High Indium Content InGaN Epilayers Grown by Molecular Beam Epitaxy,' EXMATEC, June 2014, Delphi, Greece.

28. **E. Papadomanolaki**, C. Bazioti, K. Tsagaraki, Th. Kehagias, A. Georgakilas, G.P. Dimitrakopulos, and E. Iliopoulos, 'Kinetics of Indium Incorporation in RF-MBE of InGaNFilms on GaN(0001) Substrates for Photovoltaic Applications,' WOCSCICE, June 2014, Delphi, Greece.

29. S.A. Kazazis, **E. Papadomanolaki**, M. Androulidaki, K. Tsagaraki, A. Kostopoulos, E. Aperathitis, and E. Iliopoulos, 'Rapid Thermal Annealing Effects on Polycrystalline InGaN Thin Films Deposited on Fused Silica Substrates, WOCSCICE, June 2014, Delphi, Greece.

30. **E. Papadomanolaki**, M. Androulidaki, K. Tsagaraki, C. Bazioti,Th. Kehagias, G. Dimitrakopulos, E. Iliopoulos, 'Molecular Beam Epitaxy of Single Phase InGaN Films for Photovoltaic Applications in the Entire Alloy Composition Range,' XXIX PCSSPMS, September 2013, Athens, Greece.